ANTENNA COUPLED METAMATERIAL INSPIRED PASSIVE SENSORS FOR GLAUCOMA MONITORING

by

Ümmühan Aybüke Çalıkoğlu

B.S., Electrical and Electronics Engineering, Boğaziçi University, 2016

Submitted to the Institute for Graduate Studies in
Science and Engineering in partial fulfillment of
the requirements for the degree of
Master of Science

Graduate Program in Electrical and Electronics Engineering
Boğaziçi University
2019

ACKNOWLEDGEMENTS

I express my gratitude to Prof. Arda Deniz Yalçınkaya and Assoc. Prof. Hamdi Torun, my supervisors, and Prof. Günhan Dündar for their support in this study. Their guidance, trust and support were an important motivation for me. Their professional approach to the encountered problems showed me how to look for a solution from different perspectives. They were very helpful during all this study and I was the luckiest graduate student.

I would like to thank Prof. Günhan Dündar and Assist. Prof. Onur Ferhanoğlu for their participation in my thesis jury.

I would also like to thank Glakolens for giving me the opportunity to do science while working. Every day in Glakolens is full of learning and shining! I would like to thank all my colleagues, it is a pleasure to work with them. I would also like to thank all friends in MNCL and BETA family for their both academically and friendly supports. I owe my special thanks to Onur Ateş, Özgür Kaya, Berk Çamlı, Deniz Özen and Kerim Yıldırım for their help and support in this work. Without them, the content of this study would never be as rich as it is.

I would like to thank my dearest friends Selin, DGD, Eylül, Damla, Mehmet, Alper, Barış, Saba, Yavuz, Kürşad, Kor and many others which I believe the most precious people in the world. I'm thankful to all for sharing such a wonderful bonding with me.

Finally, I would especially like to thank my amazing family for their endless support, love, and encouragement I have gotten over the years. In particular, I would like to thank my parents Gülsüm and Nail Çalıkoğlu, and my sister Nilay Çalıkoğlu, who have always believed in me.

ABSTRACT

ANTENNA COUPLED METAMATERIAL INSPIRED PASSIVE SENSORS FOR GLAUCOMA MONITORING

Glaucoma is an eye disease that may cause blindness by damaging the optic nerve due to elevation of the intraocular pressure. In this thesis, a passive metamaterial inspired resonator sensor for non-invasive and continuous monitoring of glaucoma is developed to improve diagnosis accuracy and treatment of glaucoma. The geometry of the resonator is optimized such that it can be embedded in a conventional contact lens. The sensor is fabricated and embedded in a contact lens to be used for continuous glaucoma monitoring. Finite-element based models are developed to analyse the operation of the devices and to optimize the sensor structure. For this purpose, the contact lens placed on the eye model is examined by the finite element method and the displacement of the contact lens due to the increase in intraocular pressure is analyzed. Mechanical simulations are also given to examine the fabrication of the sensors. The proposed sensor is excited and interrogated using a tunable antenna. The resonant frequency of the resonator is measured by measuring the reflection characteristics with designed antenna which is tuned to be coupled to the resonator sensor. Theoretical and simulation based analysis for tunable antennas are also shown. In-vitro characterization of the antenna coupled contact lens sensor with respect to varying intraocular pressure levels of mechanical eye model are done experimentally. According to the results obtained, the sensitivity of the device, i.e. the change in resonant frequency for a unit change in pressure, is calculated as $-31.09\,\mathrm{kHz/mmHg}$ with the resolution of $1.98\,\mathrm{mmHg}$. The experimental results supported by finite-element based models indicate that the demonstrated device is suitable for glaucoma diagnosis and monitoring.

ÖZET

GLOKOM İZLEME İÇİN METAMALZEMEDEN ESİNLENİLMİŞ ANTEN EŞLENİK PASİF ALGIÇLAR

Glokom, göz içi basıncının yükselmesi nedeniyle optik sinire zarar vererek körlüğe neden olabilecek bir göz hastalığıdır. Bu tezde, glokomun invazif olmayan bir yöntemle sürekli izlenmesi için metamalzemeden esinlenilmiş pasif bir rezonatör algıç, glokomun teşhis doğruluğunu ve tedavisini iyileştirmek için geliştirilmiştir. Rezonatörün geometrisi, konvansiyonel bir kontakt lens içine gömülebilecek şekilde optimize edilmiştir. Algıç, sürekli glokom izlemesi için kullanılmak üzere üretilmiş ve bir kontakt lens içine gömülmüştür. Sonlu elemanlar tabanlı modeller, cihazların çalışmasını analiz etmek ve algıç yapısını optimize etmek için geliştirilmiştir. Bu amaçla, göz modeline yerleştirilmiş olan kontakt lens sonlu elemanlar yöntemi ile incelenerek, göz içi basıncındaki artıştan dolayı kontakt lensin yer değiştirmesi analiz edilmiştir. Algıçların üretimini incelemek için mekanik simülasyonlar da bu tezde verilmiştir. Önerilen algıç, akort edilebilir bir anten kullanılarak uyarılır ve sorgulanır. Rezonatörün rezonans frekansı, algıça eşlenik bir anten yardımıyla yansıtma parametrelerinin ölçülmesiyle bulunur. Akort edilebilir antenler için teorik ve simülasyon temelli analizler de bu tezde verilmiştir. Antene eşlenik kontakt lens algıçın in vitro karakterizasyonu mekanik göz modelinin değişen göz içi basınç seviyelerine göre deneysel olarak yapılmıştır. Elde edilen sonuçlara göre, cihazın hassasiyeti, yani basınçtaki bir birim değişikliği için rezonans frekansındaki değişim, 1.98 mmHg çözünürlüğü ile $-31.09\,\mathrm{kHz/mmHg}$ olarak hesaplanmıştır. Sonlu elemanlar temelli modellerle desteklenen deney sonuçları, gösterilen cihazın glokom teşhisi ve izlemesi için uygun olduğunu göstermektedir.

TABLE OF CONTENTS

ACKNOWLEDGEMENTS . . . iii
ABSTRACT . . . iv
ÖZET . . . v
LIST OF FIGURES . . . viii
LIST OF TABLES . . . xvi
LIST OF SYMBOLS . . . xix
LIST OF ACRONYMS/ABBREVIATIONS . . . xxi
1. INTRODUCTION . . . 1
1.1. Flexible Strain Sensors . . . 1
1.2. SRR Based Sensors . . . 2
1.3. Application Area: Glaucoma Monitoring . . . 3
1.3.1. Glaucoma . . . 3
1.3.2. Glaucoma Monitoring Methods . . . 4
1.3.3. SRR Based Sensors . . . 8
1.4. Thesis Contribution and Organization . . . 10
2. DESIGN AND SIMULATIONS OF SRR BASED SENSOR . . . 11
2.1. Microwave Modeling of the Resonator . . . 11
2.1.1. SRR Simulations . . . 14
2.1.1.1. SRR Metal Thickness Analysis . . . 14
2.1.1.2. SRR Metal Permeability Analysis . . . 19
2.1.1.3. SRR Saline Water Effect Analysis . . . 20
2.2. Mechanical Eye Model Simulations . . . 22
2.2.1. Contact Lens placed on Eye Model . . . 22
2.2.2. Contact Lens Embedded Sensor . . . 25
2.2.2.1. SRR Embedded in PDMS: Stress Simulations . . . 25
2.2.2.2. SRR Embedded in Polyimide: Stress Simulations . . . 27
2.3. Fabrication of SRR Embedded in PDMS . . . 28
3. DESIGN OF TUNABLE ANTENNAS . . . 34
3.1. Theoretical Modeling . . . 34

3.2. Simulations 35
3.3. Characterization of Antennas 37
4. DESIGN AND MODELING OF BC-SRR BASED ANTENNA COUPLED SENSOR 39
4.1. Theoretical Modeling 39
4.2. Simulations 41
4.2.1. BC-SRR Embedded in Polyimide Thickness Analysis Simulations 44
4.2.2. BC-SRR Embedded in Polyimide Loss Tangent Simulations . . 45
4.2.3. BC-SRR based sensor placed on Eye-globe Material Simulations 47
5. FABRICATION AND CHARACTERIZATION OF SENSORS 51
5.1. Fabrication of Sensors Embedded in Polyimide 51
5.2. PDMS Eye Model 53
5.3. Embedding in Contact Lens Material 55
5.4. Measurement Setup 57
5.5. Results 58
6. CONCLUSION AND FUTURE WORK 60
6.1. Future Work 62
REFERENCES 63
APPENDIX A: RESULTS OF THE SIMULATED ANTENNAS 72
APPENDIX B: IN VITRO TEST RESULTS 78

LIST OF FIGURES

Figure 1.1. Illustration of IOP measurement with GAT [40]. 4

Figure 1.2. Microfabricated flexible-coiled wireless pressure sensor with its (left) top and (right) bottom views [41]. 5

Figure 1.3. (a) Experimental setup for in vivo pressure sensing test (rabbit),(b) measured phase-dip curves [41]. 6

Figure 1.4. Photograph of the sensing CL [42]. 6

Figure 1.5. A photograph of the CLS [43]. 7

Figure 1.6. An illustration of the experimental setup for the SRR sensor realized on flexible latex rubber [44]. 8

Figure 1.7. An illustration of the experimental setup for measuring the effect of curvature change [2]. 9

Figure 2.1. Split-ring resonator drawing [14]. 12

Figure 2.2. Dielectric properties of PI [46]. 14

Figure 2.3. Calculated RF sheet resistance values for (a) various sheet thickness of gold vs frequency, (b) and (c) various frequencies vs gold thickness. 17

Figure 2.4. (a) Simulation model and (b) s_{21} spectra of simulated model for various thicknesses of gold. 18

Figure 2.5. Simulated (a) s_{11} and (b) s_{21} spectra for varying values of permeability of metal layer. 19

Figure 2.6. Illustration of the monopole antenna pair coupled SRR on FR-4 with water layer. 20

Figure 2.7. Simulated s_{21} spectra for varying values of conductivity ($\mathrm{S\,m^{-1}}$) of defined water layer. 21

Figure 2.8. (a) Computational model including an eyeball and a CL, (b) maximum displacement values for CLs with thicknesses of 100 µm and 200 µm with respect to changes in IOP levels. 23

Figure 2.9. The deflection profile for the simulation when the change in IOP level is 5 mmHg. Red arrows illustrate (a) the normalised displacements when apical displacement is set to 0, (b) tangential displacements on CL model. 24

Figure 2.10. Stress-strain curve for (a) native PDMS [50] and (b) for gold [51]. 25

Figure 2.11. Stress distribution on (a) PDMS when PDMS is not bent, (b) PDMS when PDMS is bent and (c) 100 nm gold ring. 26

Figure 2.12. Stress distribution on (a) PI when PI is bent, (b) 5 µm thick gold ring. 27

Figure 2.13. SRR embedded in PDMS fabrication process flow. 28

Figure 2.14. PDMS spin coating recipe [55]. 29

Figure 2.15. Dark field mask strapped on a glass substrate. 30

Figure 2.16. (a) The laser cut SRR embedded in PDMS structures stored in DI water. (b) Optical microscopy images show the cracked surface that was left from sputtering. 31

Figure 3.1. Illustrations of simulated antennas. 36

Figure 3.2. Photograph of an example antenna with C_{tuning} and SMA connector. 37

Figure 3.3. Measured s_{11} spectra of the folded dipole antenna with respect to varying values of the C_{tuning}. 38

Figure 4.1. Illustration of the simulated folded dipole antenna coupled BC-SRR embedded in PDMS. 41

Figure 4.2. The simulated s_{11} spectra with respect to varying additional distances (mm) of the BC-SRR to the antenna. 42

Figure 4.3. (a) Simulated E field lines on xz plane and (b) simulated E field in z direction in between the rings of the BC-SRR of the folded dipole antenna coupled BC-SRR at resonance. 43

Figure 4.4. (a) Simulated H field lines on xz plane and (b) simulated H field in z direction on xz plane of the folded dipole antenna coupled BC-SRR at resonance. 43

Figure 4.5. (a) Illustration of the simulated folded dipole antenna and BC-SRR embedded in the PI substrate. (b) Simulated s_{11} spectra with respect to varying values of thicknesses of the metal layers of BC-SRR. 44

Figure 4.6. The simulations were performed for the antenna coupled BC-SRR embedded in the PI substrate with respect to varying values of tangent loss of the substrate. 46

Figure 4.7. (a) Illustration of the simulated sensor bent on eye-globe material, (b) Detailed illustration of the planar sensor showing defined a and (c) Simulated s_{21} spectra for varying a (mm). 47

Figure 4.8. Simulated s_{21} spectra with respect to varying values of r of the eye-globe where (a) r is changing from 8.1 mm to 8.2 mm and (b) r is changing from 8.5 mm to 8.58 mm. 49

Figure 4.9. (a) Illustration of the simulated folded dipole antenna with the BC-SRR based CLS placed on the eye-globe material. (b) Simulated s_{11} behavior of the system with respect to varying values of C_{tuning} (pF). 50

Figure 5.1. (a) Photograph of the PI spin coated wafer. (b) Soft baking on hot plate. 51

Figure 5.2. (a) Soft baking of the last spin coated PI layer. (b) Photograph of the hard-baked wafer. 52

Figure 5.3. Photograph of the laser machined sensor. 53

Figure 5.4. (a) Illustration of the modeled eye. (b) Designed molds for the fabrication of the mechanical eye model. 54

Figure 5.5. Photograph of the 3D printed VeroClear molds glass transited for the fabrication of the mechanical eye. 54

Figure 5.6. Photograph of the fabricated mechanical eyes from PDMS. 55

Figure 5.7. (a) Photograph of the closed mold pair. (b) Photograph of the spherically deformed sensor bent by molding. 56

Figure 5.8. Photograph of the spherically deformed sensor embedded in CL. . 56

Figure 5.9. Photograph of the PDMS eye model integrated test setup. (b) Photograph of the pressure sensor. 57

Figure 5.10. Photograph of the antenna and the CLS placed on the PDMS eye. 58

Figure 5.11. The ensemble of the experiments showing the mean values of the measured resonant frequencies with standard deviation error bars. 59

Figure A.1. s_{11} spectra of the simulated antennas without tuning capacitance (C_{tuning}) around their first modes. 72

Figure A.2. s_{11} spectra of the folded dipole antennas ($N = 1$) with respect to varying tuning capacitance (C_{tuning}) values around their first modes. 73

Figure A.3. s_{11} spectra of the spiral-dipole antennas with 2 turns ($N = 2$) with respect to varying tuning capacitance (C_{tuning}) values around their first modes. 74

Figure A.4. s_{11} spectra of the spiral-dipole antennas with 3 turns ($N = 3$) with respect to varying tuning capacitance (C_{tuning}) values around their first modes. 75

Figure A.5. s_{11} spectra of the spiral-dipole antennas with 4 turns ($N = 4$) with respect to varying tuning capacitance (C_{tuning}) values around their first modes. 76

Figure A.6. s_{11} spectra of the spiral-dipole antennas with 5 turns ($N = 5$) with respect to varying tuning capacitance (C_{tuning}) values around their first modes. 77

Figure B.1. Measured s_{11} spectra for trial 1 showing the resonant frequencies with respect to varying values of IOP levels. 78

Figure B.2. Measured s_{11} spectra for trial 2 showing the resonant frequencies with respect to varying values of IOP levels. 79

Figure B.3. Measured s_{11} spectra for trial 3 showing the resonant frequencies with respect to varying values of IOP levels. 80

Figure B.4. Measured s_{11} spectra for trial 4 showing the resonant frequencies with respect to varying values of IOP levels. 81

Figure B.5. Measured s_{11} spectra for trial 5 showing the resonant frequencies with respect to varying values of IOP levels. 82

Figure B.6. Measured s_{11} spectra for trial 6 showing the resonant frequencies with respect to varying values of IOP levels. 83

Figure B.7. Measured s_{11} spectra for trial 7 showing the resonant frequencies with respect to varying values of IOP levels. 84

Figure B.8. Measured s_{11} spectra for trial 8 showing the resonant frequencies with respect to varying values of IOP levels. 85

Figure B.9. Measured s_{11} spectra for trial 9 showing the resonant frequencies with respect to varying values of IOP levels. 86

Figure B.10. Measured s_{11} spectra for trial 10 showing the resonant frequencies with respect to varying values of IOP levels. 87

Figure B.11. Measured s_{11} spectra for trial 11 showing the resonant frequencies with respect to varying values of IOP levels. 88

Figure B.12. Measured s_{11} spectra for trial 12 showing the resonant frequencies with respect to varying values of IOP levels. 89

Figure B.13. Measured s_{11} spectra for trial 13 showing the resonant frequencies with respect to varying values of IOP levels. 90

Figure B.14. Measured s_{11} spectra for trial 14 showing the resonant frequencies with respect to varying values of IOP levels. 91

Figure B.15. Measured s_{11} spectra for trial 15 showing the resonant frequencies with respect to varying values of IOP levels. 92

Figure B.16. Measured s_{11} spectra for trial 16 showing the resonant frequencies with respect to varying values of IOP levels. 93

Figure B.17. Measured s_{11} spectra for trial 17 showing the resonant frequencies with respect to varying values of IOP levels. 94

Figure B.18. Measured s_{11} spectra for trial 18 showing the resonant frequencies with respect to varying values of IOP levels. 95

Figure B.19. Measured s_{11} spectra for trial 19 showing the resonant frequencies with respect to varying values of IOP levels. 96

LIST OF TABLES

Table 2.1. SRR calculations. 13

Table 2.2. Experimental results of PDMS spin coating in the clean room. . . 30

Table 3.1. Design parameters of simulated antennas. 36

Table 3.2. Comparison of the measured first modes of the folded dipole antennas with the calculated and simulated values. 38

Table 6.1. The final design parameters of the antenna coupled CLS system and the achieved performance metrics. 61

Table A.1. Comparison of calculated and simulated first modes of antennas without tuning capacitance (C_{tuning}). 72

Table A.2. Comparison of calculated and simulated first modes of folded dipole antennas ($N = 1$) with respect to varying tuning capacitance (C_{tuning}) values. 73

Table A.3. Comparison of calculated and simulated first modes of spiral-dipole antennas with 2 turns ($N = 2$) with respect to varying tuning capacitance (C_{tuning}) values. 74

Table A.4. Comparison of calculated and simulated first modes of spiral-dipole antennas with 3 turns ($N = 3$) with respect to varying tuning capacitance (C_{tuning}) values. 75

Table A.5. Comparison of calculated and simulated first modes of spiral-dipole antennas with 4 turns ($N = 4$) with respect to varying tuning capacitance (C_{tuning}) values. 76

Table A.6. Comparison of calculated and simulated first modes of spiral-dipole antennas with 5 turns ($N = 5$) with respect to varying tuning capacitance (C_{tuning}) values. 77

Table B.1. Tabulated data obtained from trial 1. 78

Table B.2. Tabulated data obtained from trial 2. 79

Table B.3. Tabulated data obtained from trial 3. 80

Table B.4. Tabulated data obtained from trial 4. 81

Table B.5. Tabulated data obtained from trial 5. 82

Table B.6. Tabulated data obtained from trial 6. 83

Table B.7. Tabulated data obtained from trial 7. 84

Table B.8. Tabulated data obtained from trial 8. 85

Table B.9. Tabulated data obtained from trial 9. 86

Table B.10. Tabulated data obtained from trial 10. 87

Table B.11. Tabulated data obtained from trial 11. 88

Table B.12. Tabulated data obtained from trial 12. 89

Table B.13. Tabulated data obtained from trial 13. 90

Table B.14. Tabulated data obtained from trial 14. 91

Table B.15. Tabulated data obtained from trial 15. 92

Table B.16. Tabulated data obtained from trial 16. 93

Table B.17. Tabulated data obtained from trial 17. 94

Table B.18. Tabulated data obtained from trial 18. 95

Table B.19. Tabulated data obtained from trial 19. 96

LIST OF SYMBOLS

A	Area of half-ring
a	Half-width of the overlapping parts of BC-SRR
Au	Gold
B	Magnetic induction
C	Capacitance
C_{dis}	Distributed capacitance of spiral dipole antenna
C_{gap}	Gap capacitance
C_{port}	Input port capacitance of folded dipole antenna
C_{surf}	Surface capacitance
C_{total}	Total capacitance of antenna
C_{tuning}	Tuning capacitance of antenna
CO_2	Carbon dioxide
Cr	Chromium
d	Distance between rings
E	Electric field intensity
f_0	Resonant frequency
$f_{0(a)}$	The first mode frequency of antenna
g	Gap distance of SRR
g_p	Gap distance of input port
G_s	RF sheet conductance
H	Magnetic field intensity
h	Thickness of SRR
H_2O_2	Hydrogen peroxide
h_a	Thickness of metal of antenna
$h_{substrate}$	Thickness of substrate
HF	Hydrogen fluoride
N	Number of turns
n	Refractive index

N_2	Nitrogen
L	Inductance
l_a	Length of coil
O_2	Oxygen
R	Inner radius of SRR
r	Radius of simulated eye-globe
R_a	Average radius of two adjacent coils
R_{avg}	Average radius of coils
R_m	Average radius of SRR
R_s	RF sheet resistance
s_{11}	Reflection
s_{21}	Transmission
s_a	Gap between two adjacent coils
t	Thickness of metal
Ti	Titanium
w	Width of SRR
w_a	Width of coil
δ_s	Skin Depth
ε_0	Permittivity of free space
ε_{eff}	Effective permittivity
ε_r	Relative permittivity
$\varepsilon_{r(eff)}$	Effective relative permittivity of antenna
λ	Wavelength
μ	Magnetic permeability
μ_0	Magnetic permeability of free space
μ_r	Relative magnetic permeability
ρ	Bulk resistivity
σ_s	RF conductivity
$\tan\delta$	Loss tangent

LIST OF ACRONYMS/ABBREVIATIONS

BC-SRR	Broadside-coupled split ring resonator
CL	Contact lens
CLS	Contact lens sensor
CMOS	Complementary metal oxide semiconductor
DI	Deionized
e-skin	Electronic skin
FEM	Finite element method
FDTD	Finite difference time domain
FR-4	Flame retardant 4
GAT	Goldmann applanation tonometer
GUI	Graphical user interface
IOP	Intraocular pressure
IR	Infrared
LC	Inductor-capacitor
MEMS	Micro electro mechanical systems
PDMS	Polydimethylsiloxane
PI	Polyimide
PR	Photoresist
PUA	Polyurethane acrylate
Q	Quality factor
RF	Radio frequency
RLC	Resistor-inductor-capacitor
ROC	Radius of curvature
SRR	Split ring resonator
UV	Ultraviolet
VNA	Vector network analyzer

1. INTRODUCTION

The main objective of this thesis is to develop a passive sensor for non-invasive and continuous monitoring of glaucoma by measuring Intraocular Pressure (IOP), which is reported to be strongly correlated with the corneal radius of curvature (ROC). [1,2] For this thesis, a resonator is designed so that its resonant frequency will vary with changing ROC. The resonant frequency is measured from the reflection or the transmission characteristics with an antenna which is tuned to be coupled to the resonator. The sensor is fabricated and embedded in a contact lens (CL) to be used for continuous glaucoma monitoring.

1.1. Flexible Strain Sensors

In healthcare monitoring applications, strain sensors attract a great deal of attention and are used in many ways. In particular, sensors with high flexibility and sensitivity are used in the form of strain sensors. Strain sensors respond to mechanical deformations used for precise detection of human health and activity with changes in electrical behavior [3].

Traditionally, complementary metal oxide semiconductor (CMOS) based sensors have been used in health monitoring with due to high precision; however, their rigid and brittle natures create disadvantageous applications in portable and implantable devices. Recently, micro-electromechanical systems (MEMS) fabricated, soft, precise and low-cost flexible sensors have been shown to have numerous advantages for next-generation wearable devices [4].

Well-developed MEMS manufacturing processes, improvements in the materials used in production [5], and stretchable sensor structures [6] benefit the further development of flexible strain sensors. Currently, studies are being carried out for the use of flexible strain sensors in the applications of electronic skin (e-skin) [7, 8], human-machine interfaces, human-motion detection [3, 9], biomedical implants [6, 10, 11], and

gloves [12].

In recent years, metamaterials have been used as flexible strain sensors. A strain sensor based on a split ring resonator (SRR) on a flexible substrate operating in the L-band of microwave region was demonstrated by Melik *et al.* in 2009 [13]. The operating principle of the sensor relies on the shift in the resonant frequency with an externally applied load to monitor the strain wirelessly. The operating mechanism of the sensor is based on the fact that the resonance behavior of the metamaterials is highly dependent on the geometry of the unit cell [14]. Therefore, based on this correlation between the deformation and the shift in the resonant frequency, metamaterial structures can be utilized to measure the strain on an object.

1.2. SRR Based Sensors

SRRs have very simple geometry which is basically a metal ring with a split. Depending on their geometry, they can have strong resonance characteristics with very high quality factors (Q). The conventional SRR is widely utilized in microwave and radio frequency (RF) applications for different purposes. Their applications can be extended to infrared (IR) or visible light regions [15].

SRR can provide a negative magnetic permeability, which derives from a 180° phase delay between magnetic field (H) and magnetic induction (B). Therefore, SRRs can be used to obtain negative refractive index (n) [16, 17]. With these favorable electromagnetic characteristics, they are used in optics [18] and electronics [19, 20].

Moreover, SRRs can be used in biosensing applications in a simple and cost-effective manner. One of the sensing mechanism of microwave biochemical sensors is based on the shifts in the resonant frequency caused by the change in the electrical characteristics of the environment; in particular, the change in the effective permittivity (ε_{eff}) of the analyte solution [21, 22]. Metamaterial architectures can achieve higher resonance frequency shifts, leading to higher sensitivity and better linearity as compared to traditional RF structures [23].

Additionally, one of the key characteristics of SRRs is that the size of the resonator can be made smaller than the wavelength at the resonance. Thus, SRRs are suitable for use in miniaturizing planar microwave devices such as filters [24, 25] and antennas [26–28]. By using SRR, the operating resonant frequencies with respect to the size of the resonator can be significantly reduced ($< \lambda/20$) [28]. This is very important for sensing applications that involve transmission through soft tissue. It is reported in [29] that the measured body loss is increased by 5.1 dB as the operational frequency rises from 418 MHz to 916.5 MHz for a vaginally located source within a human body. Furthermore, since biological tissues mainly consist of water, they behave neither as a conductor nor as a dielectric, but as a dielectric with losses. Nicolas *et al.* (2003) reported that the conductivity of the muscle varies from 0.3211 S/m to 0.9982 S/m as frequency rises from 1 kHz to 1 GHz. Therefore, as the operating frequency increases, losses in the soft tissue increase. This makes SRRs very suitable for telemetric sensing applications since it is possible o obtain relatively low resonance frequencies with small sized resonators [30].

1.3. Application Area: Glaucoma Monitoring

1.3.1. Glaucoma

Glaucoma is reported as the second leading cause of blindness as it affects the optic disc and damages the optical nerve due to elevated IOP [31]. There are two major types of glaucoma, which are primary open-angle glaucoma and closed angle glaucoma. The former is the most common type, which develops because of the blocked drainage system in the front eye. As a result, aqueous humor builds up in the eye and this damages the optical nerve gradually by increasing IOP. Open-angle glaucoma is a painless and insidious disease, which may not be detected until the disease damages the optic nerve irreversibly. The latter type of glaucoma, closed-angle glaucoma, shows itself with an acute attack which may cause blindness suddenly because of the rapid increase in IOP. Closed-angle glaucoma happens if the individual's iris is close to the drainage system. This disease develops very slowly and, in many cases, undetectably until the iris completely blocks the drainage canals. [32–34]

1.3.2. Glaucoma Monitoring Methods

There are several methods to diagnose glaucoma, such as measuring peripheral vision, examining the optical nerve, measuring central corneal thickness, and measuring IOP [35–39]. Currently, measuring IOP using Goldmann applanation tonometer (GAT) is the most common method to monitor glaucoma disease [39]. To measure IOP by using GAT, a patient should go to the hospital every time for instantaneous measurements. However, to improve the diagnosis and the management of the disease, continuous data on the behavior of IOP is needed including data obtained during the night at sleep. However, GAT cannot provide this continuous data. Moreover, the tip of the GAT should be in direct contact with anesthetized cornea (Figure 1.1) [40] to measure IOP correctly, which is a very cumbersome method for the patients.

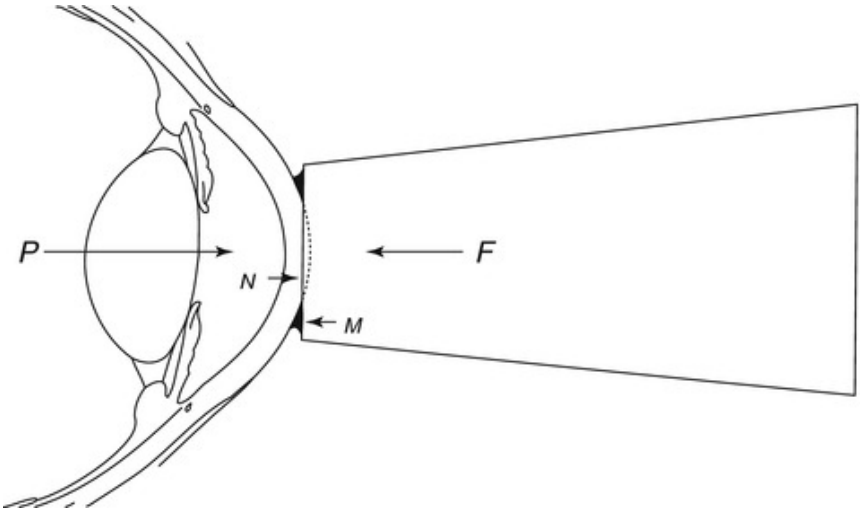

Figure 1.1. Illustration of IOP measurement with GAT [40].

A promising approach to monitor the progress of the disease is to monitor the IOP continuously, and several invasive and noninvasive devices have been developed for this approach. One of the examples of the invasive sensors to monitor glaucoma is given in Figure 1.2. Chen *et al.* (2010) presented an implant-based wireless pressure sensor for IOP monitoring and an implantable biocompatible material based pressure sensor is designed for this application [41].

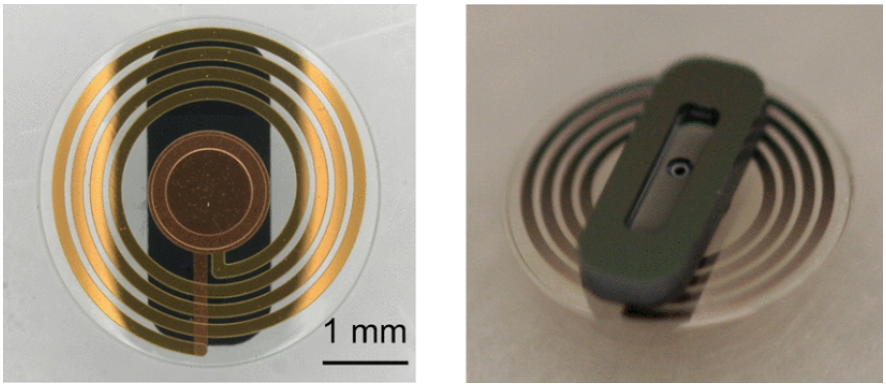

Figure 1.2. Microfabricated flexible-coiled wireless pressure sensor with its (left) top and (right) bottom views [41].

Microfabricated flexible coiled wireless pressure sensor given in Figure 1.2 is basically an inductor-capacitor (LC) tank resonant circuit with inductive coils and the pressure sensitive parallel plate capacitor at the center of the device. The shift in the resonant frequency of the sensor is measured with an external reader coil wirelessly by measuring the impedance phase difference. The resonant frequency is designed to decrease with increasing aqueous humor pressure in the eye due to the increase in the capacitance of the LC tank resonant circuit. The sensor is microfabricated on the parylene C flexible substrate using MEMS fabrication methods. Chen *et al.* (2010) presented an LC tank-based wireless pressure sensor for IOP monitoring and the disadvantage of this application is that the surgery is needed to implant this device into the front part of the eye, which is an invasive method to measure IOP.

Leonardi *et al.* (2004) presented a minimally invasive approach to IOP monitoring based on a sensing CL [42]. In this application, a microfabricated strain gauge is embedded into a soft CL to measure of changes in the corneal curvature correlated to variations in IOP. A photograph of the sensing CL is given in Figure 1.4. Sensing resistive gauges are placed circumferentially for sensing the changes in corneal curvature due to the variations in the IOP and compensation gauges are placed for thermal compensation. The data is transmitted through the micro-flex connection cable which however makes this sensor an active sensor and reduces the comfort for a patient.

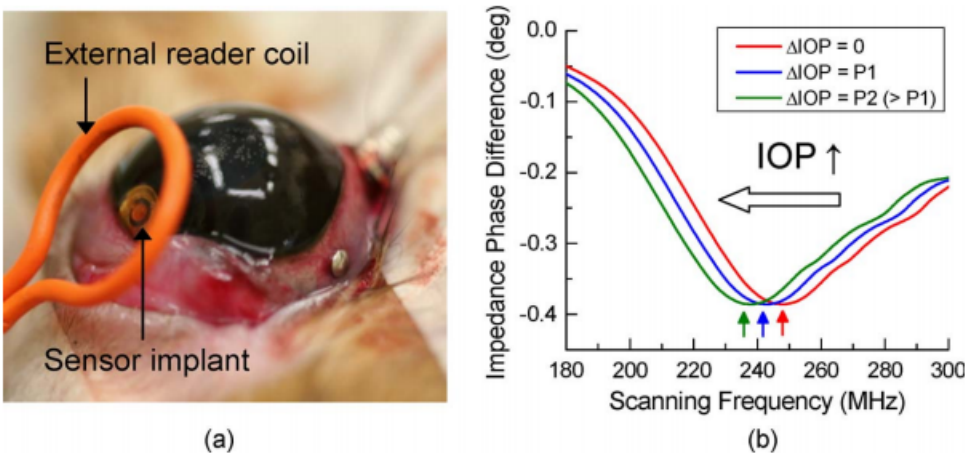

Figure 1.3. (a) Experimental setup for in vivo pressure sensing test (rabbit),(b) measured phase-dip curves [41].

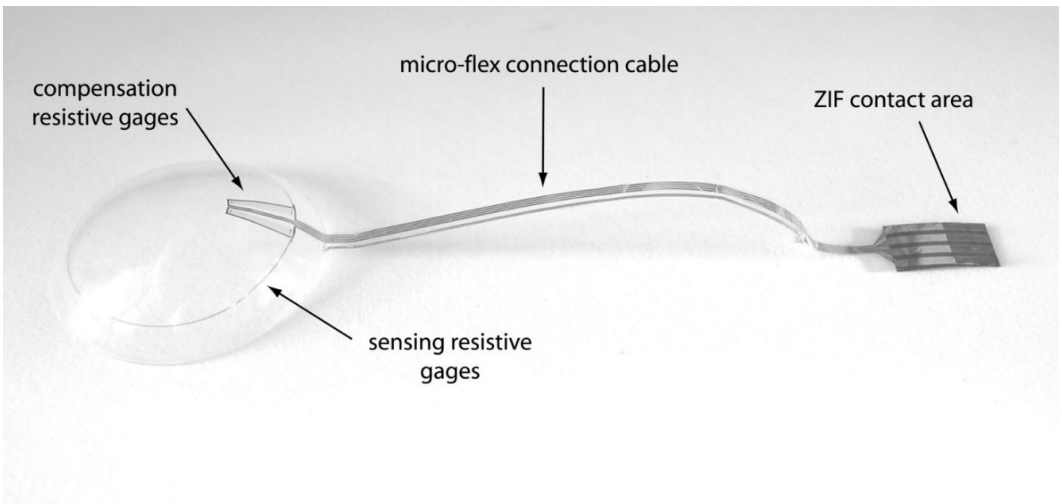

Figure 1.4. Photograph of the sensing CL [42].

The gauges of the sensor are made of thin metallic film patterned by surface micromachining on a polyimide flexible substrate. The sensor is embedded into silicone CL. And then, the CLS (contact lens sensor) is tested on enucleated porcine eyes and the measurements are compared to the ones from a needle pressure sensor. The IOP is changed by pumping normal saline water into the enucleated porcine eye. Output signal data are recorded by a data-processing unit. The results demonstrate that the output signal of the device showed a linear fit with the IOP mmHg with linear regression, $R^2 = 0.992$. The sensitivity of the sensing contact lens is reported as <0.5 mmHg with decreasing the noise in the output signal to $\pm 1\,\mu$V. However, as mentioned before, the sensing device has a wire for power transfer, which may cause discomfort for the patient.

To overcome the drawback of the presence of the wires required for power transfer, Leonardi *et al.* (2008) presented a new sensing device to measure the variations in the IOP for glaucoma monitoring [43]. A photograph of the CLS can be seen in Figure 1.5. For this new sensor application, they kept the active strain gauges and passive gauges for sensing the variations in the corneal curvature and thermal compensation, respectively. Moreover, they removed the wire and included a microprocessor chip and an antenna for data transmission and powering. However, the thickness of microprocessor may cause increasing the thickness of the CLS.

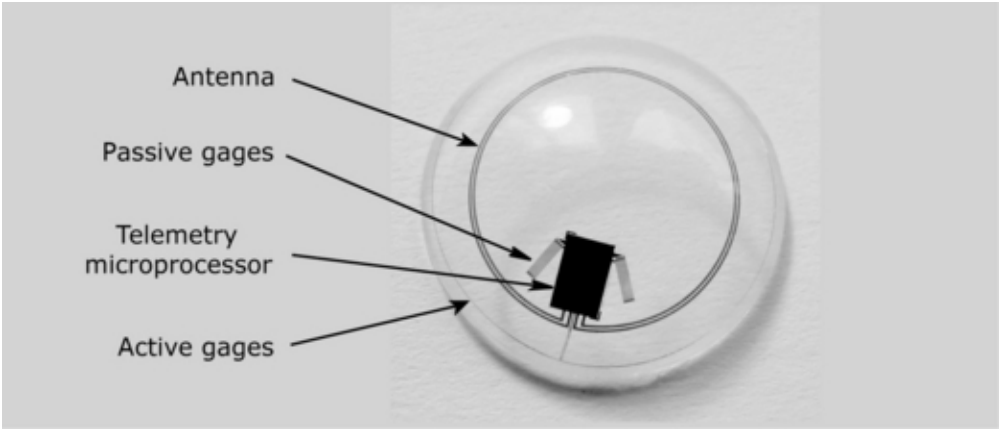

Figure 1.5. A photograph of the CLS [43].

1.3.3. SRR Based Sensors

Ekinci *et al.* (2016, 2017) presented split-ring resonator (SRR) based strain sensor for glaucoma detection application [44, 45]. In this application, an electrically passive, wireless and low-cost sensor to measure IOP was presented and the geometry of the sensor was optimized such that the resonant frequency of the sensor varies with the change in the ROC due to the variations in IOP. The device is realized on a flexible latex rubber substrate with silver conductive ink and Ekinci *et al.* (2016, 2017) have showed that the device exhibited monotonic variation in the resonant frequency with respect to the change in ROC.

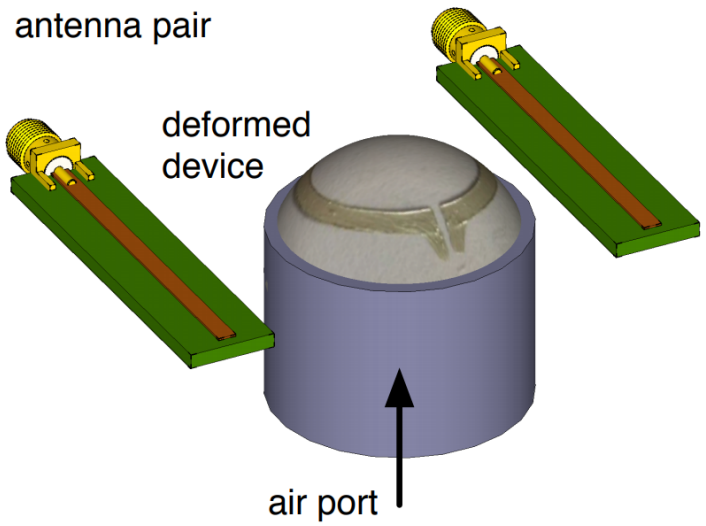

Figure 1.6. An illustration of the experimental setup for the SRR sensor realized on flexible latex rubber [44].

As can be seen in Figure 1.6, a pair of monopole antennas were used to detect resonant frequency of the sensor by measuring the transmission spectrum. The latex rubber substrate was stretched on top of a cylindrical injection syringe and the SRR structure is painted on the substrate using hard mask. The ROC of the device was changed by pumping air in and out of the device by using this syringe. Ekinci *et al.* (2016, 2017) suggested that SRR based sensors are promising applications for diagnosis of glaucoma. SRR sensors realized on flexible substrates can be integrated

to soft contact lens for fully passive, noninvasive method for continuous measuring of IOP wirelessly.

Calikoglu *et al.* (2017) presented a biosensor based on laser-machined metallic split-ring resonators embedded in hydrophilic polymer matrices for glaucoma monitoring [2]. The SRR sensors are fabricated by laser cutting of 15 μm-thick aluminum sheets and embedded into photo-polymerized cross-linked hydrogels, which are used to prepare hydrophilic polymer matrices. The dimensions of the SRRs are optimized to have resonant frequencies in the S-band. The localization of the SRR within a hydrogel based contact lens is determined at the point where the distension of the eyeball is maximum.

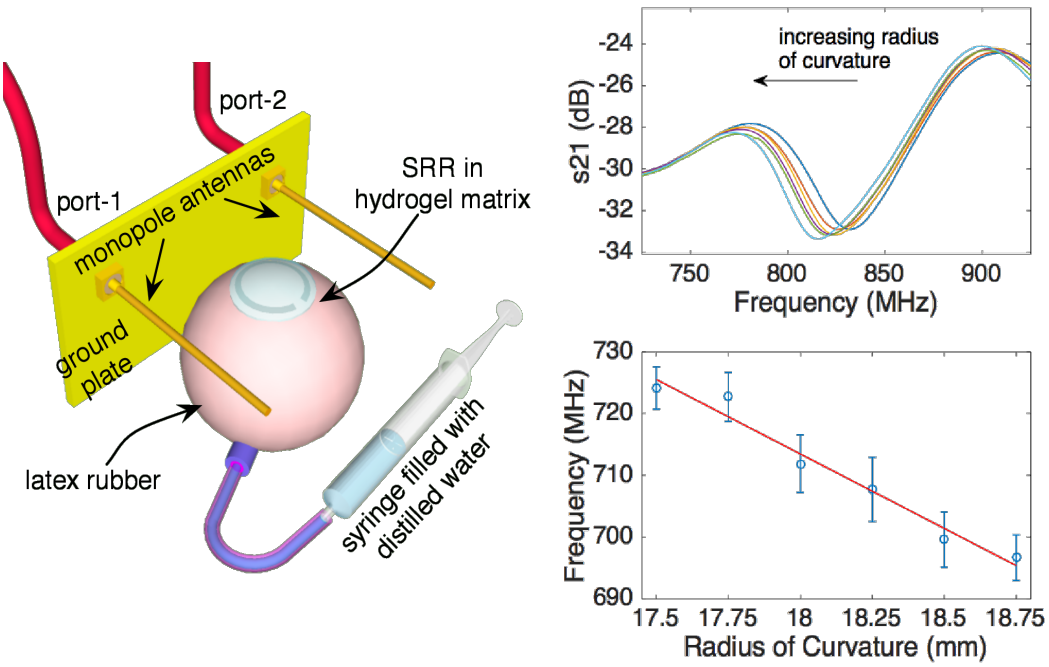

Figure 1.7. An illustration of the experimental setup for measuring the effect of curvature change [2].

In Figure 1.7, an illustration of the experimental setup is given. A spherically deformed latex rubber, which was filled with deionized (DI) water, was connected to a syringe using a medical pipe. The SRR embedded in hydrogel was placed on top

of the latex balloon and the curvature of the balloon was changed by pumping water in and out using a syringe. It is reported that the resonant frequency of the device exhibited monotonic change with respect to the change in the ROC, and the sensitivity was obtained as $-24.12\,\mathrm{MHz/mm}$. The demonstrated SRR based sensor was suggested as promising for non-invasive and continuous monitoring of glaucoma.

1.4. Thesis Contribution and Organization

The main objective of this thesis is to design and fabricate a biosensor to be embedded in a contact lens, which enables continuous monitoring of glaucoma to improve diagnosis accuracy and treatment of glaucoma. Organization of this thesis and contribution of this thesis to the previous work is listed below:

(i) SRR designed for glaucoma detection in the previous work [2,45] was further analyzed with finite difference time domain (FDTD) method simulations in Chapter 2.

(ii) Mechanical finite element model (FEM) simulations are shown in Chapter 2 which are performed for:
   - Contact lens (CL) placed on the fibrous layer of the anterior part of the eye to analyze the displacements of the CL caused by the IOP level given in Section 2.2.1 .
   - Bending processes of the resonators to be embedded in CL to analyze the feasibility of the fabrications given in Section 2.2.2.

(iii) Theoretical and simulation based analysis for tunable antennas are shown in Chapter 3.

(iv) In Chapter 4, broadside-coupled split ring resonator (BC-SRR) based CLSs which are coupled to the tunable antennas were designed and analyzed. BC-SRR based sensors were further analyzed with FDTD method in terms of metal thickness and substrate tangent loss. Further simulations were performed to analyze the resonance behavior of the CLSs on eye-globe for changing ROC levels.

(v) Fabrication of BC-SRR based CLSs and in-vitro characterization of the antenna coupled CLSs with respect to varying IOP levels are given in Chapter 5.

2. DESIGN AND SIMULATIONS OF SRR BASED SENSOR

2.1. Microwave Modeling of the Resonator

The SRR structure consists of a circular or rectangular metallic ring with a narrow gap. An external electromagnetic excitation can lead this structure to behave like a Resistor-Inductor-Capacitor (RLC) circuit. If the time-varying magnetic field (H) is transverse to the SRR surface, the magnetic field induces a circulating current on the ring surface, which creates another magnetic field that may enhance or oppose the incoming magnetic field. This results in a magnetic resonance at certain frequency f_0. At the resonant frequency, the SRR structures can exhibit negative permeability. The resonant frequency strongly depends on the electrical properties of the materials and geometry of the structure and is given by [14]:

$$f_0 = \frac{1}{2\pi\sqrt{LC}} \tag{2.1}$$

Here, L is the self-inductance of the split-ring made of conductive material and C is the sum of the gap and surface capacitances ($C_{gap} + C_{surf}$). Formulae of the self-inductance and capacitance of split ring resonators are given in Equation 2.2 [14]:

$$L = \mu_0 R_{\mathrm{m}} \left(\log \frac{8R_{\mathrm{m}}}{h+w} - \frac{1}{2} \right) \tag{2.2a}$$

$$C = C_{gap} + C_{surf} \tag{2.2b}$$

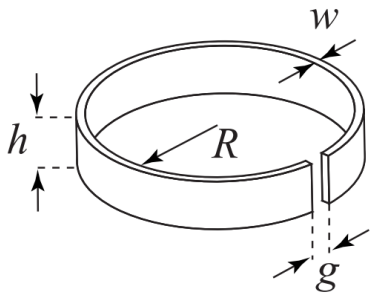

Figure 2.1. Split-ring resonator drawing [14].

where

$$R_{\mathrm{m}} = R + \frac{w}{2} \tag{2.2c}$$

$$C_{\mathrm{gap}} = \varepsilon_{eff}\left(\frac{hw}{g} + h + w + g\right) \tag{2.2d}$$

$$C_{surf} = \frac{2\varepsilon_{eff}(h+w)}{\pi}\log\frac{4R}{g} \tag{2.2e}$$

where R is the inner radius, R_{m} is the average radius, h is the height, w is the width and g is the gap distance of SRR (Figure 2.1). Table 2.1 shows the calculated resonant frequencies of the sensors with the self-inductance and capacitance values for different geometries and relative permittivities (ε_{r}) and thicknesses of the substrates ($h_{substrate}$). For the calculations, effective permittivity ($\varepsilon_{\mathrm{eff}}$) is calculated as below:

$$\varepsilon_{eff} = \frac{(\varepsilon_r + 1)}{\pi}\varepsilon_0 \arctan\left(\frac{8h_{substrate}}{w}\right) \tag{2.3}$$

where ε_0 is free space permittivity.

Table 2.1. SRR calculations.

	g (mm)	w (mm)	r (mm)	h (µm)	$h_{substrate}$ (mm)	ε_r(substrate)	C_{gap} (fF)	C_{surf} (fF)	C (fF)	L (nH)	f_0 (GHz)
1	1	1.5	4.5	30	1.5	4.3	55.06	60.83	115.89	18.55	3.43
2	1.5	1.5	4.5	30	1.5	4.3	65.73	52.29	118.03	18.55	3.40
3	2	1.5	4.5	30	1.5	4.3	76.47	46.24	122.71	18.55	3.33
4	1.5	1.5	4.5	30	1.5	4.3	56.40	36.21	92.61	19.85	3.71
5	1.5	2	4.5	30	1.5	4.3	74.47	67.43	141.90	17.81	3.16
6	1.5	2.5	4.5	30	1.5	4.3	82.64	81.63	164.27	17.34	2.98
7	1.5	1.5	4	30	1.5	4.3	65.73	49.82	115.55	16.19	3.68
8	1.5	1.5	5	30	1.5	4.3	65.73	54.51	120.24	20.98	3.17
9	1.5	1.5	4.5	10	1.5	4.3	65.12	51.61	116.73	18.55	3.41
10	1.5	1.5	4.5	20	1.5	4.3	65.43	51.95	117.38	18.55	3.41
11	1.5	1.5	4.5	40	1.5	4.3	66.04	52.64	118.67	18.55	3.40
12	1.5	1.5	4.5	30	1.5	3	49.67	39.47	89.14	18.55	3.91
13	1.5	1.5	4.5	30	1.5	2	37.32	29.60	66.92	18.55	4.52
14	1.5	1.5	4.5	30	1.5	1	24.97	19.73	44.70	18.55	5.53
15	1.5	1.5	4.5	30	1	4.3	62.97	50.09	113.06	18.55	3.47
16	1.5	1.5	4.5	30	2	4.3	67.13	53.41	120.54	18.55	3.37
17	1.5	1.5	4.5	30	2.5	4.3	67.97	54.08	122.06	18.55	3.34

2.1.1. SRR Simulations

The effect of the thicknesses and permeabilities of the metal parts of the SRR on the resonance behavior analyzed using finite difference time domain (FDTD) simulations. While analyzing the metal thickness and permeability, substrate thickness was selected as 50 µm and substrate material was chosen as polyimide (PI). Dielectric properties of PI are given in Figure 2.2 [46]. Based on this figure, relative permittivity (ε_r) was chosen as 3.4 and loss tangent ($\tan\delta$) of the substrate was chosen as 0.005 while doing the simulations.

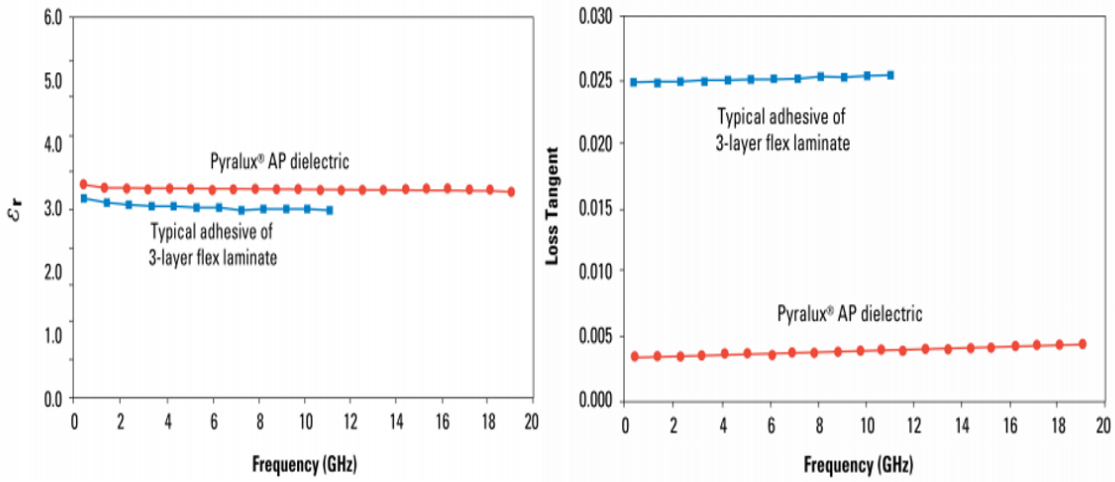

Figure 2.2. Dielectric properties of PI [46].

Moreover, saline water effect on SRR with Flame Retardant 4 (FR-4) substrate was also analyzed in Section 2.1.1.3. For these simulations monopole antenna pair is used and resonance behavior is analyzed on transmission (s_{21}) spectra.

2.1.1.1. SRR Metal Thickness Analysis. Simulations were performed using CST Microwave Software. For the simulations, g was 100 µm, R was 5 mm and w was 1.5 mm to keep the dimensions of the resonators so that they can be embedded in the contact lens.

Thickness of the metal is an important parameter while designing the sensor as it affects both mechanical performance of the sensor in terms of conformity to the cornea, and resolution of the sensor. To increase the conformity of the sensor to the cornea, substrate and also the metal layers should be chosen as thin as possible. However, decreasing the thickness of the metal increases the resistance, which decreases the Q factor and the resolution of the sensor.

While doing the simulations it is realized that changing the thickness of the metal layer to values thinner than the skin depth (δ_s) of that metal in CST Microwave Studio does not yield altered simulation results in terms of the Q. However, this cannot be true in reality. It is also realized that whatever the thickness of the metal layer modeled in CST Microwave Studio, the software defines the conductivity of the metal layer as a constant value which is the maximum conductivity of that metal at given frequencies. Therefore, to make the simulations more realistic, RF sheet resistance values are calculated for several thicknesses of gold and imported to the CST Microwave Studio as tabulated sheet resistance values of the defined new materials.

RF sheet resistance of gold for varying thicknesses is calculated using the formulae given below. First, δ_s is calculated from the formula:

$$\delta_s = \sqrt{\frac{\rho}{\pi f \mu}} \quad \text{(m)} \tag{2.4}$$

and RF conductivity (σ_s) at t is calculated using:

$$\sigma_s = \frac{e^{-t/\delta_s}}{\rho} \quad \text{(S/m)} \tag{2.5}$$

RF sheet conductance (G_s) can be calculated by integrating σ_s to a thickness of t:

$$G_s = \frac{1}{\rho}\int_0^t e^{-\frac{t}{\delta_s}} dt = \frac{\delta_s}{\rho}\left(1 - e^{-\frac{t}{\delta_s}}\right) \quad \text{(Ssq)} \tag{2.6}$$

therefore, RF sheet resistance (R_S) is:

$$R_s = \frac{1}{\frac{\delta_s}{\rho}\left(1 - e^{-t/\delta_s}\right)} \quad (\Omega/\text{sq}) \tag{2.7}$$

where t is the thickness of the metal (m) and ρ is bulk resistivity ($\Omega\,\text{m}$).

The calculated sheet resistance values for various various sheet thickness of gold vs frequency can be seen in Figure 2.3(a). ρ of gold is defined as $2.24\,\mu\Omega\,\text{cm}$. Moreover, the effect of the frequency on RF sheet resistance can be seen in Figure 2.3(a) and Figure 2.3(b).

s_{21} spectra with respect to varying values of metal thickness are given in 2.4(b) for the model depicted in Figure 2.4(a). As can be seen in the simulation results, decrease in the thickness of the metal layer decreases Q of the resonator due to the increase in the RF sheet resistance. Also, given the simulation results, we can say that results are converged in terms of Q when the thickness is increased to 1 µm; however, Figure 2.3(b) shows that at 3 GHz, RF sheet resistance continues to decrease when the thickness is increased to values higher than 1 µm. This can be explained by the loss parameter of the substrate. Consequently, the Q is limited due to the dielectric loss of the substrate.

As a result, using very thin metals for the resonators reduces the performance of the sensor system as the Q decreases with increasing resistance, which in turn lowers the resolution of the sensor. Also, dielectric loss of the substrate is important parameter as it limits the Q.

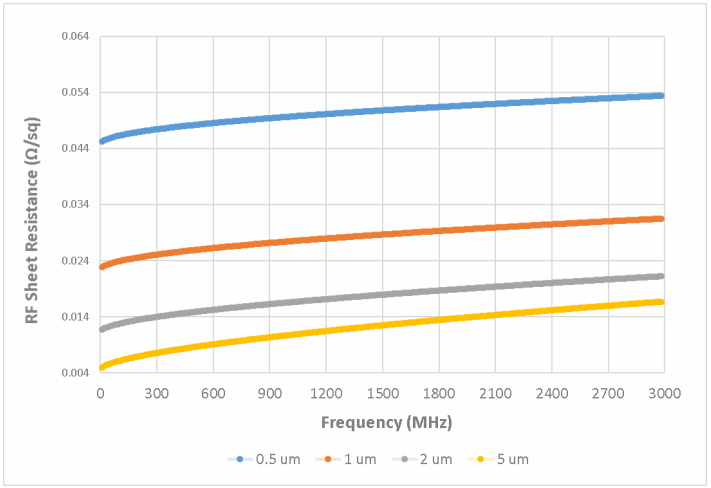

(a)

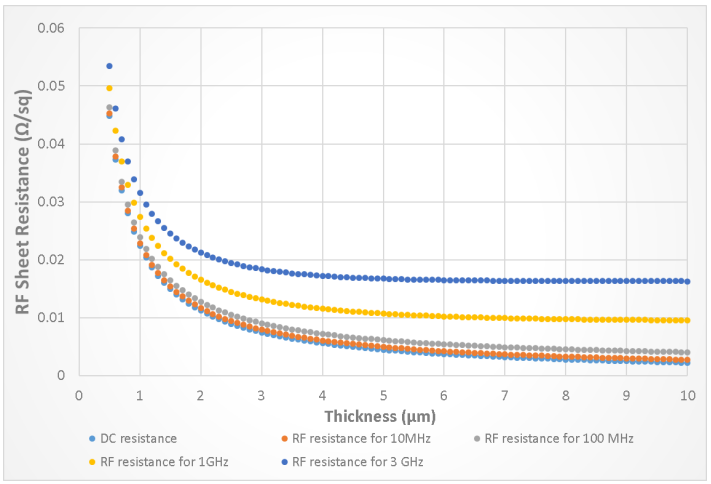

(b)

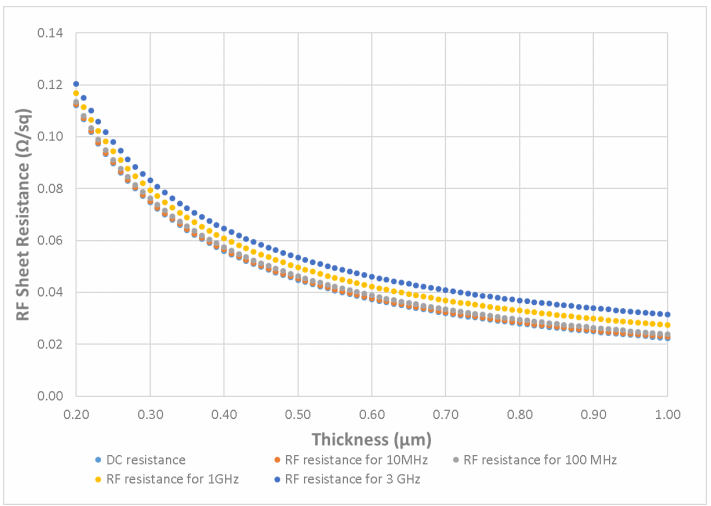

(c)

Figure 2.3. Calculated RF sheet resistance values for (a) various sheet thickness of gold vs frequency, (b) and (c) various frequencies vs gold thickness.

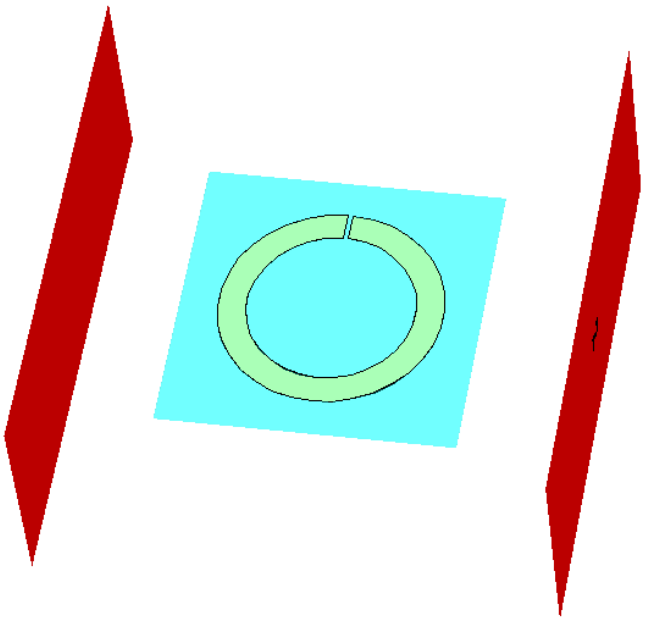

(a)

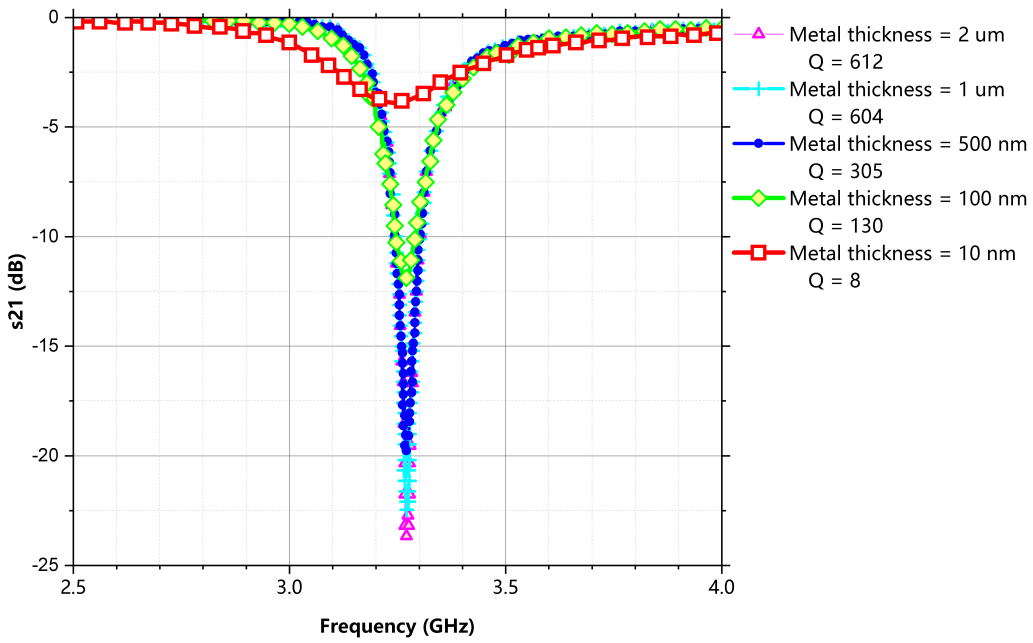

(b)

Figure 2.4. (a) Simulation model and (b) s_{21} spectra of simulated model for various thicknesses of gold.

2.1.1.2. SRR Metal Permeability Analysis. The effect of metal permeability on the resonance behavior of the SRR was analyzed with simulations using FDTD method. Conductivity of the metal was chosen as 4.1×10^7 S/m and permeability was changed parametrically to see its effect.

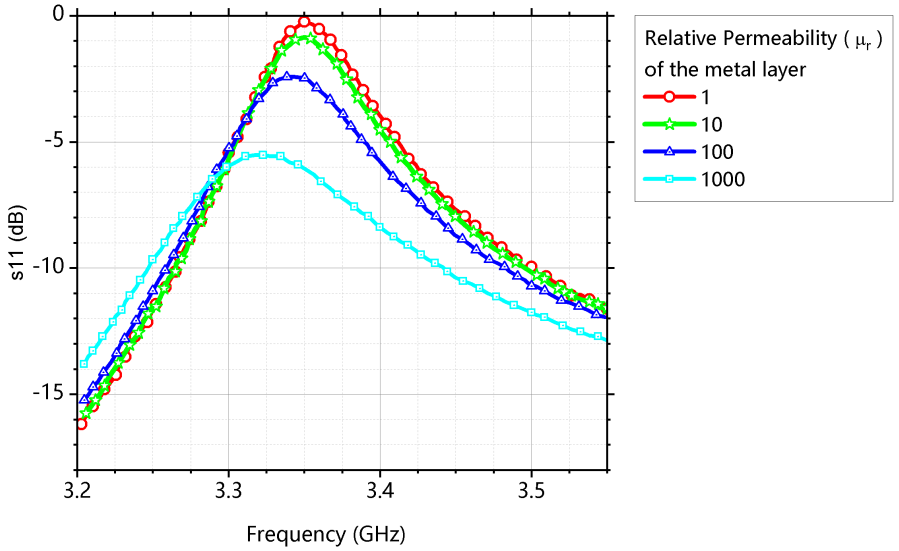

(a)

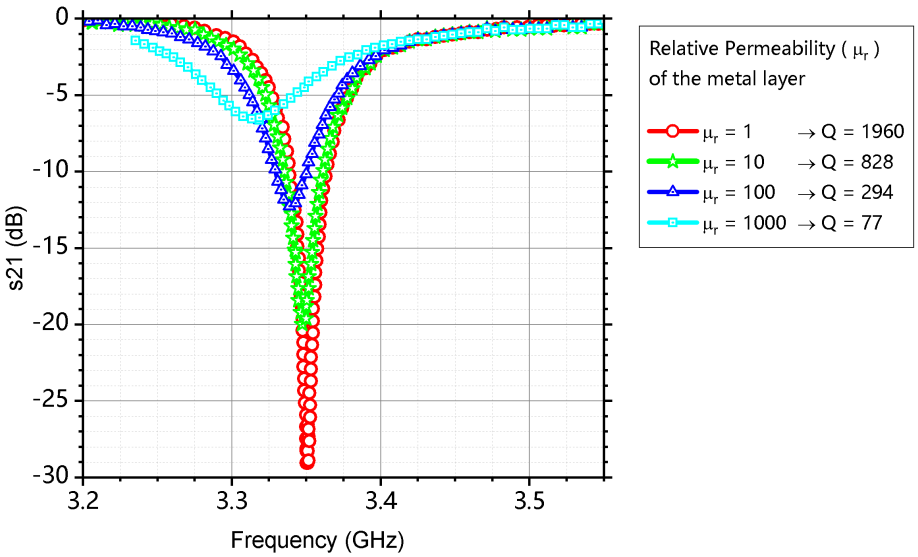

(b)

Figure 2.5. Simulated (a) s_{11} and (b) s_{21} spectra for varying values of permeability of metal layer.

s_{11} and s_{21} spectra with respect to varying values of permeability of metal are given in Figure 2.5(a) and Figure 2.5(b), respectively. As can be seen in the simulation results, increase in permeability of metal layer, decreases Q of the resonator due to the decrease in the δ_s which increases RF sheet resistance (Equation 2.7). As a result, using magnetic metal layers for the resonators reduces the performance of the sensor system as the Q factor decreases with increasing resistance, which in turn lowers the resolution of the sensor as the resolution of the sensor depends on the amount of the shift and the sharpness of the signal (high Q).

2.1.1.3. SRR Saline Water Effect Analysis. Saline water effect on SRR with FR-4 substrate was also analyzed using CST Microwave Studio simulations. For these simulations monopole antenna pair is used and resonance behavior is analyzed on s_{21}. For the simulations, g was 1 mm, R was 4.5 mm, w was 1 mm and h was 25 µm for SRR. FR-4 (lossy) substrate is chosen from the material library of CST Microwave Software and thickness of the substrate was defined as 1.5 mm.

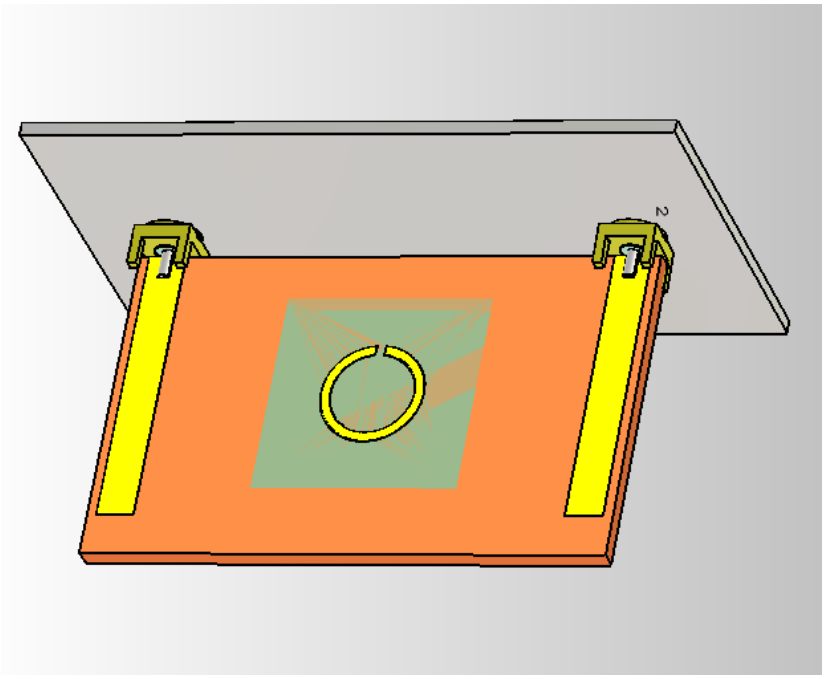

Figure 2.6. Illustration of the monopole antenna pair coupled SRR on FR-4 with water layer.

Figure 2.6 shows the illustration of the simulated monopole antenna pair coupled SRR with additional water layer on top of the SRR. For the simulations ε_r of the water layer was defined as 80 and the thickness of the layer was defined as 40 µm to mimic the tear fluid whose thickness reported in the literature ranges from about 4 µm [47] to 40 µm [48].

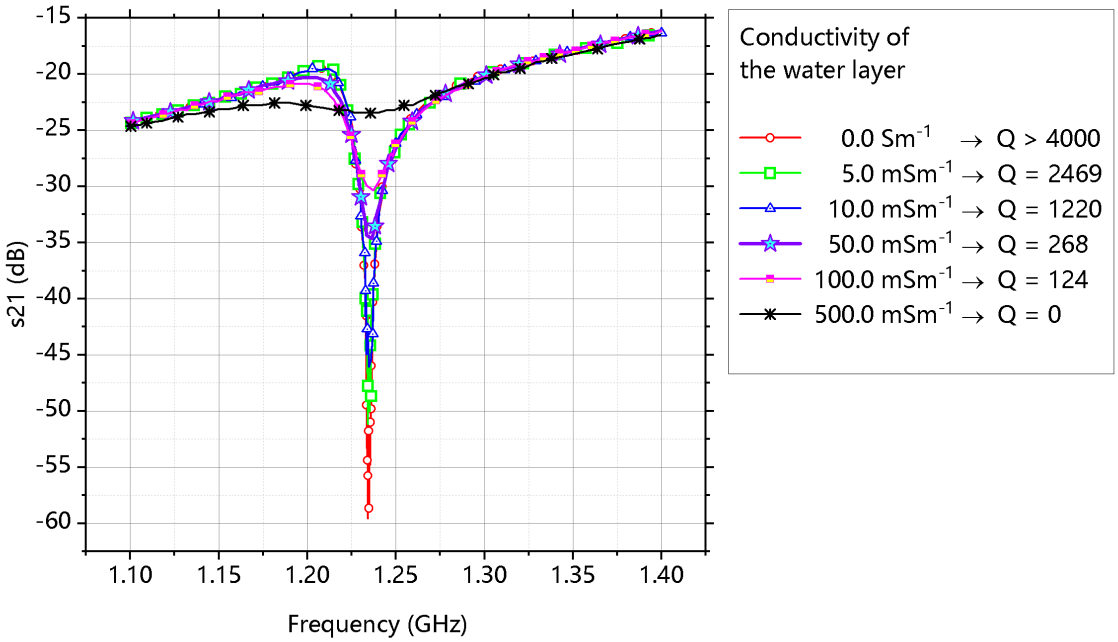

Figure 2.7. Simulated s_{21} spectra for varying values of conductivity ($S\,m^{-1}$) of defined water layer.

Figure 2.7 shows the simulation results for varying conductivity levels of defined water layer ($S\,m^{-1}$). As can be seen from the simulation results, the Q of the sensor decreases as the conductivity ($S\,m^{-1}$) of defined water layer increases. Decrease in the Q is very dramatic when the conductivity of the water increases to $0.5\,S\,m^{-1}$. However, around 1 GHz conductivity values of the eye tissues are higher than $0.5\,S\,m^{-1}$, reported in [49].

The decrease in the Q of the resonator is due to the decrease in the Q of the self-capacitance (both C_{surf} and C_{gap}) of the SRR since the dielectric layers of the capacitances are deteriorated by conductivity. Therefore, using the SRR around the

eye tissues would only be possible with thick dielectric layer isolation, which is not suitable for this application.

2.2. Mechanical Eye Model Simulations

Calikoglu *et al.* (2017) showed the mechanical eye model in [2]. In this work, an axisymmetric finite-element model, for the fibrous layer of the eye was modeled to investigate the effect of the change in the IOP on the cornea. It has been shown that 1 mmHg change in the IOP corresponds to 4 µm change in the ROC.

2.2.1. Contact Lens placed on Eye Model

For this thesis, same model for the fibrous layer of the anterior part of the eye is used. Moreover, CL placed on the fibrous layer of the eye was modeled to investigate the effect of the change in the IOP on the cornea and CL. CL material is defined as polydimethylsiloxane (PDMS). Figure 2.8(a) shows the computational model including an eyeball and a contact lens. The thickness of the CL is 200 µm in this model.

Figure 2.9(a) shows the deflection profile for a selected simulation when the change in IOP level is 5 mmHg. Red arrows illustrate the normalised displacements when apical displacement is set to 0. Moreover, tangential displacement lines can be seen in Figure 2.9(b). Maximum change in the ROC for the CL is obtained at $r = 5 \pm 0.5$ mm. The dimensions of the sensors (Section 2.1) are determined based on this value so that the displacement on the sensor is maximized with respect to change in the IOP.

Deformation profiles are compared for CLs with thicknesses of 100 µm and 200 µm. Figure 2.8(b) shows maximum displacement values obtained from the simulations on the cornea and CL with respect to changes in IOP levels. The slopes of the trend lines indicate the change in the ROCs for a 1 mmHg change in the IOP. 1 mmHg change in IOP corresponds to 4 µm change in the ROC. Moreover, the results of the simulations indicate that thickness variation within 100 µm to 200 µm range do not have significant

effect on the deformation of CLs.

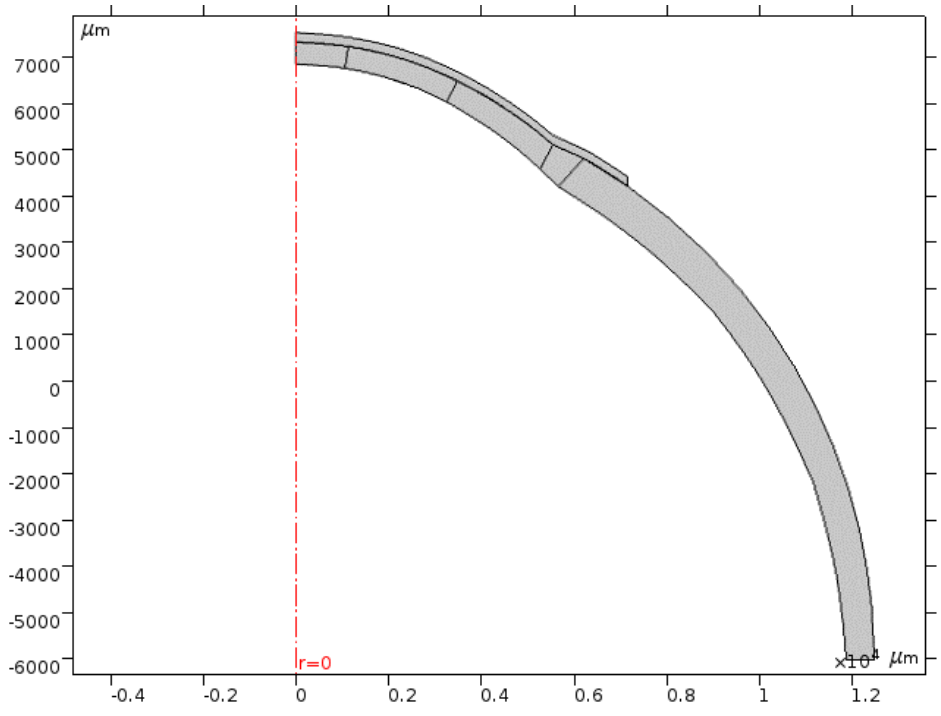

(a)

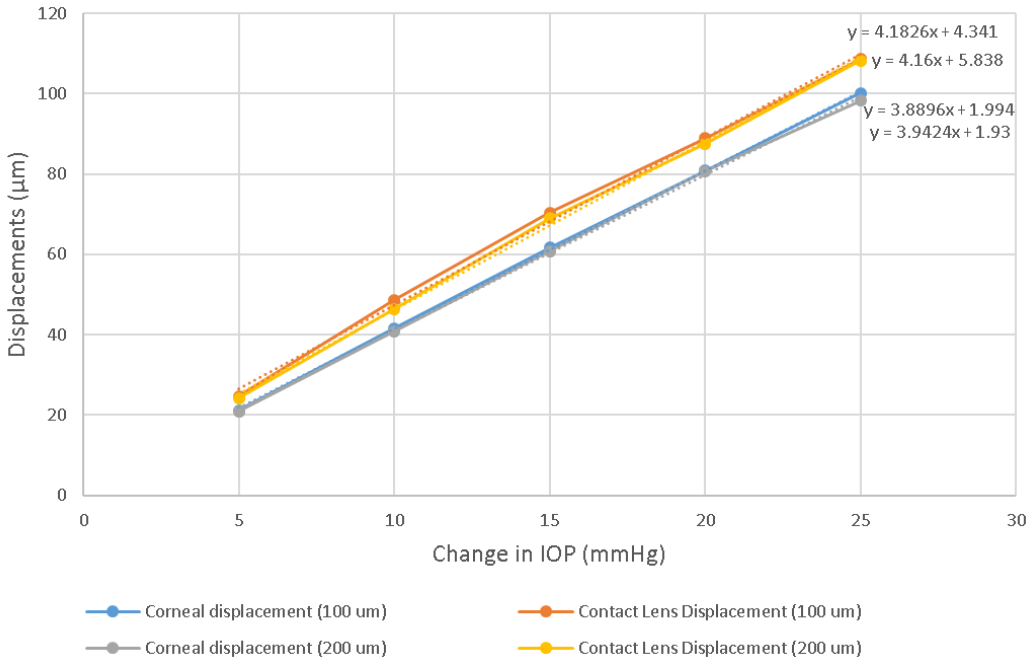

(b)

Figure 2.8. (a) Computational model including an eyeball and a CL, (b) maximum displacement values for CLs with thicknesses of 100 µm and 200 µm with respect to changes in IOP levels.

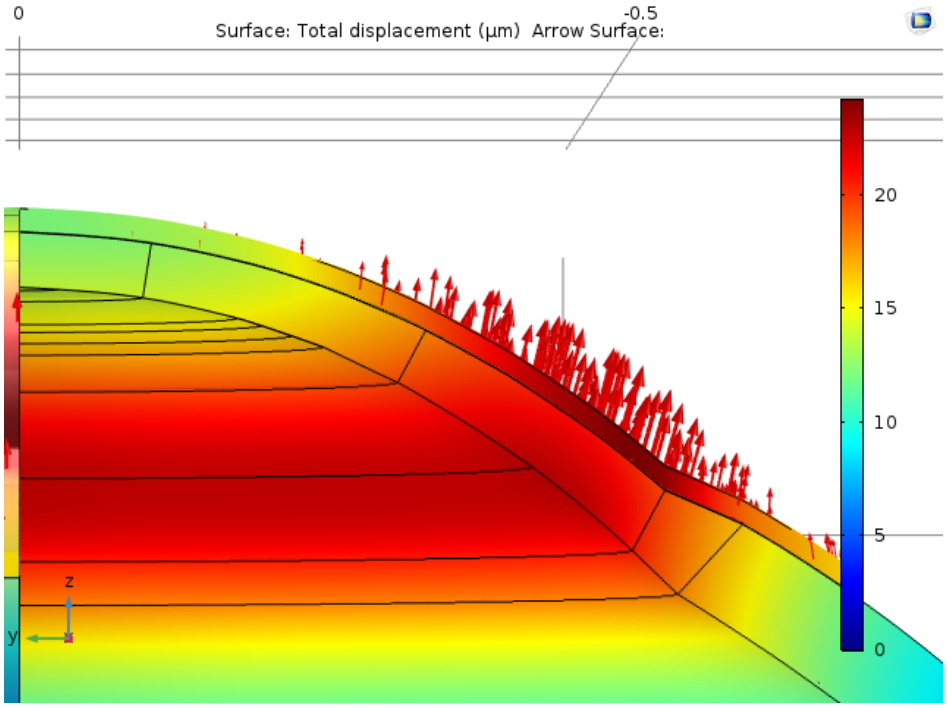

(a)

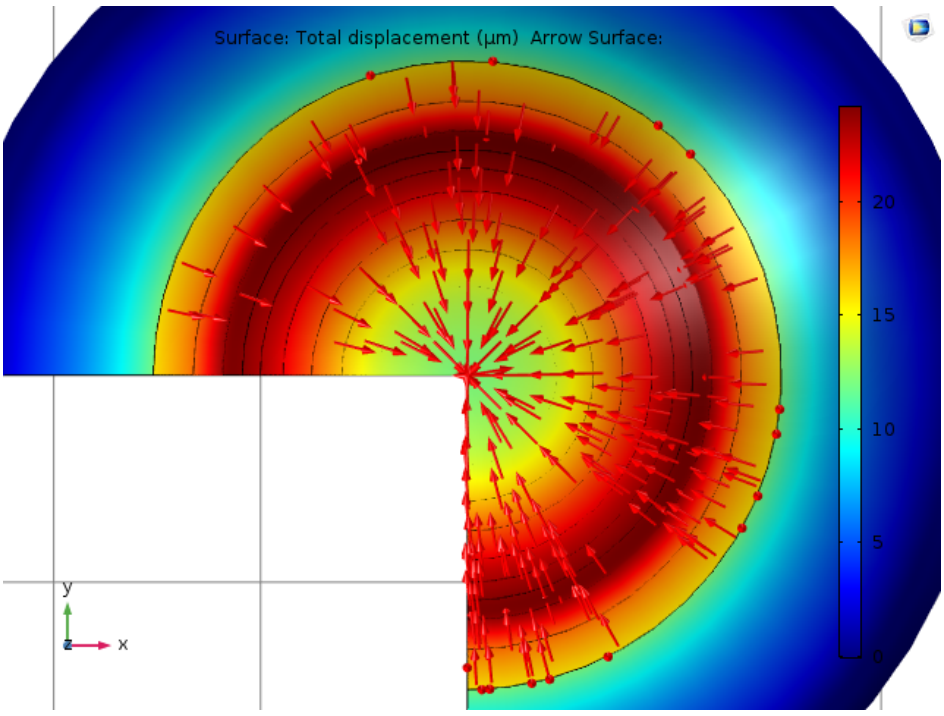

(b)

Figure 2.9. The deflection profile for the simulation when the change in IOP level is 5 mmHg. Red arrows illustrate (a) the normalised displacements when apical displacement is set to 0, (b) tangential displacements on CL model.

2.2.2. Contact Lens Embedded Sensor

Fabricated sensors were placed in a CL having a typical shape designed to fit the cornea. In order to embed fabricated planar sensors in the CL, it was necessary to bend them first. It is decided to bend the sensors by molding. Therefore, an axisymmetric FEM model was designed in COMSOL software to analyze the mechanical feasibility of the molding process of the sensors. In these simulations, stainless steel molds were approaching each other and bending PDMS and PI substrates with embedded metal ring. The gap of the SRR was excluded for the simplicity of the simulations.

2.2.2.1. SRR Embedded in PDMS: Stress Simulations. 100 nm ring resonator was placed in the middle of 50 µm thick PDMS substrate. Stress-strain behavior of the PDMS and gold are given in Figure 2.10(a) [50] and Figure 2.10(b) [51], respectively. Maximum stress values obtained from the simulations are evaluated using these behaviors.

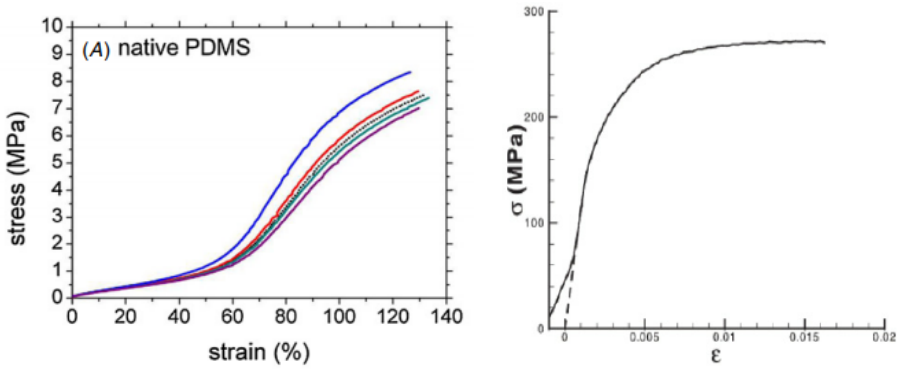

(a) (b)

Figure 2.10. Stress-strain curve for (a) native PDMS [50] and (b) for gold [51].

Figure 2.11(a) shows that the maximum stress on PDMS substrate is about 1.3 MPa which is in the linear region for native PDMS (Figure 2.10(a)). Moreover, the stress result of the metallic ring which is embedded in PDMS substrate is excluded and results are given in Figure 2.11(c). The maximum stress value on 100 nm gold ring was found to be around 0.6 MPa, which is a relatively small stress value for gold (Figure 2.10(b)). Therefore, it is concluded that the result of the molding process can be done without damaging the planar sensor.

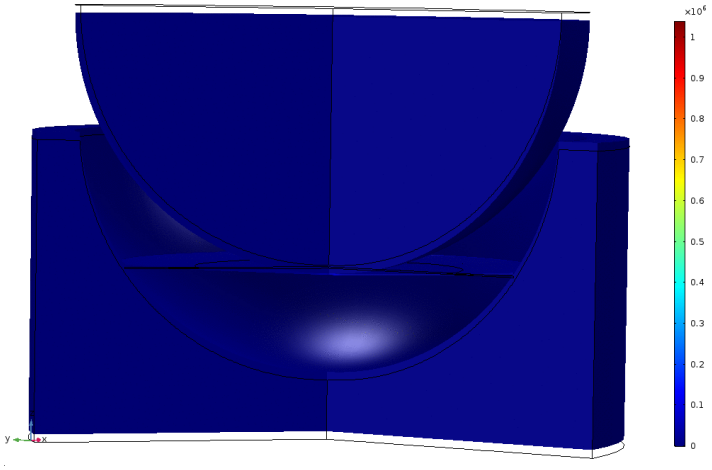

(a)

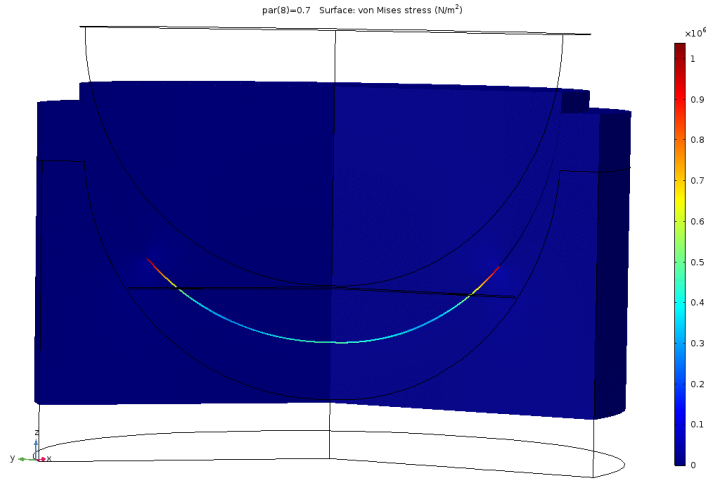

(b)

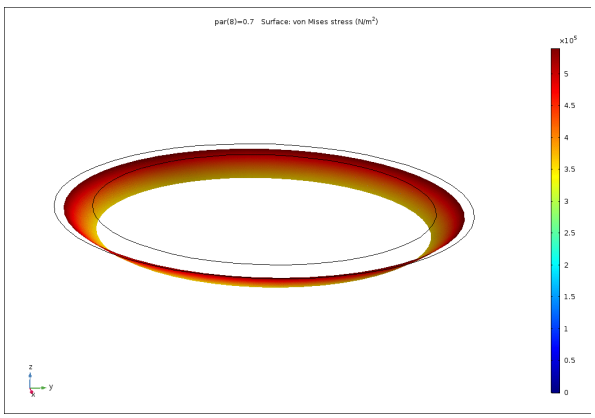

(c)

Figure 2.11. Stress distribution on (a) PDMS when PDMS is not bent, (b) PDMS when PDMS is bent and (c) 100 nm gold ring.

2.2.2.2. SRR Embedded in Polyimide: Stress Simulations. 5 µm thick ring resonator was placed in the middle of 50 µm thick PI substrate. Maximum stress values obtained from the simulations were also evaluated for SRR embedded in PI.

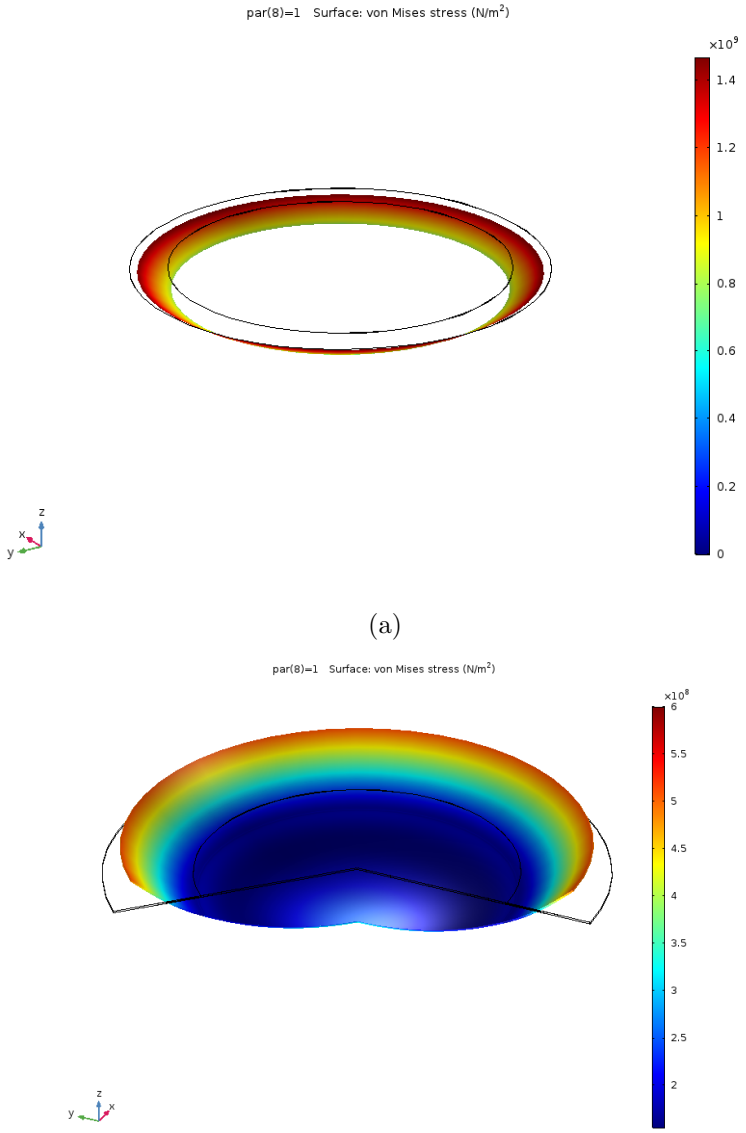

Figure 2.12. Stress distribution on (a) PI when PI is bent, (b) 5 µm thick gold ring.

The result of the stress simulations of the metallic ring which is embedded in PI substrate is given in Figure 2.12(a). The maximum stress value on 5 µm thick gold ring was found to be around 1.3 GPa, which is very high value for gold and it is above the ultimate strength (Figure 2.10(b)). While performing the simulations,

the materials were defined as linear elastic materials. With the obtained stress value, we can conclude that bending the sensors cannot be performed without damaging the planar sensor. Moreover, Figure 2.12(b) shows the maximum stress on PI substrate is about 600 MPa which is also above the yield strength of the polymer [52]. Therefore, results show that while bending PI, it will undergo plastic deformation.

2.3. Fabrication of SRR Embedded in PDMS

Fabrication processes were done in the clean room located in Boğaziçi University, Kandilli Campus. Spin coating, lithography, etching and sputtering were used in various steps of fabrication. The process flow of the fabrication of SRR embedded in PDMS is given in Figure 2.13 and fabrication steps are explained in detail below:

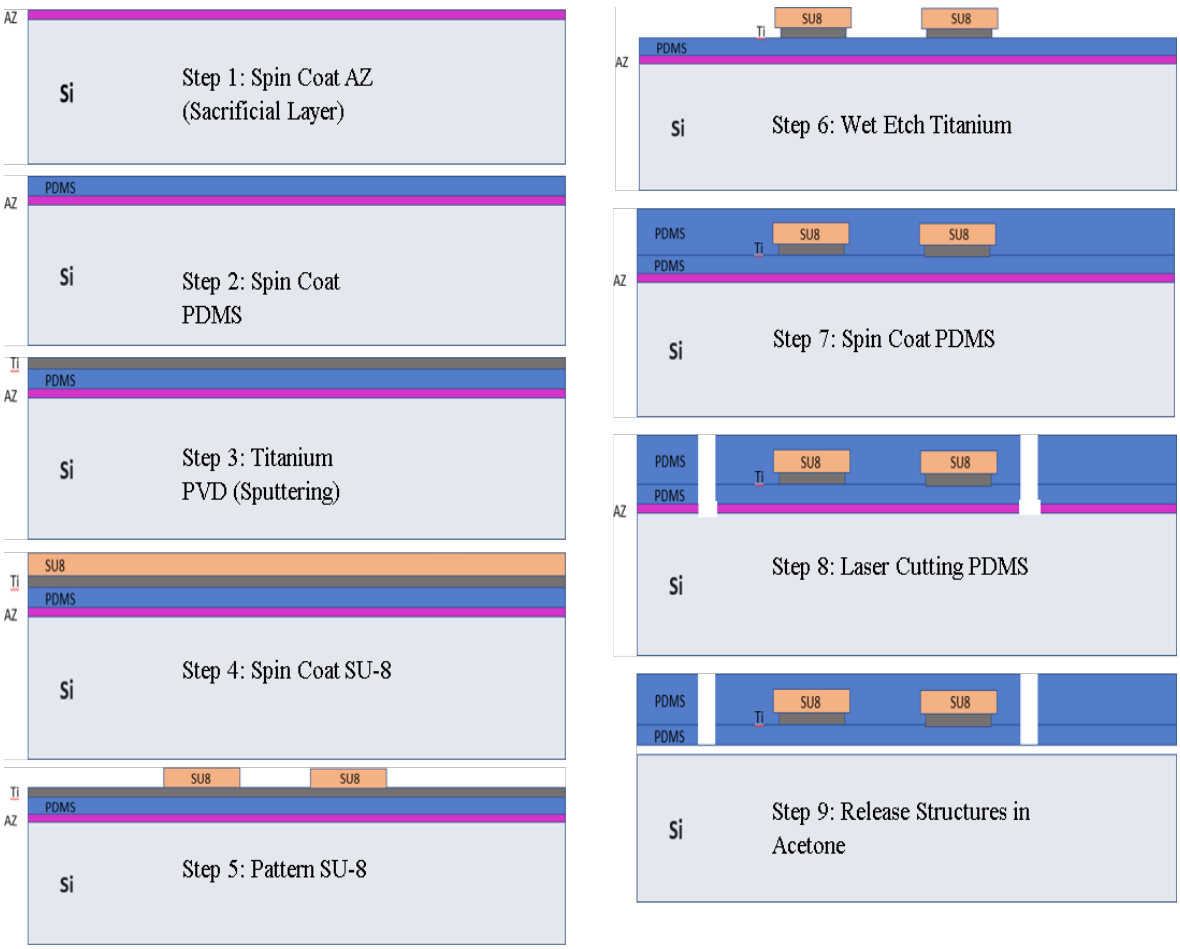

Figure 2.13. SRR embedded in PDMS fabrication process flow.

After cleaning of the wafer using piranha solution and rinsing, the wafer is dried using Nitrogen (N_2) gun and hot plate at 200 °C for 20 min. Oxygen (O_2) plasma is applied onto the wafer at 200 mTorr, 70 W for 10 min to clean carbon contaminants. Then, as a sacrificial layer AZ 5214 is spin coated (500 rpm for 30 s and 300 rpm for 1 min) on the wafer, pre-baked at 110 °C for 50 s and patterned with 40 mJ cm^{-2} exposion dose [53].

PDMS (Sylgard 184) is prepared by mixing the PDMS prepolymer and the curing agent at weight ratio of 10:1. Mixture is stirred well and degassed under a vacuum for 15 min. Degassed 5 mL of PDMS is dispensed onto the sacrificial layer. Then, 2 step spin coating is applied. Then the mixture is cured at 70 °C for 35 min [54] and thickness of obtained PDMS layer is measured in the clean room using surface profiler. In Figure 2.14 PDMS spin coating recipe is given [55]. Table 2.2 shows experimental results of PDMS spin coating in clean room.

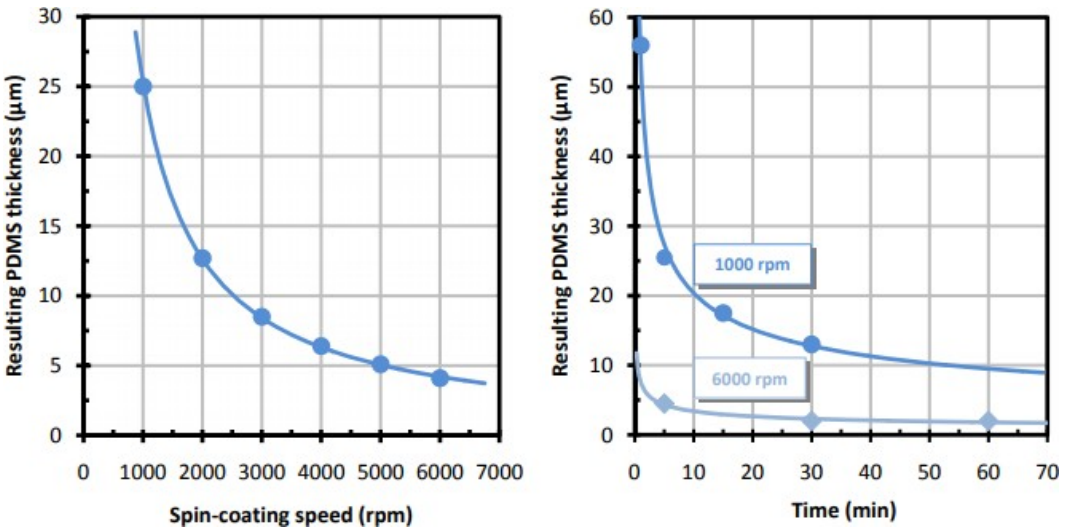

Figure 2.14. PDMS spin coating recipe [55].

After PDMS curing, O_2 plasma is applied at 200 mTorr and 70 W for 3 min, the wafer is left in sputter device for metal deposition at 100 W for 140 min. Baratron gauge is set to 3 mTorr, combined pressure to 20 mTorr. 280 nm thick titanium (Ti) is obtained after sputtering process. However, sputtering Ti on PDMS produced a cracked surface.

Table 2.2. Experimental results of PDMS spin coating in the clean room.

	Velocity (rpm)	**Time** (s)	**Velocity (rpm)**	**Time** (s)	**Thickness** (µm)
1	500	25	3000	30	77
2	200	10	1000	300	58
3	200	10	1000	350	53.5
4	200	5	1000	500	50
5	400	25	4000	100	20

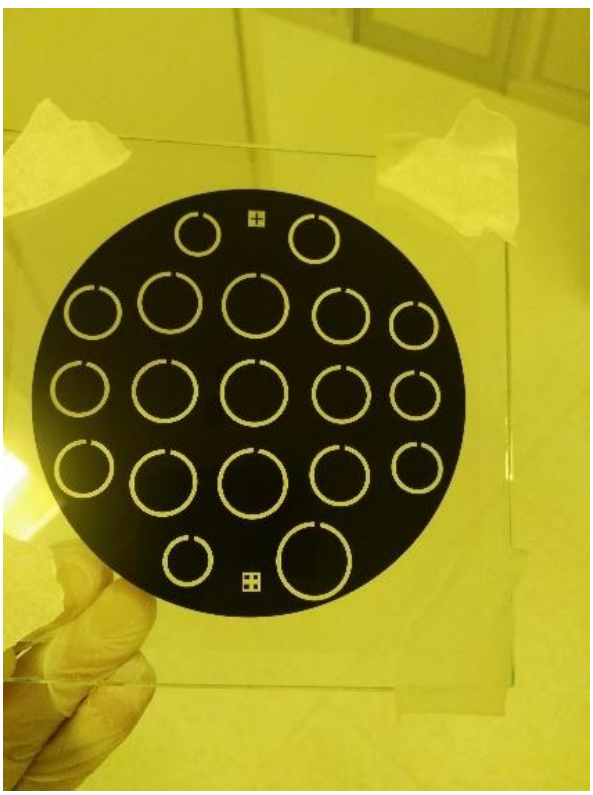

Figure 2.15. Dark field mask strapped on a glass substrate.

5 mL SU-8 is dispensed onto Ti layer and spin coated (800 rpm for 20 s and 7500 rpm for 150 s). Then spin coated SU-8 is soft baked in two steps (65 °C for 3 min and 95 °C for 9 min) [56]. SU-8 is then patterned with dark field mask which was printed on acetate and strapped on a glass substrate (Figure 2.15). For SU-8, exposi-

tion dose is set to 120 mJ cm^{-2}. In the end SU-8 is post baked in two steps again (65 °C for 2 min and 95 °C for 7 min) [56]. The wafer is then immersed into SU-8 developer for 7 min and cleaned. Therefore 20 µm thick SU-8 is obtained onto Ti layer.

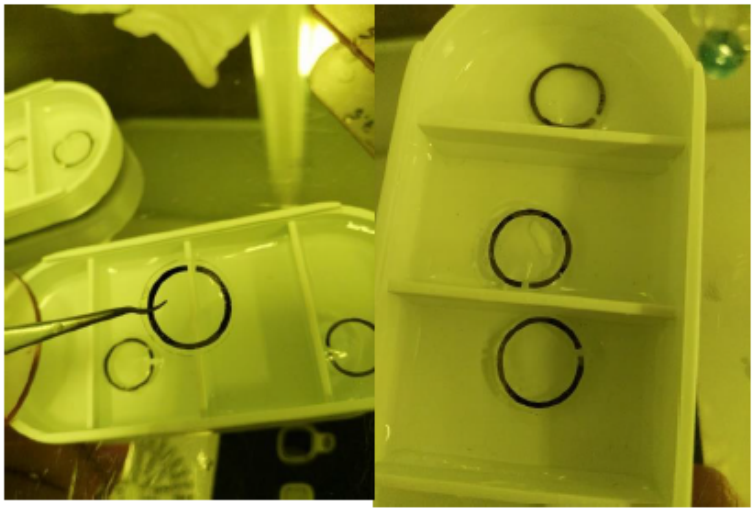

(a)

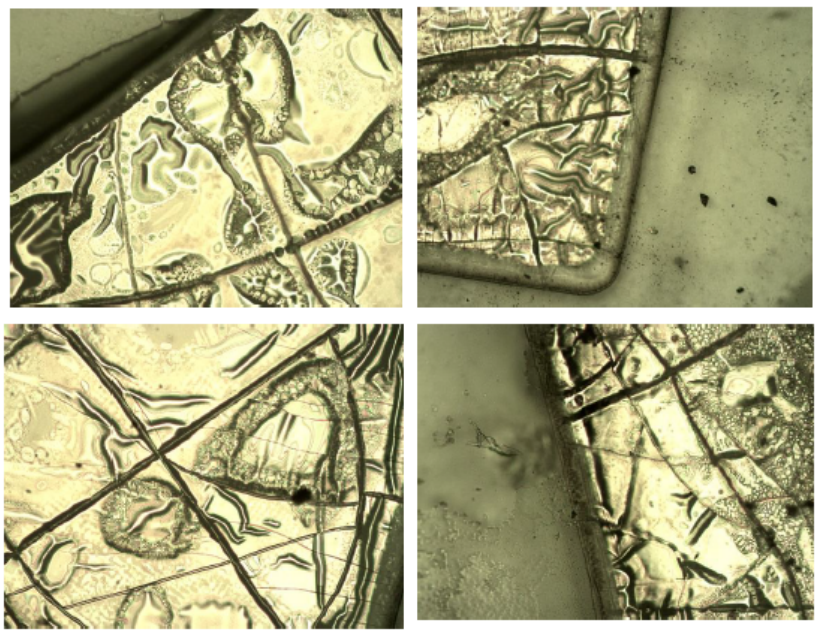

(b)

Figure 2.16. (a) The laser cut SRR embedded in PDMS structures stored in DI water. (b) Optical microscopy images show the cracked surface that was left from sputtering.

The wafer is then left for 2 minutes in 1:1:20 hydrogen fluoride (HF), hydrogen peroxide (H_2O_2), DI water, Ti etchant solution. Afterwards, the wafer is coated and cured with 50 µm PDMS again after O_2 plasma treatment, so that metal structures

will be completely embedded in PDMS.

Template for laser cutting was shaped using boundary drawings, and PDMS was cut with carbon dioxide (CO_2) laser. The sacrificial AZ layer was removed in acetone. The laser cut SRR embedded in PDMS structures were removed via lift-off in acetone after waiting around 5 min. They were stored in DI water(Figure 2.16(a)).

Optical microscopy images show the cracked surface that was left from sputtering. Figure 2.16(b) shows Ti deposited surface, and its optical microscopy images after etching. Ti etchant clearly moved through the cracks to etch the resonator structure. Pressure settings of the deposition chamber were changed to see the crack response. Crack density decreases when pressure decreases. However, since this is not a permanent solution for the problem, the substrate material is determined to be changed.

In this chapter, SRR designed for glaucoma detection in the previous work [2, 45] was further analyzed in terms of metal thickness and permeability with simulations using FDTD method. As a result, it is concluded that decrease in the thickness of the metal layer and increase in permeability decreased Q of the resonator, thus the performance of the system due to the increase of the RF sheet resistance.

Mechanical FEM simulations which are performed for the contact lens (CL) placed on the fibrous layer of the anterior part of the eye have been performed to analyze the displacements of the CL caused by the IOP level. As a result, 1 mmHg change in IOP corresponds to 4 µm change in the ROC is concluded. Moreover, the results of the simulations indicate that thickness variation within 100 µm to 100 µm range do not have significant effect on the deformation of CLs. Moreover, mechanical FEM simulations for bending processes of the resonators to be embedded in CL have been performed to analyze the feasibility of the fabrications.

In Section 2.3, fabrication of SRR-based sensor on PDMS substrate is given. The resonance behavior of the produced sensors could not be measured and possible reasons are as follows:

- The proper coating of the metal layers on the PDMS substrate could not be achieved due to the cracked surface that might effect the resonance characteristics of the sensor.
- 280 nm thick Ti layer was obtained after sputtering process. As given in Chapter 2.1.1.1, the Q factor could be very low with 280 nm thick Ti layer as the bulk resistivity of Ti is higher than that of Au.
- In order to measure the resonance behavior, the metal thickness was tried to be increased with electroplating to increase the Q. However, electroplating could not be achieved as the resistance of the seed layer was increased due to the cracked surface.

Since the metal coating on the PDMS substrate was challenging, it was decided to change the substrate material to PI. Furthermore, it has been concluded that a simple SRR is not suitable for glaucoma monitoring application, since the use of SRR around the eye tissues can only be achieved by thick dielectric layer isolation because the quality factor decreases dramatically as the conductivity of the environment approaches the conductivity of the eye tissues.

3. DESIGN OF TUNABLE ANTENNAS

In this chapter designs and the simulations of the folded dipole and spiral dipole antennas are given which aim to measure the resonant behavior of the resonator sensors. The motivation in designing folded-dipole and spiral-dipole antennas is to use an antenna which radiates in the first mode having similar frequency with the sensor so that resonance behavior of the resonator sensor can be obtained with high Q factor. Moreover, folded dipole antennas are also characterized in Section 3.3.

3.1. Theoretical Modeling

The first modes of the folded dipole and spiral-dipole antennas are calculated by the basic rule given in Equation 2.1. All capacitance and inductance values affecting the frequency of the first mode of the antennas calculated separately.

To calculate the first mode of the antennas, the distributed capacitance (C_{dis}) between two adjacent coils of a spiral is calculated by the formula [57]:

$$C_{dis} = \int_0^{2\pi R_a} \frac{\varepsilon_{r(eff)}}{\pi} \ln\left(1 + \frac{2w_a}{s_a}\right) dl_a \tag{3.1a}$$

where l_a, w_a and s_a are the length, width of coil and the gap between two adjacent coils. Also, R_a is defined as the average radius of two adjacent coils. It is stated in [58] that the distributed capacitance of a spiral with N turns is equal to the capacitance between two annular rings and independent of the number of turns (N). Then, C_{dis} of spiral-dipole antenna ($N > 1$) can be calculated by using the formula given as:

$$C_{dis} = 2R_{avg}\varepsilon_{r(eff)} \ln\left(1 + \frac{2w_a}{s_a}\right) \tag{3.1b}$$

where R_{avg} is the average radius of the coil. Gap capacitance (C_{gap}) of the folded dipole antenna ($N = 1$) is calculated from the formula given in Equation 2.2d where g is gap distance of the input port. Moreover, surface capacitance (C_{surf}) is also derived from the formula given in Equation 2.2e as follows:

$$C_{\text{surf}} = N\frac{2\varepsilon_{\text{r(eff)}}\,(h_a + w_a)}{\pi}\log\frac{4R_{\text{avg}}}{g_p} \tag{3.1c}$$

where h_a is the thickness of the metal coils. Therefore, total capacitance (C_{tot}) is calculated as:

$$C_{tot} = C_{\text{surf}} + C_{\text{port}} + C_{gap} + C_{dis} + C_{\text{tuning}} \tag{3.1d}$$

C_{tuning} is the tuning capacitance which is connected to adjust the first mode frequency of the antenna. Inductances (L) of the spiral-dipole antennas and folded dipole antennas are calculated as follows [59]:

$$L = \mu N^2 R_{\text{avg}}\left(\ln\frac{2.46}{p} + \frac{p^2}{5}\right) \tag{3.2}$$

where $p = w_a/s_a$ and μ is magnetic permeability of the metal.

3.2. Simulations

Simulations were performed using CST Microwave Studio software, illustrations of the simulated antennas are depicted in Figure 3.1 and design parameters of the antennas are given in Table 3.1. g is 2.5 mm for folded dipole antenna.

The first modes of the antennas are calculated as given in Section 3.1 and compared with simulated values. For calculations, $\varepsilon_{\text{r(eff)}}$ was selected as tuning parameter for 130 µm thick FR-4 without ground plane and it was determined as 2.1 to minimize the error for the operating frequency of the folded dipole antenna.

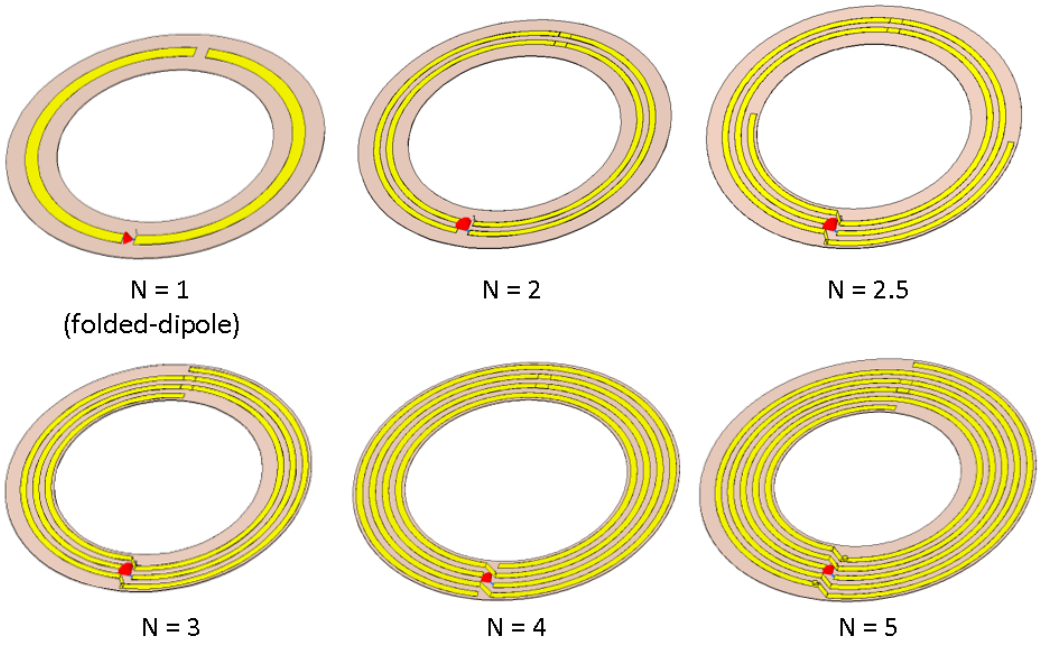

Figure 3.1. Illustrations of simulated antennas.

Table 3.1. Design parameters of simulated antennas.

Number of turns (N)	g_p (mm)	w_a (mm)	s_a (mm)	R_{avg} (mm)	h_a (µm)	$\varepsilon_{r(eff)}$
1	3	2	∞	21	35	2.1
2	3	1	1	21	35	2.1
2.5	3	1	1	21	35	2.1
3	3	1	1	21	35	2.1
4	3	1	1	21	35	2.1
5	3	1	1	21	35	2.1

Results of simulations are given in Appendix A. s_{11} spectra of the simulated antennas are given in Figure A.1 to Figure A.6 around their first modes. Given the simulation results, it can be said that as the tuning capacitance increases, the first mode shifts to the left with decreasing Q. Decrease in the Q due to the increased capacitance can be explained by the series connection of the capacitance to the antenna.

Comparison of calculated and simulated first modes of antennas are given in Table A.1 to Table A.6. As a result, the calculated first modes of the antennas are in good agreement with the simulations, the relative error is less than 5%.

3.3. Characterization of Antennas

It is decided to use folded dipole antennas due to their simple design and ease of fabrication to measure the resonance behavior of the CLSs. s_{11} spectra of folded dipole antennas fabricated by printed circuit method on 130 µm thick FR-4 substrates were measured by vector network analyzer VNA, (ZNLE6, Rohde-Schwarz, Munich, Germany). SMA connectors are soldered to the part left in the antennas. Figure 3.2 shows a photograph of an example fabricated antenna with soldered tuning capacitance (C_{tuning}) and SMA connector.

Figure 3.2. Photograph of an example antenna with C_{tuning} and SMA connector.

Measured s_{11} spectra of the folded dipole antenna with respect to varying values of the C_{tuning} are given in Figure 3.3. Moreover, measured first modes of the folded dipole antennas are compared with the calculated and simulated first modes of the folded dipole antenna which are given in Table A.1 and Table A.2. As a result, measured

first modes of the antennas are in good agreement with the calculated and simulated values.

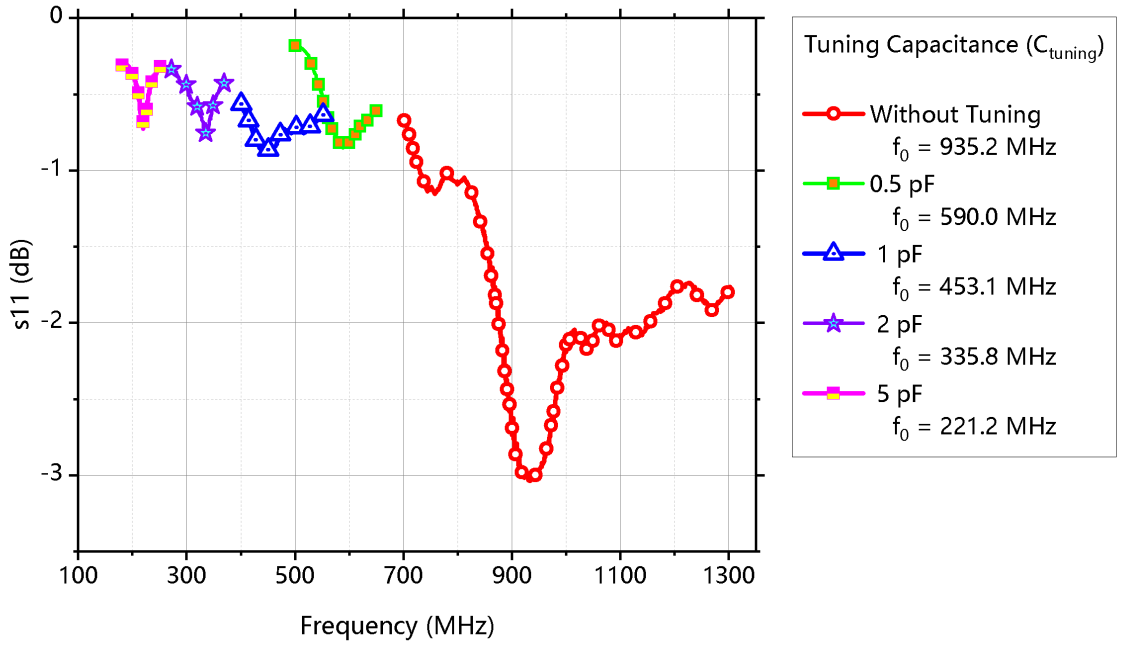

Figure 3.3. Measured s_{11} spectra of the folded dipole antenna with respect to varying values of the C_{tuning}.

Table 3.2. Comparison of the measured first modes of the folded dipole antennas with the calculated and simulated values.

Tuning Capacitance (C_{tuning}) (pF)	**Measured** $f_{0(a)}$ (MHz)	**%Error with calculated** $f_{0(a)}$	**%Error with simulated** $f_{0(a)}$
0	935.2	-5.24	-5.16
0.5	590	2.09	-0.17
1	453.1	0.93	-2.00
2	335.8	0.16	-2.61
5	221.2	0.65	-2.98

4. DESIGN AND MODELING OF BC-SRR BASED ANTENNA COUPLED SENSOR

In section 2.1.1.3, it was shown that a simple SRR is not suitable for glaucoma monitoring application as its Q decreases dramatically when the conductivity of the defined water layer closes to the conductivities of the eye tissues. Therefore, using the SRR around the eye tissues would only be possible with thick dielectric layer isolation, which is not suitable for this application because of mechanical constraints put by the application.

The decrease in the Q of the SRR with increasing conductivity is due to the decrease in the Q of the self-capacitance of the SRR since the dielectric layer of the capacitance is deteriorated by increased conductivity. Therefore, it is important to find a way to protect the dielectric layer of the resonator. A reasonable solution to this challenge is to trap dominant capacitance of the CLS between two conductive layers and use a substrate that would not absorb water. Therefore, BC-SRR based CLSs has been initiated with this idea.

4.1. Theoretical Modeling

The typical BC-SRR consists of two SRRs realized on the opposite sides of the dielectric substrate, with gaps facing in the opposite directions. [60]. Moreover, BC-SRR may also consist of more than two split rings, which is reported as design idea for band pass filter applications in [61]. The resonant frequency of the BC-SRR can be controlled by sizes or the geometries of the SRRs and the thicknesses and materials of the dielectric layers, and changing angular orientations.

The BC-SRR interacts with incoming electromagnetic wave as the SRR does. The incident time-varying magnetic field supports a circulating current on each split-rings and the gap on split-ring behaves like a capacitor and the metal ring as an

inductor. The resonant frequency of BC-SRR changes with the corneal curvature like a typical SRR because the resonant frequency of the resonator is determined with the geometry of the structure. However, in BC-SRR, charge distribution between top and bottom metal rings will create a mutual capacitance and this capacitance will shift the resonance frequency of the BC-SRR to the lower frequencies.

Resonant frequency of the BC-SRR can be expressed by the formula given in Equation 2.1. Here, L is the the average of the inductances of both rings and can be calculated by the formula given in Equation 2.2b. Here C is the total capacitance of this circuit is the series connection of the capacitances of both BC-SRR halves, that is C/2 [62]. The capacitance between the rings can be calculated by the parallel-plate capacitor formula given by:

$$C = \frac{\varepsilon_r \varepsilon_0 A}{d} \tag{4.1}$$

where ε_{r} is the relative permittivity of the substrate between SRRs, ε_0 is free space permittivity, A is the area of the half of the SRR and d is the distance between the rings.

BC-SRR also has the $\mathrm{C_{gap}}$ and $\mathrm{C_{surf}}$ like SRR; however, mutual capacitance between the rings is the dominant capacitance over the frequency response for this application as the thickness of the dielectric layer between SRRs is designed to be as thin as possible to ensure the flexibility of the sensor. Any change of the distance between metallic rings or surface area of the rings changes the resonance behaviour of the system. Similarly, a BC-SRR resonator embedded in a soft contact lens responds to the deformation due to change in the IOP with a shift in the resonant frequency. Moreover, the mutual capacitance can be well tuned to achieve the desired resonance frequency. For an application of IOP measurement, lower frequencies to decrease the loss in the soft tissues [29] are preferred.

4.2. Simulations

Firstly, the simulations were performed for the BC-SRR with CST Microwave Studio software to analyze the E and H fields at the resonance. For the simulations, gap distances of SRRs are 1 mm, inner radii are 4.5 mm, widths are 1.5 mm, and the distance between SRRs is 200 µm. Substrate is defined as PDMS and total thickness of the substrate is 500 µm. BC-SRR is placed in the middle of the substrate. Conductive layers are defined as gold. PDMS and gold materials are imported from the material library of the CST Microwave Studio for these simulations.

Illustration of the simulated folded dipole antenna coupled BC-SRR based sensor is given in Figure 4.1. The tuning of the folded dipole antenna is provided by the extra conductive layers around the dipole arms, which increases the total capacitance slightly.

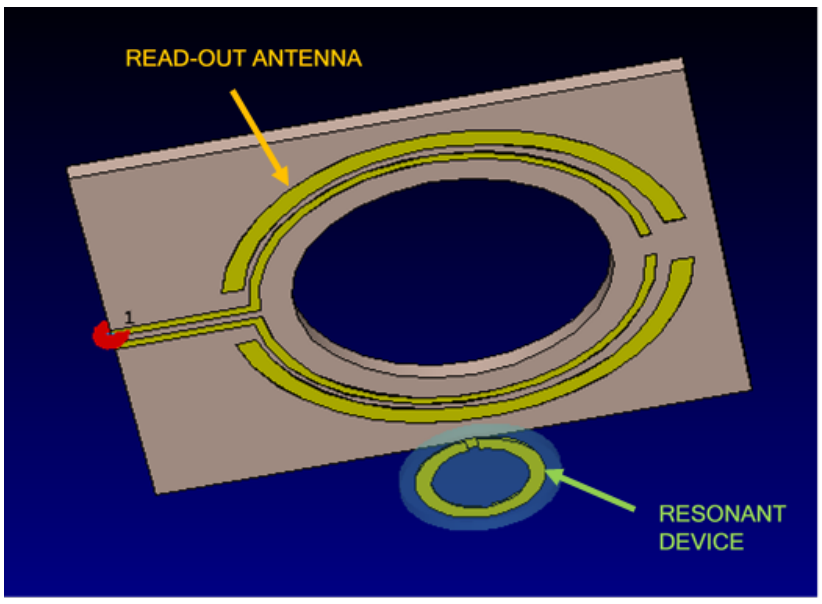

Figure 4.1. Illustration of the simulated folded dipole antenna coupled BC-SRR embedded in PDMS.

Results of the simulated s_{11} spectra with respect to varying additional distances (mm) of the BC-SRR to the antenna is given in Figure 4.2. Initial distance of BC-SRR to the antenna is defined as 30 mm. Additional distances are defined as distance in the

results. As can be seen from the results, resonant frequency of the BC-SRR did not shift with changing distance values. Moreover, the first mode of the antenna is around 900 MHz and resonant frequency of BC-SRR is at 921.2 MHz. Resonant frequency of the defined BC-SRR is calculated as 966.0 MHz from the formulas given in Section 4.1. The difference between calculated and simulated values caused by the 500 µm thick PDMS substrate that also covers the top and the bottom of the BC-SRR, which increases C_{surf}, thus decreases the resonant frequency.

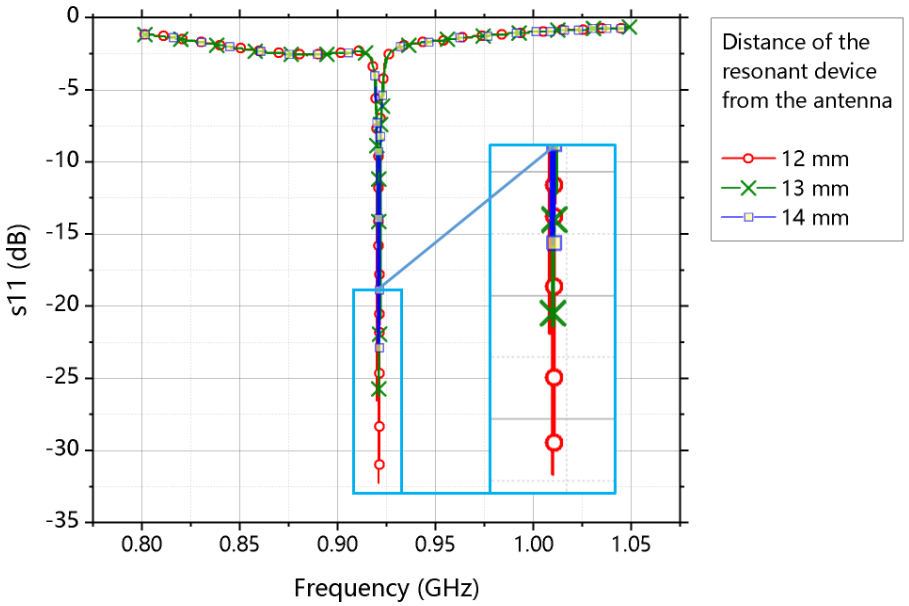

Figure 4.2. The simulated s_{11} spectra with respect to varying additional distances (mm) of the BC-SRR to the antenna.

Simulated electric field intensity (E) and magnetic field intensity (H) lines on xz plane of the folded dipole antenna coupled BC-SRR at resonance are given in Figure 4.3(a) and Figure 4.4(a), respectively. Figure 4.3(b) shows the simulated E field in z direction in between the rings of the BC-SRR of the folded dipole antenna coupled BC-SRR at resonance, which shows the opposite direction of E in the middle of the BC-SRR. Therefore series connection of the capacitances of both BC-SRR halves explained in Section 4.1 can be understood better with these results. Moreover, Figure 4.4(b) shows the simulated H in z direction on xz plane, it can be said that the magnetic field is focused on the center of the BC-SRR while exciting it with folded dipole antenna.

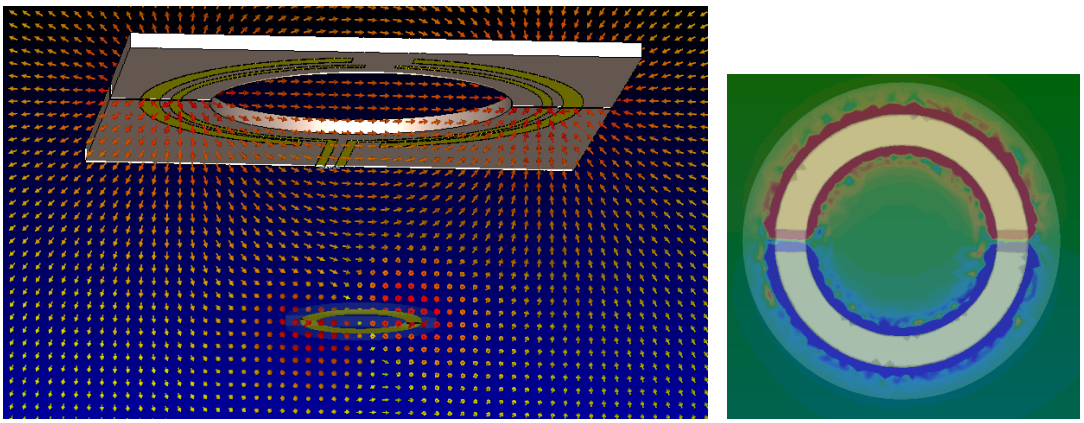

(a) (b)

Figure 4.3. (a) Simulated E field lines on xz plane and (b) simulated E field in z direction in between the rings of the BC-SRR of the folded dipole antenna coupled BC-SRR at resonance.

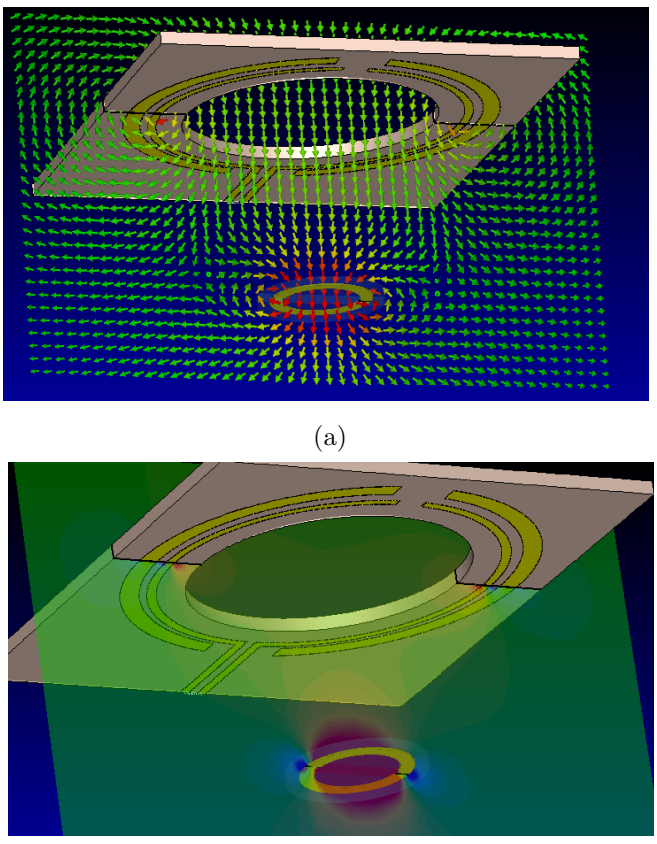

(a)

(b)

Figure 4.4. (a) Simulated H field lines on xz plane and (b) simulated H field in z direction on xz plane of the folded dipole antenna coupled BC-SRR at resonance.

4.2.1. BC-SRR Embedded in Polyimide Thickness Analysis Simulations

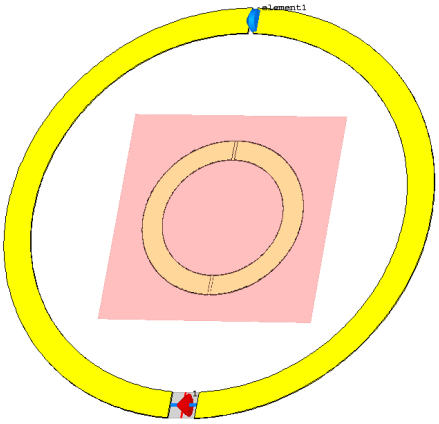

(a)

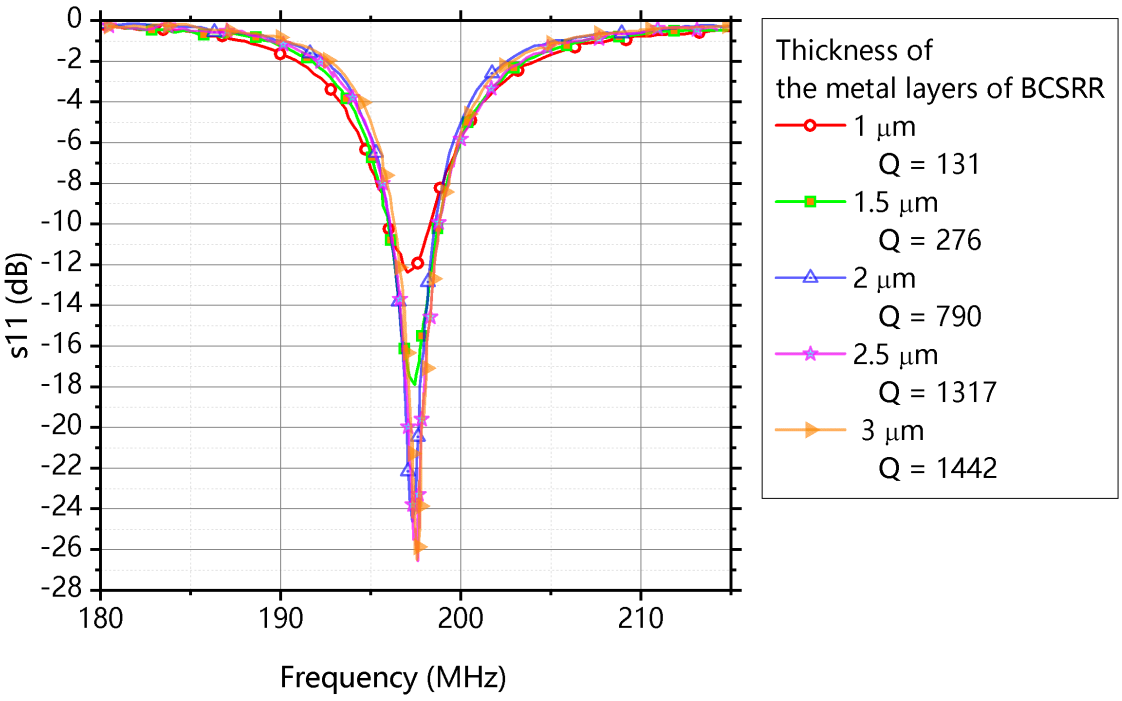

(b)

Figure 4.5. (a) Illustration of the simulated folded dipole antenna and BC-SRR embedded in the PI substrate. (b) Simulated s_{11} spectra with respect to varying values of thicknesses of the metal layers of BC-SRR.

The simulations were performed for the antenna coupled BC-SRR embedded in the PI substrate depicted in Figure 4.5(a) with respect to varying values of thicknesses of the metal layers of BC-SRR. For the simulations, gap distances of SRRs are 200 μm,

inner radii are 4.5 mm, widths are 1.5 mm, and the distance between rings is 10 µm. BC-SRR was placed in the middle of the PI substrate which has a thickness of 100 µm. Antenna is tuned with the tuning capacitance (C_{tuning}) of 7.4 pF and substrate of the antenna is excluded from the simulations for the simplicity of simulations.

To define thicknesses of metals, sheet resistance values of 1 µm, 1.5 µm, 2 µm, 2.5 µm, and 3 µm thick gold for a given frequency range are calculated as given in Section 2.1.1.1 and imported to CST Microwave Studio software as tabulated surface resistance values. s_{11} spectra with respect to varying values of thicknesses of the metal layers of BC-SRR is given in Figure 4.5(b).

As can be seen in the simulation results, decrease in the thickness of the metal layer, decreases Q of the resonator due to the increase in the RF sheet resistance. As a result, using very thin metals for the resonators reduces the performance of the sensor system as the Q decreases with increasing resistance, which in turn lowers the resolution of the sensor.

Specifically for this example, for BC-SRR having a resonance frequency of around 200 MHz, the thickness of the conductive layers should be greater than 2.5 µm as the Q value increases as the thickness increases to 2.5 µm and converges thereafter as given in Figure 4.5(b).

4.2.2. BC-SRR Embedded in Polyimide Loss Tangent Simulations

The effect of loss tangent on the resonance behavior of the BC-SRR was also analyzed with simulations using CST Microwave Studio. Dielectric properties of the PI are given in Figure 2.2. With respect to this figure relative permittivity of the substrate was chosen as 3.4 and loss tangent was changed parametrically to observe its effect. The simulations were performed for the antenna coupled BC-SRR embedded in the PI substrate depicted in Figure 4.5(a) with respect to varying values of tangent loss of PI substrate.

For the simulations, gap distances of SRRs are 200 µm, inner radii are 4.5 mm, widths are 1.5 mm and the distance between rings is 12.5 µm. BC-SRR placed in the middle of the PI substrate which has the thickness of 100 µm. Antenna is tuned with the tuning capacitance (C_{tuning}) of 7.3 pF and substrate of the antenna is excluded from the simulations for the simplicity of simulations.

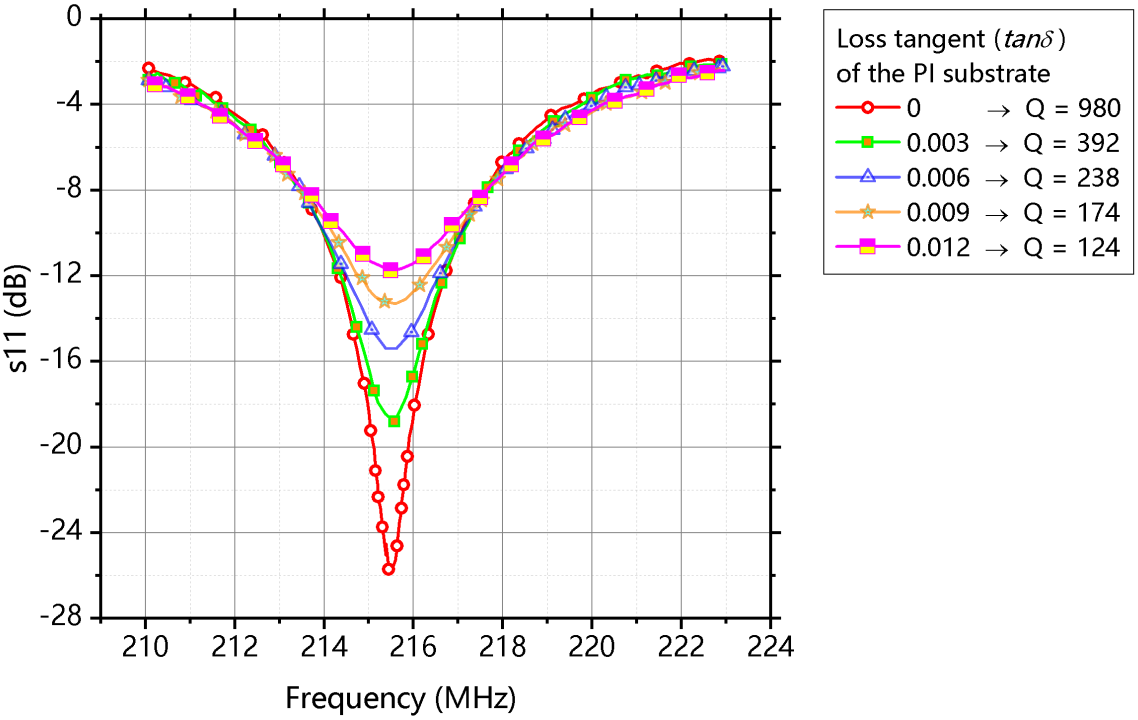

Figure 4.6. The simulations were performed for the antenna coupled BC-SRR embedded in the PI substrate with respect to varying values of tangent loss of the substrate.

As given in Figure 4.6, increasing the loss tangent (tanδ) of the PI substrate decreases the Q of the antenna coupled resonator system. As a result, using substrates with high dielectric loss for the fabrication of the resonators reduces the performance of the sensor system as the Q decreases with increasing tanδ, which in turn lowers the resolution of the sensor.

4.2.3. BC-SRR based sensor placed on Eye-globe Material Simulations

For the BC-SRR based sensor placed on eye-globe material simulations, Eye-globe material in the CST Microwave library is used to simulate the lossy environment of the eye. Firstly, the simulations were performed for with waveguide ports for measuring s_{21} spectra, which will normally be implemented by antennas by measuring s_{11}.

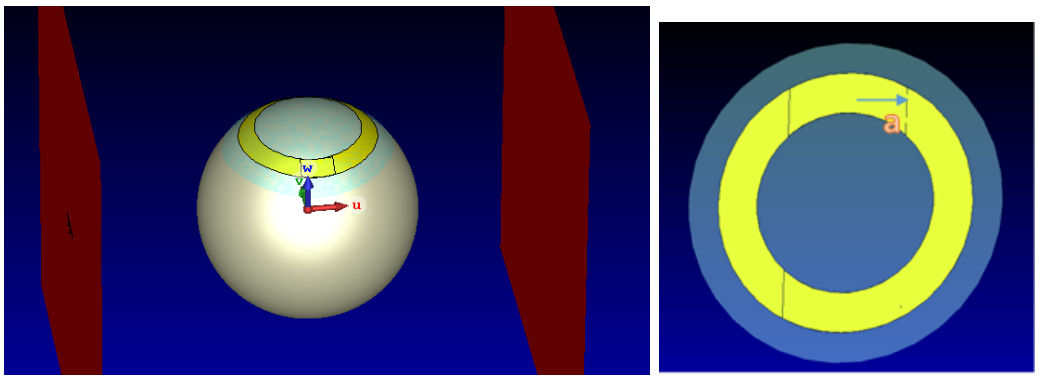

(a) (b)

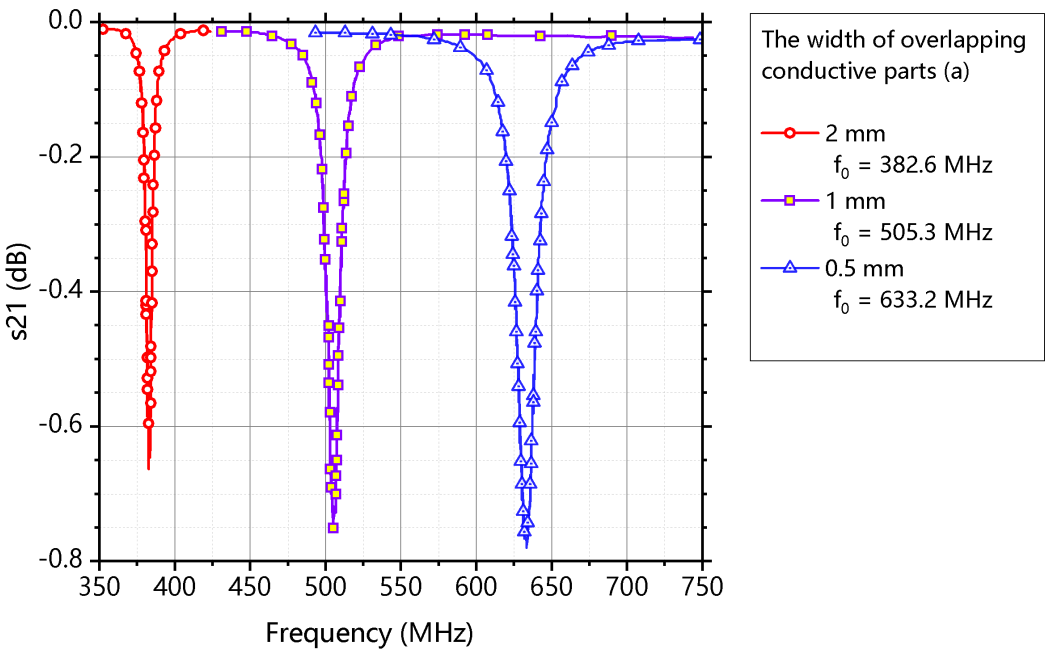

(c)

Figure 4.7. (a) Illustration of the simulated sensor bent on eye-globe material, (b) Detailed illustration of the planar sensor showing defined a and (c) Simulated s_{21} spectra for varying a (mm).

For the first simulations, inner radii of the BC-SRR are defined as 4.5 mm, widths are 1.5 mm, and the distance between rings is 12.5 µm. BC-SRR is placed in the middle of the PDMS substrate which has the thickness of 100 µm. BC-SRR sensor is bent on the defined eye-globe material with a radius of 8.5 mm.

As can be seen from Figure 4.7(b), the gap of the rings are changed by changing a, defined as the half of the width of overlapping conductive parts (mm) of the BC-SRR and the effect of the gap distance is analyzed. Simulation results given in Figure 4.7(c) show that as a increases, resonant frequency of the BC-SRR sensor bent on eye-globe material decreases due to the increasing capacitance between the rings.

The effect of the change in the radius of the eye-globe is also analyzed by simulations. BC-SRR sensor with a =1 mm is bent on the defined eye-globe material with a radius of r (mm) as given in Figure 4.7(a) and r is changed parametrically to see its effect on the resonance behavior.

Simulated s_{21} spectra with respect to varying values of r of the eye-globe for r changing from 8.1 mm to 8.2 mm and from 8.5 mm to 8.58 mm are given in Figure 4.8(a) and Figure 4.8(b), respectively. Given the simulation results, for the simulated model of BC-SRR, an average shift in the resonant frequency is calculated for r ranging from 8.1 mm to 8.2 mm as 32 MHz/mm and for r ranging from 8.1 mm to 8.2 mm as 36.2 MHz/mm. Therefore it can be said that the shift in the resonant frequency for a unit change in the ROC decreases as the initial ROC increases.

Furthermore, folded dipole antenna coupling effect to the BC-SRR based CLS placed on the eye-globe material on the s_{11} behavior is also analyzed with simulations using CST Microwave Studio software. Illustration of the folded dipole antenna and the simulated sensor is given in Figure 4.9(a).

In this simulation, capacitance C (pF) is added to the gap on the antenna realized on 1.5 mm FR4 substrate as tuning capacitance C_{tuning}. For the simulations, gap distances of SRRs are 1 mm, inner radii are 4.5 mm, widths are 1.5 mm and the distance

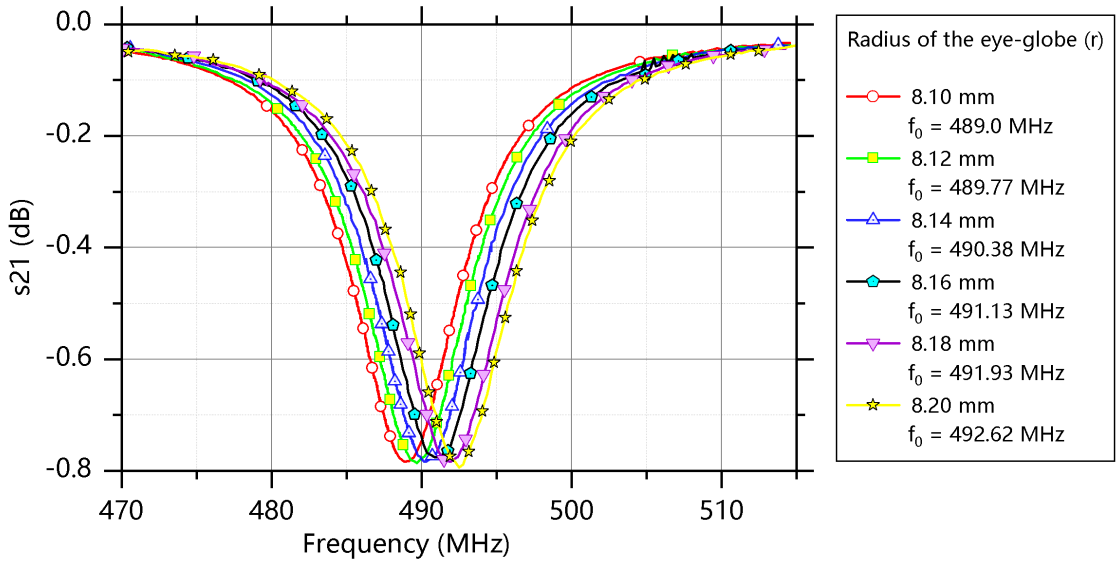

(a)

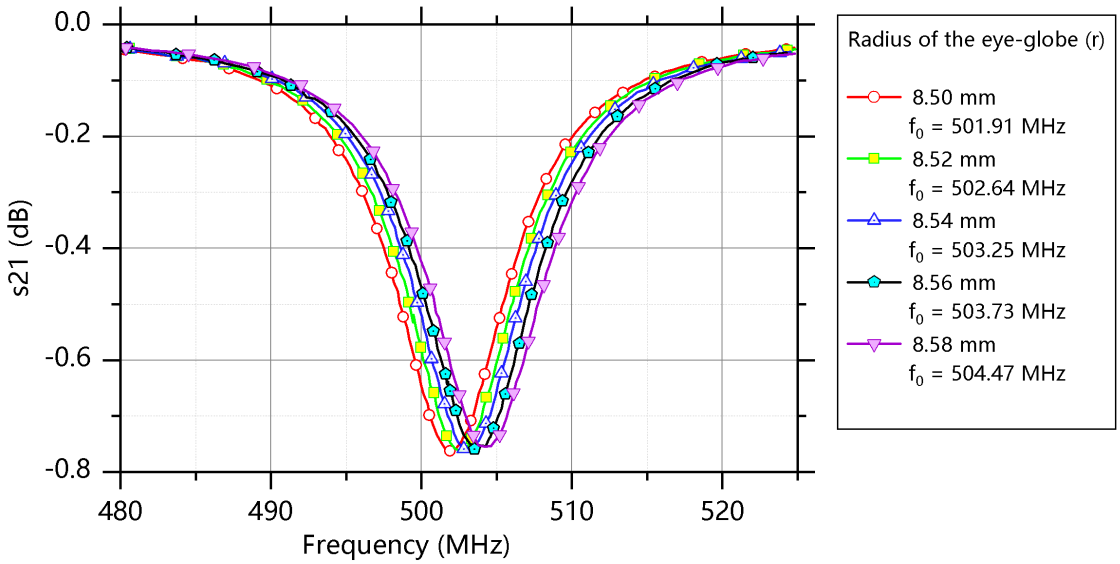

(b)

Figure 4.8. Simulated s_{21} spectra with respect to varying values of r of the eye-globe where (a) r is changing from 8.1 mm to 8.2 mm and (b) r is changing from 8.5 mm to 8.58 mm.

between rings is 12.5 µm. BC-SRR placed in the middle of the PDMS substrate which has the thickness of 100 µm.

The results of the tuning of the folded dipole antenna is given in Figure 4.9(b). With capacitive tuning the frequency of the first radiating mode of the antenna is redshifted to the resonant frequency of the BC-SRR on the eye globe. Therefore, the antenna and the resonator became part of resonant circuits tuned to resonate at the same frequency,which improves the Q of the system.

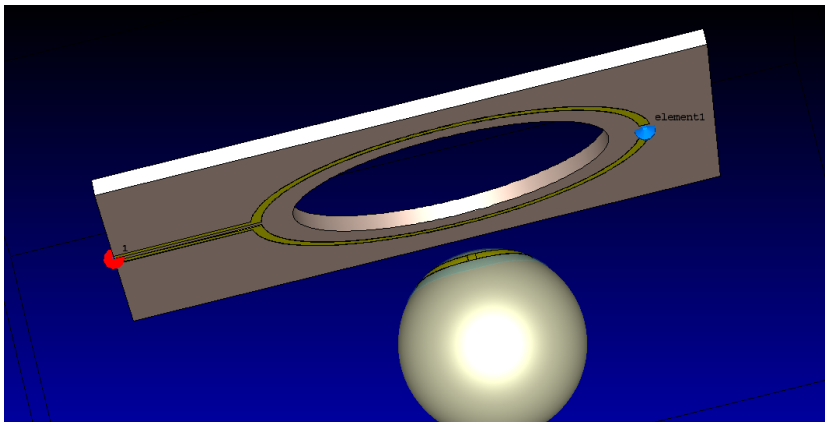

(a)

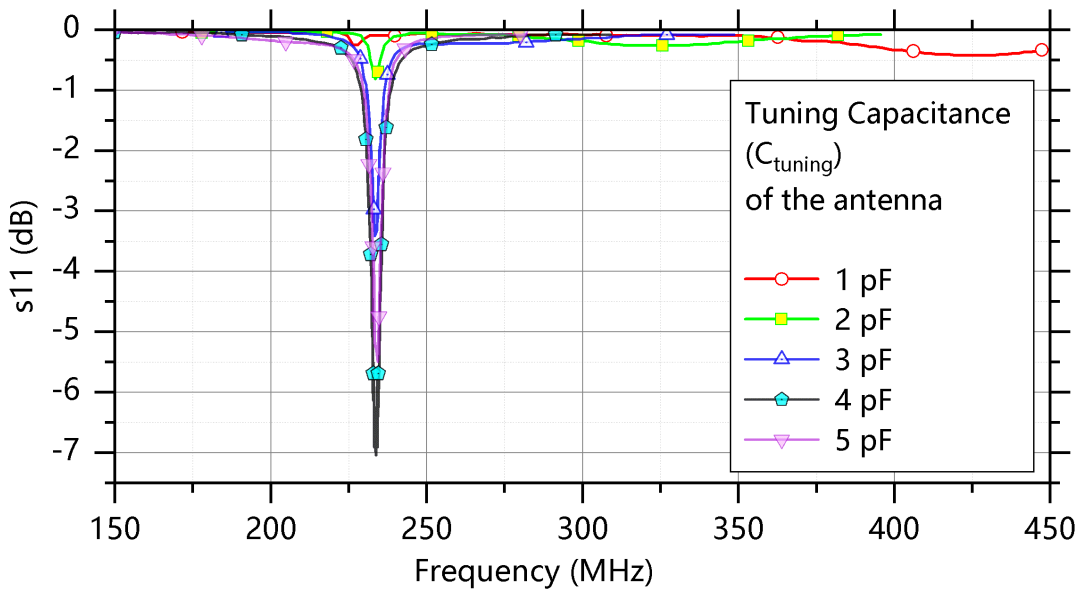

(b)

Figure 4.9. (a) Illustration of the simulated folded dipole antenna with the BC-SRR based CLS placed on the eye-globe material. (b) Simulated s_{11} behavior of the system with respect to varying values of C_{tuning} (pF).

5. FABRICATION AND CHARACTERIZATION OF SENSORS

In this chapter fabrication of the BC-SRR based CLS is explained. Furthermore, resonance behaviors of the CLSs are measured with respect to changing IOP values of the designed mechanical eye model with the specialized test setup and results are analyzed.

5.1. Fabrication of Sensors Embedded in Polyimide

Fabrication processes were done in the clean room located in Boğaziçi University, Kandilli Campus. Spin coating, lithography, etching and sputtering were used in various steps of fabrication. The fabrication steps of the resonator embedded PI explained as follows:

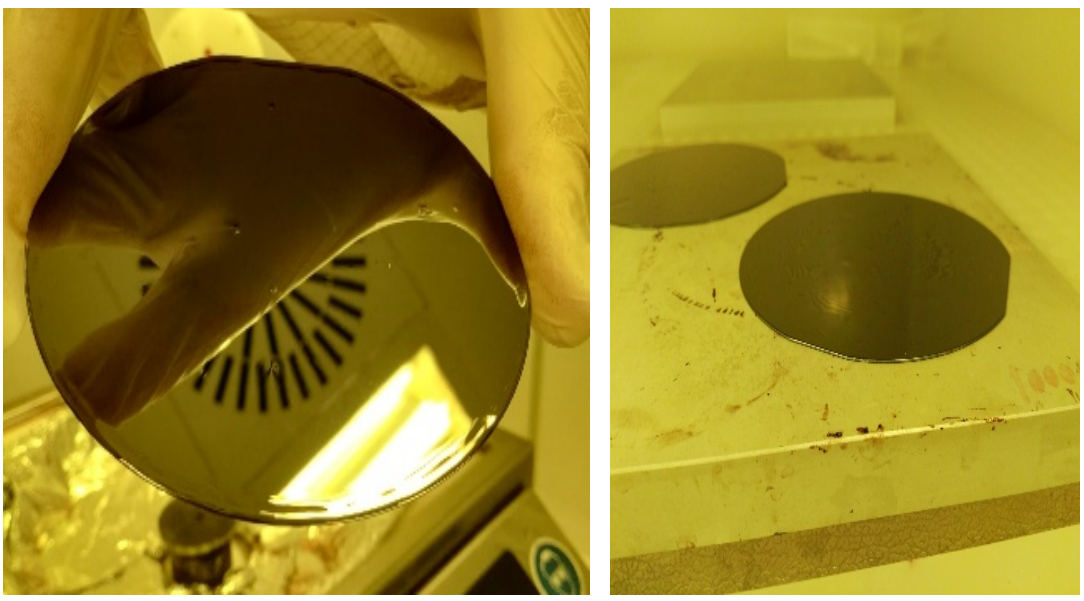

(a) (b)

Figure 5.1. (a) Photograph of the PI spin coated wafer. (b) Soft baking on hot plate.

After cleaning of the wafer using piranha solution and rinsing, the wafer is dried using Nitrogen (N_2) gun and hot plate at 200 °C for 20 min. Oxygen (O_2) plasma is

applied onto the wafer at 200 mTorr, 70 W for 10 min to clean carbon contaminants. Then, the first layer of the PI2611 is spin coated (500 rpm for 15 s and 2000 rpm for 45 s) on the wafer. For soft-baking, the wafer is placed on hot plate that is set to 40 °C and the temperature is gradually increased to 170 °C with a ramp-rate of 3 °C s^{-1}. The same spin and soft bake procedures are done for additional 2 10 µm PI layers [63].

Then the metal layers are sputtered on the wafer (chromium (Cr) 5 nm and gold (Au) 5 nm).O_2 plasma is applied at 200 mTorr and 70 W for 3 min before sputtering to improve adhesion. For the lithography, AZ-5214 is used as negative photo resist (PR), and only baked at 110 °C for 50 s [53]. It is developed in its developer solution and rinsed with DI water. After lithography, Au-Cr layers are etched with their selective etchants.

(a) (b)

Figure 5.2. (a) Soft baking of the last spin coated PI layer. (b) Photograph of the hard-baked wafer.

After patterning the resonators on the PI substrate, adhesive is applied on metal (VM 651 0.1%) before coating and the same PI spin coating and soft bake procedures applied for the top PI layer. To release the fabricated resonators embedded PI hard bake is done in oven, the temperature is gradually increased to 350 °C with a ramp-rate of 4 °C min^{-1} from the room temperature.

The fabrication step outputs of the resonator embedded PI are given in Figure 5.1 and Figure 5.2. During the fabrication, blister formations occured on PI at the soft baking steps which can also be seen in Figure 5.2(a). While doing the hard baking, the quality of the cured polymer deteriorated considerably (Figure 5.2(b)), so that it could not be used for CLSs.

Since the production process was insufficient, the production of the sensors in the clean room was abandoned and commercial solutions were applied. The sensor is designed to have resonant frequency less than 500 MHz; because, as given in [64], the conductivity values of the body tissues increase rapidly above 500 MHz, which increases the loss of electromagnetic energy due to the absorption. When the fabricated sensors arrived, they are laser cut using CO_2 laser (Versa Laser Engraver 30W). A photograph of the laser cut sensor is given in Figure 5.3.

Figure 5.3. Photograph of the laser machined sensor.

5.2. PDMS Eye Model

For in vitro testing of the designed BC-SRR based sensors, it is decided to use a mechanical eye model. Therefore, mechanical eye is modeled in SolidWorks software. Illustration of a modeled eye can be seen in Figure 5.4(a). Eye model is designed to be fabricated from the PDMS material and filled with saline water. The test setup will be used to pump additional saline into mechanical eye model to change pressure and

ROC of the cornea of the model.

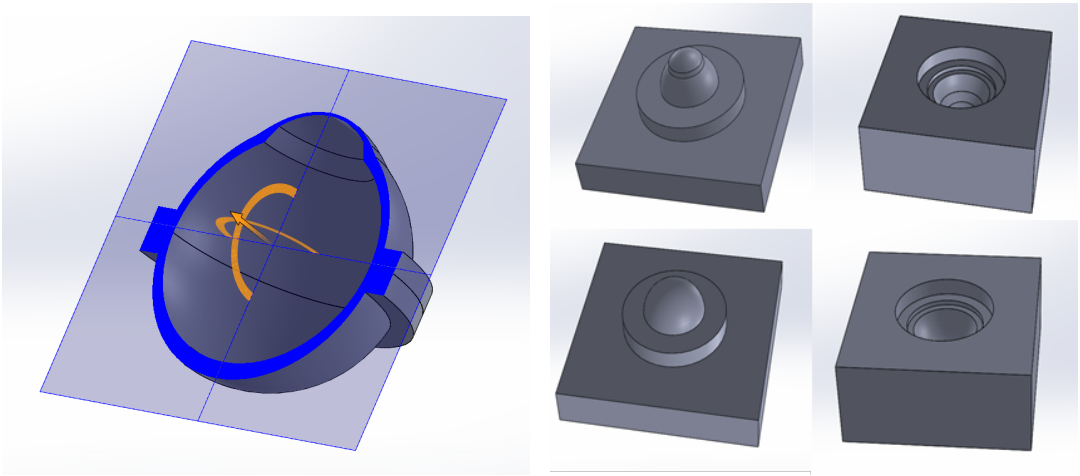

(a) (b)

Figure 5.4. (a) Illustration of the modeled eye. (b) Designed molds for the fabrication of the mechanical eye model.

Figure 5.4(b) shows the designed molds modeled using SolidWorks software based on the designed eye model. Designed molds were 3D printed from VeroClear material in the clean room and they were baked over night at 85 °C for glass transition [65].

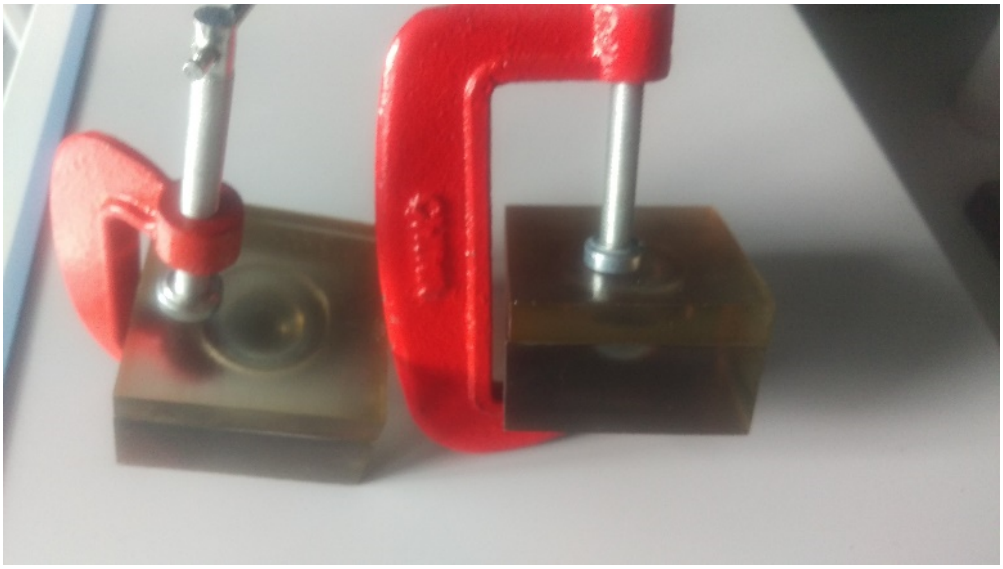

Figure 5.5. Photograph of the 3D printed VeroClear molds glass transited for the fabrication of the mechanical eye.

PDMS material is prepared as explained in [66], placed in the concave mold and degassed in vacuum for 30 min. Before PDMS, silicone oil is applied to the molds as a thin layer to strip the PDMS easily after curing. Convex molds are closed on degassed PDMS and pressed (Figure 5.5). PDMS pre-polymer is cured at room temperature for 24 h to fabricate mechanical PDMS eye. A photograph of the mechanical eye models fabricated from PDMS is given in Figure 5.6

Figure 5.6. Photograph of the fabricated mechanical eyes from PDMS.

5.3. Embedding in Contact Lens Material

In order to embed planar sensors in the CL, it was necessary to bend them first to change the ROC of the fabricated sensors. So it is decided to bend the sensors by molding. Therefore, two-part hemisphere molds (ROC is 8.6 mm) are Computer Numerical Control (CNC) machined from steel. Laser cut sensors are placed in the middle of the mold pair and pressed carefully. Mold pair is heated in the oven to 200 °C for 7 min to bend the sensors. Figure 5.7(a) shows a photograph of the closed mold pair and Figure 5.7(b) shows a photograph of the spherically deformed sensor bent by molding.

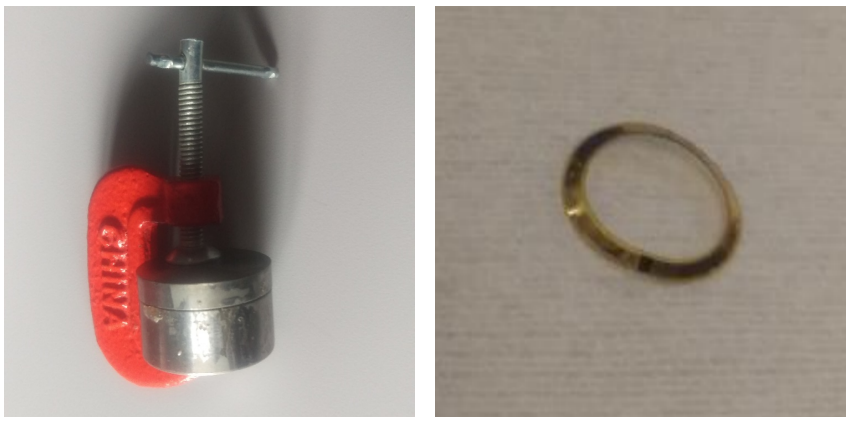

(a) (b)

Figure 5.7. (a) Photograph of the closed mold pair. (b) Photograph of the spherically deformed sensor bent by molding.

The sensors are embedded in CL in Anadolu Tıp A.Ş. (Sivas). The CL material they are using is polyurethane-acrylate (PUA), which is biocompatible, ultraviolet (UV) curable, hydrophobic material. The sensors are placed in the glass molds which is designed to produce contact lens with a ROC of 8.6 mm and uncured PUA is added between the molds. Each side of the CLS is cured with photo-polymerization device. A photograph of the resulting CLS is given in Figure 5.8.

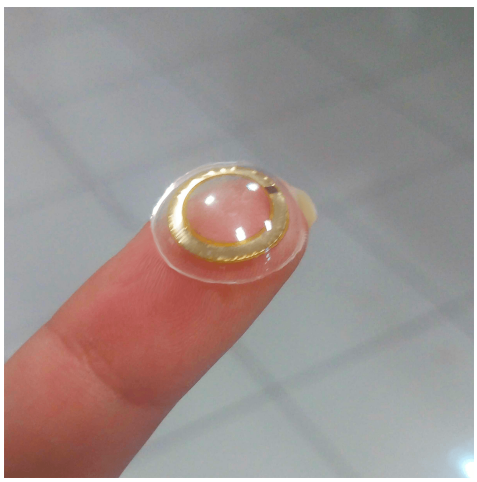

Figure 5.8. Photograph of the spherically deformed sensor embedded in CL.

5.4. Measurement Setup

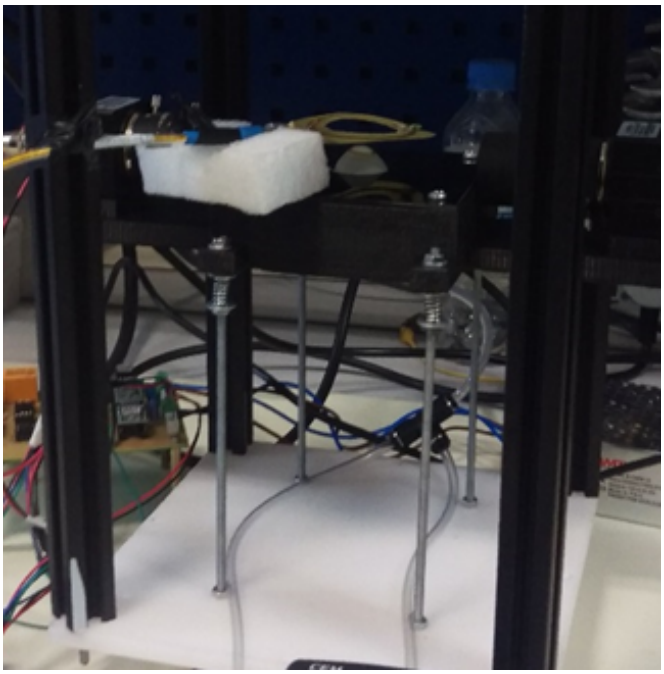

(a)

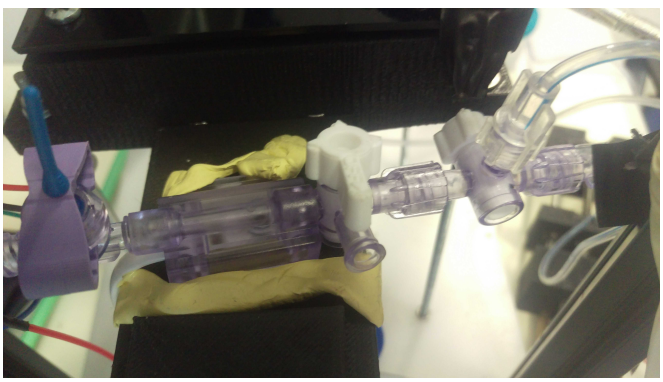

(b)

Figure 5.9. Photograph of the PDMS eye model integrated test setup.
(b) Photograph of the pressure sensor.

The test setup is provided by Glakolens A.Ş. for the measurements of the fabricated sensors. Fabricated PDMS eyes are connected to the test setup, which can be seen in Figure 5.9(a). The system includes a bottle of the isotonic saline solution with a holder to control its elevation, a commercial intravascular blood pressure sensor (NPC-120T) and a graphical user interface (GUI).

Working principle of the test setup is as follows: PDMS eye is filled with saline water and connected to the bottle of isotonic saline solution with silicone pipe. The elevation of the saline bottle is changed to change the pressure level of the connected PDMS eye. Pressure sensor is placed on the same elevation with the PDMS eye and pressure level is measured and read from the GUI.

5.5. Results

The response of the change in the pressure of the PDMS eye (IOP) on the resonant frequency of the folded dipole antenna coupled CLS is analyzed. s_{11} spectra were measured with VNA (ZNLE6, Rohde-Schwarz, Munich, Germany). Antenna is tuned to the resonant frequency of the CLS when the pressure is 0 mmHg and the impedance at the nominal resonant frequency is matched to the 50 Ω to increase the Q of the system. A photograph of the antenna and the CL placed on the PDMS eye can be seen in Figure 5.10.

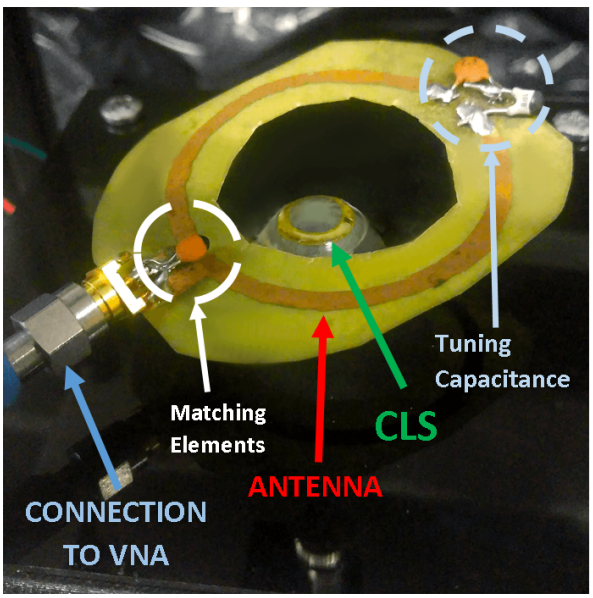

Figure 5.10. Photograph of the antenna and the CLS placed on the PDMS eye.

The pressure level is changed from 10 mmHg to 50 mmHg by changing the elevation of the saline bottle, and measurements are taken with an accuracy of ±1 mmHg in every 5 mmHg change. Experiments are repeated 19 times and measured s_{11} spectra

in those experiments showing the resonant frequencies with respect to varying values of IOP levels are given in Appendix B from Figure B.1 to Figure B.9.

The ensemble of the experiments showing the mean values of the measured resonant frequencies with standard deviation error bars is given in Figure 5.11. Given the results, the slope of the fitted curve shows that the change in the resonant frequency corresponding to a unit change in pressure is −31.09 kHz/mmHg.

Moreover, Q factors of the measured resonant frequencies are given in Appendix B from Figure B.1 to Figure B.19. Average of the measured Q is calculated as 7349 and average of the measured f_0 is calculated as 451.347 MHz. Therefore, given the simulation results, bandwidth is calculated as 61.42 kHz, which corresponds to the 3 dB resolution of 1.98 mmHg for the CLS on PDMS eye.

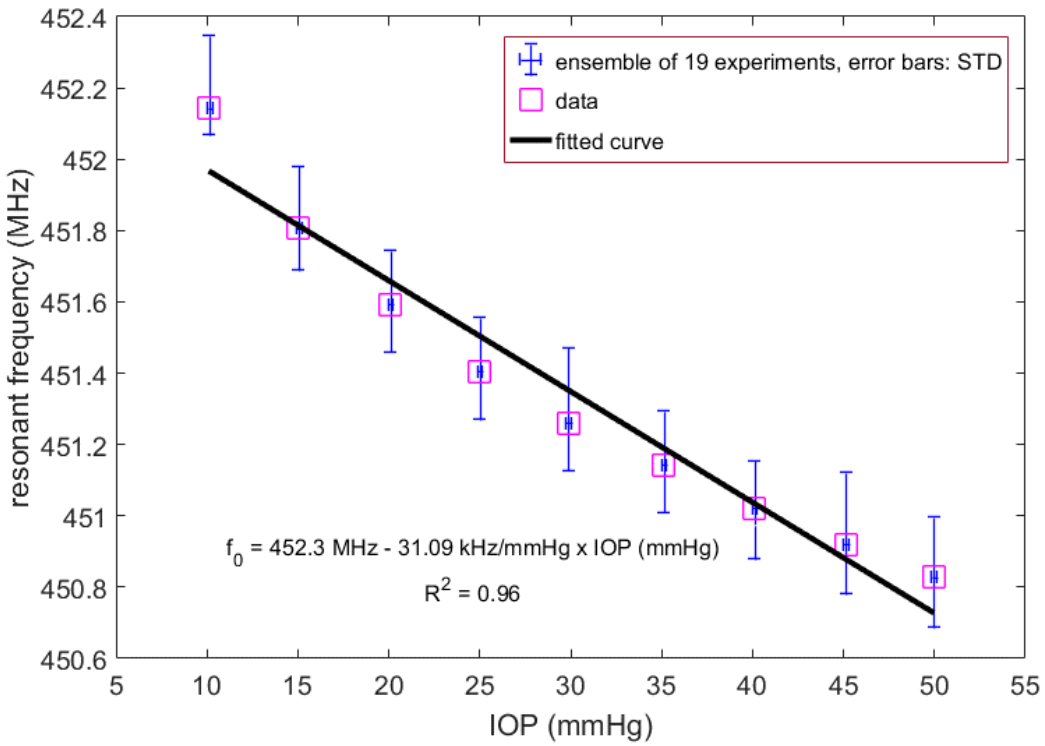

Figure 5.11. The ensemble of the experiments showing the mean values of the measured resonant frequencies with standard deviation error bars.

6. CONCLUSION AND FUTURE WORK

In this thesis, passive sensor application for non-invasive and continuous monitoring of glaucoma is presented. The sensor is fabricated and embedded in CL, which enables continuous monitoring of glaucoma to improve diagnosis accuracy and treatment of glaucoma. For this thesis, a resonator sensor was designed so that its resonant frequency varies with the changing ROC which is well correlated with IOP. The resonant frequency of the resonator is measured by measuring the scattering characteristics of the sensor system with an antenna which is tuned to be coupled to the resonator.

Firstly, SRR based CLSs given in the previous work was further analyzed with FDTD simulations. Results showed that using SRR for CLS is not suitable as its resonance response to the conductivity is bad. Mechanical FEM simulations of CL on the eye model was also performed to analyze the displacements of the CL caused by the IOP. Also, feasibility of the bending of the resonators was also analyzed.

To improve the CLS response to the conductivity, antenna coupled BC-SRR based CLS was designed and analyzed. Theoretical and simulation based analysis for tunable antennas were shown and resonance behaviors of CLSs were measured with those tunable antennas. BC-SRR based sensors were analyzed in terms of metal thickness and substrate tangent loss. Further simulations were performed to analyze the resonance behavior of the CLS on eye-globe for changing ROC levels.

Furthermore, planar sensors were bent to be embedded in CL with designed molds. For the in-vitro setup, PDMS eye model is designed and produced. In-vitro characterization of the antenna coupled BC-SRR based CLSs with respect to varying IOP levels are given in this thesis. The monotonic change in the resonant frequency of the CLS could be measured for varying values of IOP values. With respect to the measurement results, 3 dB resolution of the CLS is calculated as 1.98 mmHg. The final design parameters of the antenna coupled CLS system and the achieved performance metrics are given in Table 6.1.

Table 6.1. The final design parameters of the antenna coupled CLS system and the achieved performance metrics.

CLS	
Radii of the rings	4 mm
Widths of the rings	1.5 mm
Gap distance of the rings	1 mm
Distance between the rings	37.5 µm
Thickness of the metals	18 µm
Substrate material of the resonator	PI
CL Material	PUA
Radius of curvature of the CLS	8.6 mm
Centre thickness of the CLS	600 µm
Antenna	
Average radius of the metal	21 mm
Width of the metal	2.4 mm
Thickness of the metal	35 µm
Gap distance for the input port	1.2 mm
Substrate material	FR-4
Substrate thickness	130 µm
Tuning Capacitance	0.8 pF
Performance metrics of the antenna coupled CLS system	
Average resonant frequency shift with respect to IOP	−31.09 kHz/mmHg
Average quality factor	7349
Average resonant frequency	451.347 MHz
3 dB resolution	1.98 mmHg

In the end, this device is planned to be used as a noninvasive CLS for glaucoma monitoring. Reproducibility and the biocompatibility of the CLS and was maintained by fabrication of the biocompatible materials. Also, in-vitro characterization of the CLS and antenna structures, which are parts of the developed system, were performed.

6.1. Future Work

According to the applied static pressure (IOP), the monotonic change in the resonant frequency of the BC-SRR embedded CLS could be measured and it is of great importance to support these results with dynamic tests.

Furthermore, the change in the ROC of the designed eye model should be measured with respect to changing values of the IOP and resolution of the sensor should be measured again as the sensor is following the changes in the ROC.

While performing the experiments, the CLS was placed on the hydrophobic PDMS mechanical eye. In addition, the sensor is embedded in PUA, which is also a hydrophobic material. Therefore, in the experiments, the tear fluid between the eye and the CLS could not be mimicked, which is an important parameter that might affect the results.

Moreover, using a hydrophobic material for the CL reduces the comfort for the patient. Therefore, a hydrophilic coating on the CL or changing the CL material should be considered. Also, to ensure the biocompatibility, cytotoxicity tests for the resonators and CLSs should be performed.

REFERENCES

1. Hjortdal, J. Ø. and P. K. Jensen, "In vitro measurement of corneal strain, thickness, and curvature using digital image processing", *Acta Ophthalmologica Scandinavica*, Vol. 73, No. 1, pp. 5–11, 1995.

2. Calikoglu, A., G. Dundar, A. D. Yalcinkaya and H. Torun, "Laser-Machined Split-Ring Resonators Embedded in a Polymer Matrix for Glaucoma Monitoring", *Multidisciplinary Digital Publishing Institute Proceedings*, Vol. 1(4), p. 531, 2017.

3. Ge, G., W. Huang, J. Shao and X. Dong, "Recent progress of flexible and wearable strain sensors for human-motion monitoring", *Journal of Semiconductors*, Vol. 39, No. 1, p. 011012, 2018.

4. Klosterhoff, B. S., M. Tsang, D. She, K. G. Ong, M. G. Allen, N. J. Willett and R. E. Guldberg, "Implantable sensors for regenerative medicine", *Journal of biomechanical engineering*, Vol. 139, No. 2, p. 021009, 2017.

5. Li, Y.-Q., Y. A. Samad and K. Liao, "From cotton to wearable pressure sensor", *Journal of Materials Chemistry A*, Vol. 3, No. 5, pp. 2181–2187, 2015.

6. Chen, X., B. Assadsangabi, Y. Hsiang and K. Takahata, "Enabling Angioplasty-Ready "Smart" Stents to Detect In-Stent Restenosis and Occlusion", *Advanced Science*, Vol. 5, No. 5, p. 1700560, 2018.

7. Wang, C., D. Hwang, Z. Yu, K. Takei, J. Park, T. Chen, B. Ma and A. Javey, "User-interactive electronic skin for instantaneous pressure visualization", *Nature materials*, Vol. 12, No. 10, p. 899, 2013.

8. Wood, R. J., Y.-L. Park, C. S. Majidi, B.-r. Chen, L. Stirling, C. J. Walsh, R. Nagpal, D. Young and Y. Menguc, "Artificial skin and elastic strain sensor", , Dec. 12 2017, uS Patent 9,841,331.

9. Li, Y.-Q., P. Huang, W.-B. Zhu, S.-Y. Fu, N. Hu and K. Liao, "Flexible wire-shaped strain sensor from cotton thread for human health and motion detection", *Scientific reports*, Vol. 7, p. 45013, 2017.

10. Boutry, C. M., Y. Kaizawa, B. C. Schroeder, A. Chortos, A. Legrand, Z. Wang, J. Chang, P. Fox and Z. Bao, "A stretchable and biodegradable strain and pressure sensor for orthopaedic application", *Nature Electronics*, Vol. 1, No. 5, p. 314, 2018.

11. Natta, L., V. Mastronardi, F. Guido, L. Algieri, S. Puce, F. Pisano, F. Rizzi, R. Pulli, A. Qualtieri and M. De Vittorio, "Soft and flexible piezoelectric smart patch for vascular graft monitoring based on Aluminum Nitride thin film", *Scientific reports*, Vol. 9, No. 1, p. 8392, 2019.

12. Chen, S., Z. Lou, D. Chen, K. Jiang and G. Shen, "Polymer-Enhanced Highly Stretchable Conductive Fiber Strain Sensor Used for Electronic Data Gloves", *Advanced Materials Technologies*, Vol. 1, No. 7, p. 1600136, 2016.

13. Melik, R., E. Unal, N. Kosku Perkgoz, C. Puttlitz and H. V. Demir, "Flexible metamaterials for wireless strain sensing", *Applied Physics Letters*, Vol. 95, No. 18, p. 181105, 2009.

14. Sydoruk, O., E. Tatartschuk, E. Shamonina and L. Solymar, "Analytical formulation for the resonant frequency of split rings", *Journal of applied physics*, Vol. 105, No. 1, p. 014903, 2009.

15. Hesmer, F., E. Tatartschuk, O. Zhuromskyy, A. A. Radkovskaya, M. Shamonin, T. Hao, C. J. Stevens, G. Faulkner, D. J. Edwards and E. Shamonina, "Coupling mechanisms for split ring resonators: Theory and experiment", *physica status solidi (b)*, Vol. 244, No. 4, pp. 1170–1175, 2007.

16. Smith, D. R., J. B. Pendry and M. C. Wiltshire, "Metamaterials and negative refractive index", *Science*, Vol. 305, No. 5685, pp. 788–792, 2004.

17. Benedetti, A., C. Sibilia and M. Bertolotti, "Wide band negative magnetic permeability materials (NMPM) with composite metal-semiconductor structures based on the Drude model, and applications to negative-refractive index (NIM)", *Optics express*, Vol. 15, No. 11, pp. 6534–6545, 2007.

18. Klein, M., C. Enkrich, M. Wegener, C. Soukoulis and S. Linden, "Single-slit split-ring resonators at optical frequencies: limits of size scaling", *Optics letters*, Vol. 31, No. 9, pp. 1259–1261, 2006.

19. Bait-Suwailam, M. and O. Ramahi, "Simultaneous switching noise mitigation in high-speed circuits using complementary split-ring resonators", *Electronics letters*, Vol. 46, No. 8, pp. 563–564, 2010.

20. Liang, Y., H. Yu, W. Zhang and F. Lin, "CMOS sub-THz on-chip modulator by stacked split ring resonator with high-extinction ratio", *2015 IEEE International Symposium on Radio-Frequency Integration Technology (RFIT)*, pp. 67–69, IEEE, 2015.

21. Camli, B., E. Kusakci, B. Lafci, S. Salman, H. Torun and A. Yalcinkaya, "A microwave ring resonator based glucose sensor", *Procedia Engineering*, Vol. 168, pp. 465–468, 2016.

22. Camli, B., E. Kusakci, B. Lafci, S. Salman, H. Torun and A. D. Yalcinkaya, "Cost-effective, microstrip antenna driven ring resonator microwave biosensor for biospecific detection of glucose", *IEEE Journal of Selected Topics in Quantum Electronics*, Vol. 23, No. 2, pp. 404–409, 2017.

23. Melik, R., E. Unal, N. K. Perkgoz, C. Puttlitz and H. V. Demir, "Metamaterial-based wireless strain sensors", *Applied Physics Letters*, Vol. 95, No. 1, p. 011106, 2009.

24. Martin, F., F. Falcone, J. Bonache, R. Marques and M. Sorolla, "Miniaturized coplanar waveguide stop band filters based on multiple tuned split ring resonators",

IEEE Microwave and Wireless Components Letters, Vol. 13, No. 12, pp. 511–513, 2003.

25. Lubkowski, G., C. Damm, B. Bandlow, R. Schuhmann, M. Schüßler and T. Weiland, "Metamaterial Loaded Waveguides for Miniaturized Filter Applications", *Frequenz*, Vol. 62, No. 3-4, pp. 71–74, 2008.

26. Dong, Y., H. Toyao and T. Itoh, "Design and characterization of miniaturized patch antennas loaded with complementary split-ring resonators", *IEEE Transactions on antennas and propagation*, Vol. 60, No. 2, pp. 772–785, 2011.

27. Alici, K. B. and E. Ozbay, "Electrically small split ring resonator antennas", *Journal of applied physics*, Vol. 101, No. 8, p. 083104, 2007.

28. Kim, O. S. and O. Breinbjerg, "Miniaturized planar split-ring resonator antenna", *2009 IEEE Antennas and Propagation Society International Symposium*, pp. 1–4, IEEE, 2009.

29. Scanlon, W. G., B. Burns and N. E. Evans, "Radiowave propagation from a tissue-implanted source at 418 MHz and 916.5 MHz", *IEEE Transactions on Biomedical Engineering*, Vol. 47, No. 4, pp. 527–534, 2000.

30. Chen, T., S. Li and H. Sun, "Metamaterials application in sensing", *Sensors*, Vol. 12, No. 3, pp. 2742–2765, 2012.

31. Quigley, H. A. and A. T. Broman, "The number of people with glaucoma worldwide in 2010 and 2020", *British journal of ophthalmology*, Vol. 90, No. 3, pp. 262–267, 2006.

32. François, J., "Genetics and primary open-angle glaucoma", *American journal of ophthalmology*, Vol. 61, No. 4, pp. 652–665, 1966.

33. Weinreb, R. N. and P. T. Khaw, "Primary open-angle glaucoma", *The Lancet*, Vol.

363, No. 9422, pp. 1711–1720, 2004.

34. ALLEN, L., H. M. BURIAN and A. E. BRALEY, "A New Concept of the Development of theAnterior Chamber Angle: Its Relationship to Developmental Glaucoma and Other Structural Anomalies", *JAMA Ophthalmology*, Vol. 53, No. 6, pp. 783–798, 06 1955.

35. Mokbel, T. H. and A. A. Ghanem, "Correlation of central corneal thickness and optic nerve head topography in patients with primary open-angle glaucoma", *Oman journal of ophthalmology*, Vol. 3, No. 2, p. 75, 2010.

36. Hu, C. X., C. Zangalli, M. Hsieh, L. Gupta, A. L. Williams, J. Richman and G. L. Spaeth, "What do patients with glaucoma see? Visual symptoms reported by patients with glaucoma", *The American journal of the medical sciences*, Vol. 348, No. 5, pp. 403–409, 2014.

37. Kim, J. M., H. Kyung, S. H. Shim, P. Azarbod and J. Caprioli, "Location of initial visual field defects in glaucoma and their modes of deterioration", *Investigative ophthalmology & visual science*, Vol. 56, No. 13, pp. 7956–7962, 2015.

38. Medeiros, F. A., G. Vizzeri, L. M. Zangwill, L. M. Alencar, P. A. Sample and R. N. Weinreb, "Comparison of retinal nerve fiber layer and optic disc imaging for diagnosing glaucoma in patients suspected of having the disease", *Ophthalmology*, Vol. 115, No. 8, pp. 1340–1346, 2008.

39. Yolcu, U., A. Ilhan and A. Tas, "Conventional Intraocular Pressure Measurement Techniques", *Glaucoma-Intraocular Pressure and Aqueous Dynamics*, IntechOpen, 2016.

40. Sampaolesi, R., J. R. Sampaolesi and J. Zárate, "Applanation Tonometry", *The Glaucomas*, pp. 123–147, Springer, 2014.

41. Chen, P.-J., S. Saati, R. Varma, M. S. Humayun and Y.-C. Tai, "Wireless intraoc-

ular pressure sensing using microfabricated minimally invasive flexible-coiled LC sensor implant", *Journal of Microelectromechanical Systems*, Vol. 19, No. 4, pp. 721–734, 2010.

42. Leonardi, M., P. Leuenberger, D. Bertrand, A. Bertsch and P. Renaud, "First steps toward noninvasive intraocular pressure monitoring with a sensing contact lens", *Investigative ophthalmology & visual science*, Vol. 45, No. 9, pp. 3113–3117, 2004.

43. Leonardi, M., E. M. Pitchon, A. Bertsch, P. Renaud and A. Mermoud, "Wireless contact lens sensor for intraocular pressure monitoring: assessment on enucleated pig eyes", *Acta ophthalmologica*, Vol. 87, No. 4, pp. 433–437, 2009.

44. Ekinci, G., A. D. Yalcinkaya, G. Dundar and H. Torun, "Split-Ring Resonator-Based Strain Sensor on Flexible Substrates for Glaucoma Detection", *Journal of Physics: Conference Series*, Vol. 757(1), p. 012019, IOP Publishing, 2016.

45. Ekinci, G., A. Calikoglu, S. N. Solak, A. D. Yalcinkaya, G. Dundar and H. Torun, "Split-ring resonator-based sensors on flexible substrates for glaucoma monitoring", *Sensors and Actuators A: Physical*, Vol. 268, pp. 32–37, 2017.

46. DuPont, *Pyralux AP Clad Technical Data Sheet*, `https://www.pragoboard.cz/download/pyralux_ap.pdf`, accessed in June 2019.

47. Benedetto, D., D. Shah and H. Kaufman, "The instilled fluid dynamics and surface chemistry of polymers in the preocular tear film.", *Investigative Ophthalmology & Visual Science*, Vol. 14, No. 12, pp. 887–902, 1975.

48. Prydal, J. I., P. Artal, H. Woon and F. W. Campbell, "Study of human precorneal tear film thickness and structure using laser interferometry.", *Investigative ophthalmology & visual science*, Vol. 33, No. 6, pp. 2006–2011, 1992.

49. Dodig, H., A. Peratta and D. Poljak, "Analysis method for the heating of the human eye exposed to high frequency electromagnetic fields", *Journal of Commu-*

nications Software and Systems, Vol. 3, No. 1, pp. 3–10, 2007.

50. Chou, N., J. Jeong and S. Kim, "Crack-free and reliable lithographical patterning methods on PDMS substrate", *Journal of Micromechanics and Microengineering*, Vol. 23, No. 12, p. 125035, 2013.

51. Tajik, A. and H. Jahed, "Standalone Tensile Testing of Thin Film Materials for MEMS/NEMS Applications", *Microelectromechanical Systems and Devices*, p. 435, 2012.

52. DuPont, *Kapton: Summary of Properties*, https://www.dupont.com/content/dam/dupont/products-and-services/membranes-and-films/polyimde-films/documents/DEC-Kapton-summary-of-properties.pdf, accessed in June 2019.

53. MERCK, *Technical Data Sheet: AZ5214 E Photoresist*, https://www.microchemicals.com/micro/tds_az_5214e_photoresist.pdf, accessed in June 2019.

54. Company, T. D. C., *Technical Data Sheet: SYLGARD 184 Silicone Elastomer*, https://consumer.dow.com/content/dam/dcc/documents/en-us/productdatasheet/11/11-31/11-3184-sylgard-184-elastomer.pdf?iframe=true, accessed in June 2019.

55. Elveflow, *PDMS thickness vs spin coating speed*, https://www.elveflow.com/microfluidic/PDMS%20thickness%20VS%20spin%20speed.pdf, accessed in June 2019.

56. *SU8 2000 Processing Guidelines*, http://microchem.com/pdf/SU-82000DataSheet2000_5thru2015Ver4.pdf, accessed in June 2019.

57. Jin, X., Q. Wang, W. Q. Khan, Z. H. Tang and X. M. Yao, "Analytical computation of distributed capacitance for NFC coil antenna", *IEICE Electronics Express*, Vol. 14, No. 2, pp. 20161147–20161147, 2017.

58. Jiang, Z., P. Excell and Z. Hejazi, "Calculation of distributed capacitances of spiral resonators", *IEEE Transactions on Microwave Theory and Techniques*, Vol. 45, No. 1, pp. 139–142, 1997.

59. Mohan, S. S., M. del Mar Hershenson, S. P. Boyd and T. H. Lee, "Simple accurate expressions for planar spiral inductances", *IEEE Journal of solid-state circuits*, Vol. 34, No. 10, pp. 1419–1424, 1999.

60. Marqués, R., F. Mesa, J. Martel and F. Medina, "Comparative analysis of edge- and broadside-coupled split ring resonators for metamaterial design-theory and experiments", *IEEE Transactions on antennas and propagation*, Vol. 51, No. 10, pp. 2572–2581, 2003.

61. Vegesna, S. and M. A. Saed, "Compact two-layer microstrip bandpass filters using broadside-coupled resonators", *Progress In Electromagnetics Research*, Vol. 37, pp. 81–102, 2012.

62. Marqués, R., F. Martin and M. Sorolla, *Metamaterials with negative parameters: theory, design, and microwave applications*, Vol. 183, John Wiley & Sons, 2011.

63. HD-Microsystems, *PI 2600 Low stress applications*, `https://www.dupont.com/content/dam/dupont/products-and-services/electronic-and-electrical-materials/semiconductor-fabrication-and-packaging-materials/documents/PI-2600_ProcessGuide.pdf`, accessed in June 2019.

64. Nicolas, L., N. Burais, F. Buret, O. Fabregue, L. Krähenbühl, A. Nicolas, C. Poignard, R. Scoretti, N. Siauve and C. Vollaire, "Interactions between electromagnetic field and biological tissues: Questions, some answers and future trends", *International Compumag Society Newsletter*, Vol. 10, No. 2, pp. 4–9, 2003.

65. Prototyping, M., *VeroClear RGD810*, `https://www.midwestproto.com/sites/midwestproto.com/assets/files/default/VeroClear.pdf`, accessed in June 2019.

66. DuPont, *Silastic MDX4-4210 Biomedical Grade Elastomer*, https://www.dupont.com/content/dam/Dupont2.0/Products/transportation/Literature/Downloaded-TDS/0901b803809b782d.pdf, accessed in June 2019.

APPENDIX A: RESULTS OF THE SIMULATED ANTENNAS

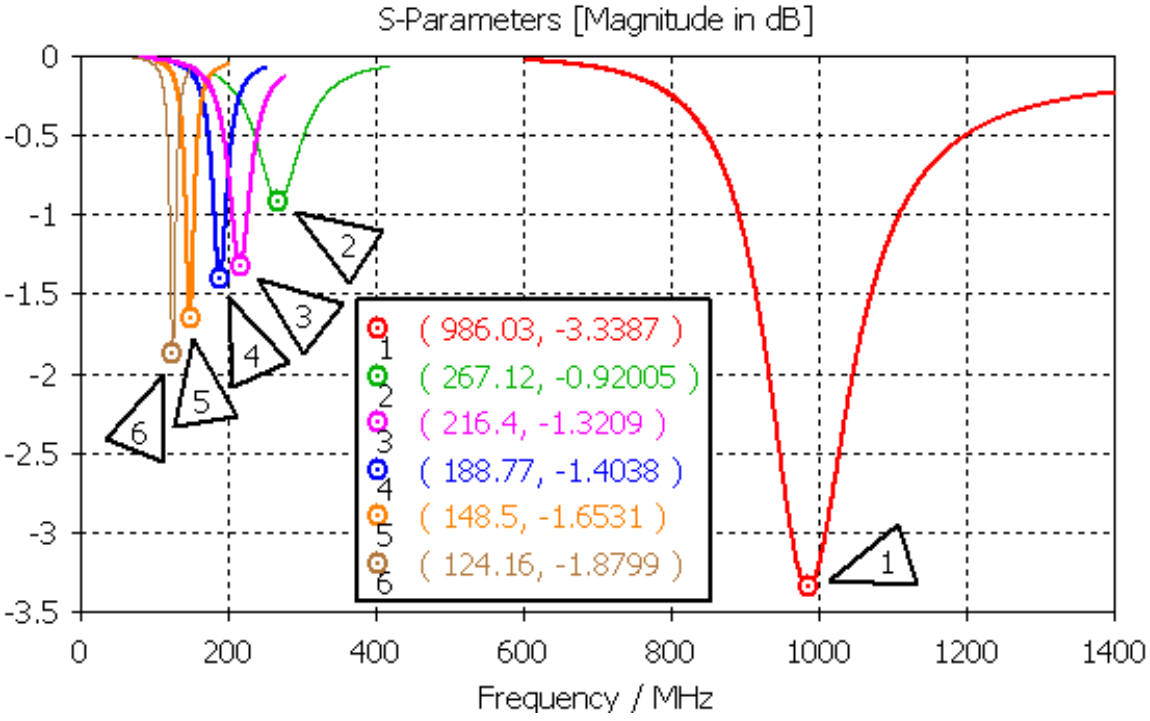

Figure A.1. s_{11} spectra of the simulated antennas without tuning capacitance (C_{tuning}) around their first modes.

Table A.1. Comparison of calculated and simulated first modes of antennas without tuning capacitance (C_{tuning}).

Number of turns (N)	**Calculated f_0 (MHz)**	**Simulated f_0 (MHz)**	**%Error**
1	986.93	986.03	0.09
2	261.69	267.12	-2.03
2.5	216.29	216.40	-0.05
3	184.97	188.77	-2.01
4	144.42	148.50	-2.75
5	119.17	124.16	-4.02

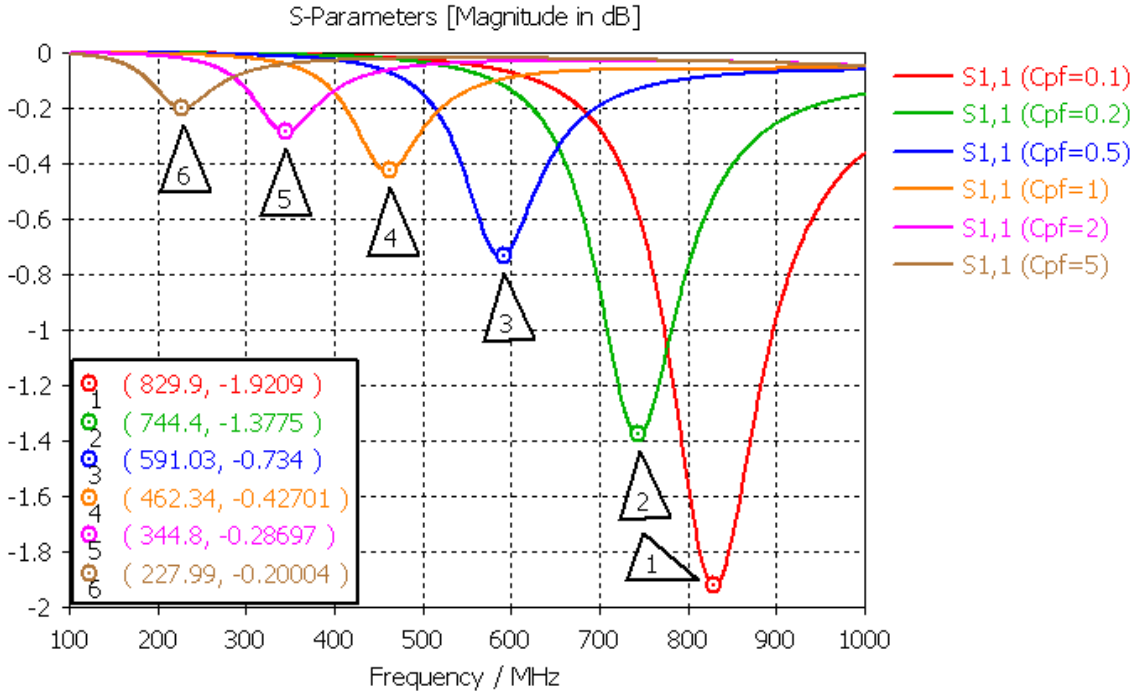

Figure A.2. s_{11} spectra of the folded dipole antennas ($N = 1$) with respect to varying tuning capacitance (C_{tuning}) values around their first modes.

Table A.2. Comparison of calculated and simulated first modes of folded dipole antennas ($N = 1$) with respect to varying tuning capacitance (C_{tuning}) values.

Tuning Capacitance (C_{tuning}) (pF)	**Calculated** f_0 (MHz)	**Simulated** f_0 (MHz)	%**Error**
0.1	839.13	829.90	1.11
0.2	742.53	744.40	-0.25
0.5	577.90	591.03	-2.22
1	448.93	462.34	-2.90
2	335.26	344.80	-2.77
5	219.78	227.99	-3.60

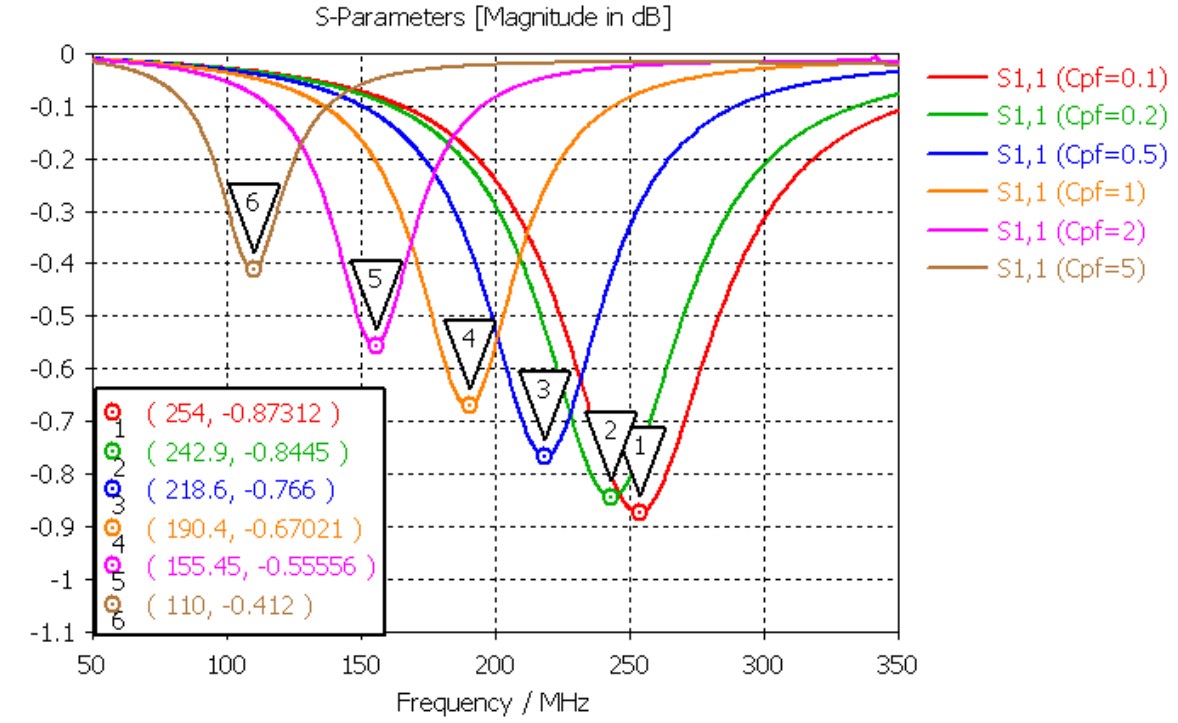

Figure A.3. s_{11} spectra of the spiral-dipole antennas with 2 turns ($N = 2$) with respect to varying tuning capacitance (C_{tuning}) values around their first modes.

Table A.3. Comparison of calculated and simulated first modes of spiral-dipole antennas with 2 turns ($N = 2$) with respect to varying tuning capacitance (C_{tuning}) values.

Tuning Capacitance (C_{tuning}) (pF)	**Calculated** f_0 (MHz)	**Simulated** f_0 (MHz)	%**Error**
0.1	249.66	254.00	-1.71
0.2	239.15	242.90	-1.54
0.5	214.13	218.60	-2.04
1	185.65	190.40	-2.50
2	151.74	155.45	-2.38
5	107.42	110.00	-2.35

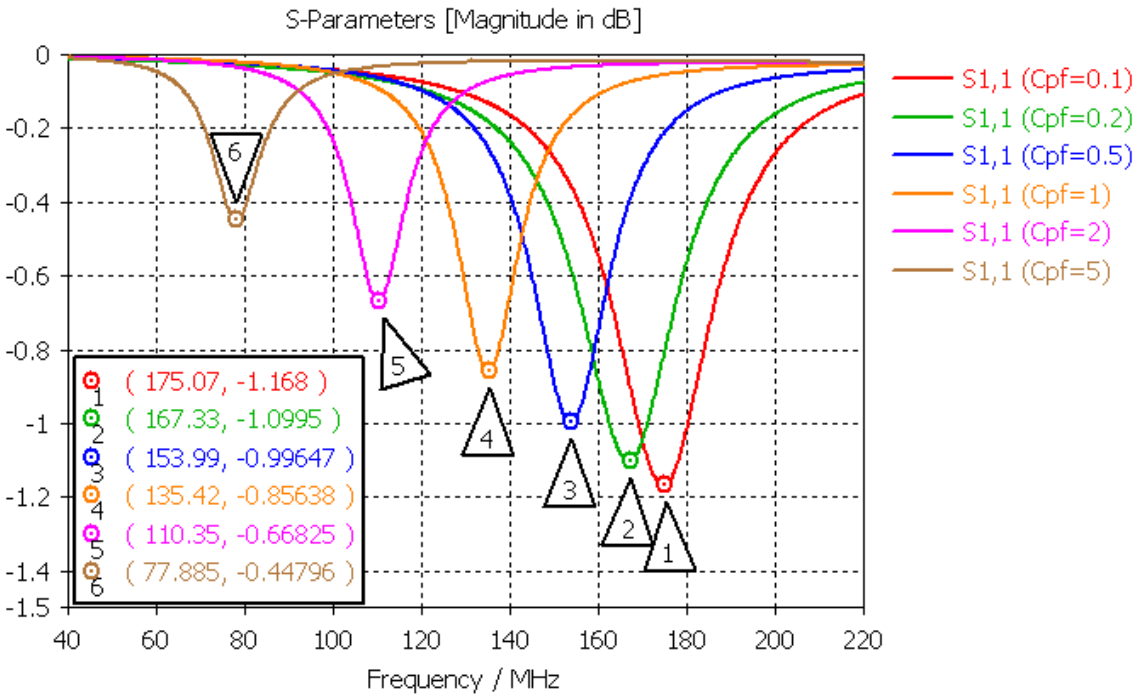

Figure A.4. s_{11} spectra of the spiral-dipole antennas with 3 turns ($N = 3$) with respect to varying tuning capacitance (C_{tuning}) values around their first modes.

Table A.4. Comparison of calculated and simulated first modes of spiral-dipole antennas with 3 turns ($N = 3$) with respect to varying tuning capacitance (C_{tuning}) values.

Tuning Capacitance (C_{tuning}) (pF)	**Calculated** f_0 (MHz)	**Simulated** f_0 (MHz)	**%Error**
0.1	176.77	175.07	0.97
0.2	169.57	167.33	1.34
0.5	152.32	153.99	-1.09
1	132.48	135.42	-2.17
2	108.64	110.35	-1.55
5	77.16	77.89	-0.94

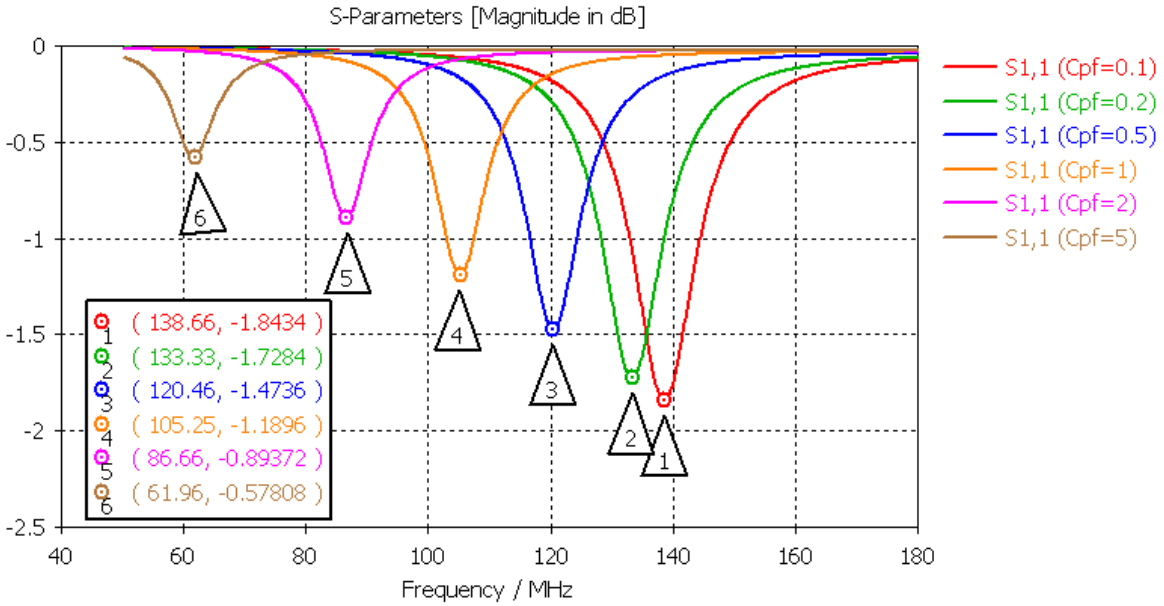

Figure A.5. s_{11} spectra of the spiral-dipole antennas with 4 turns ($N = 4$) with respect to varying tuning capacitance (C_{tuning}) values around their first modes.

Table A.5. Comparison of calculated and simulated first modes of spiral-dipole antennas with 4 turns ($N = 4$) with respect to varying tuning capacitance (C_{tuning}) values.

Tuning Capacitance (C_{tuning}) (pF)	**Calculated** f_0 (MHz)	**Simulated** f_0 (MHz)	%**Error**
0.1	138.23	138.66	-0.31
0.2	132.78	133.33	-0.41
0.5	119.63	120.46	-0.69
1	104.37	105.24	-0.82
2	85.86	86.66	-0.92
5	61.18	61.96	-1.27

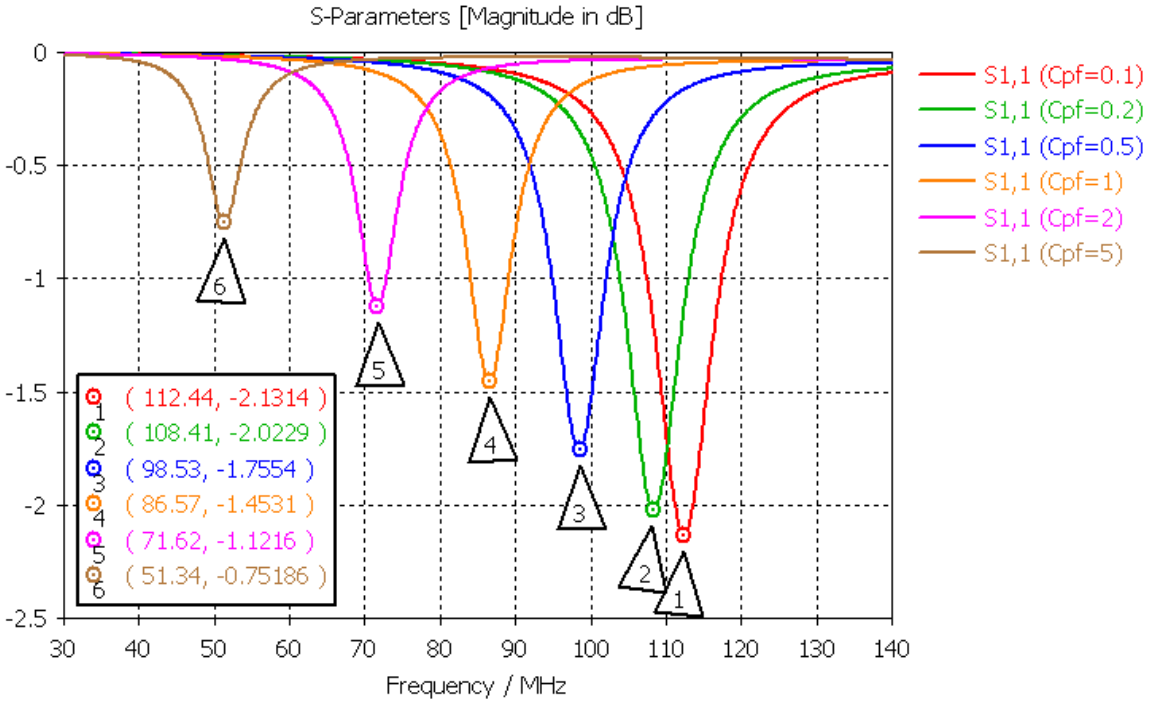

Figure A.6. s_{11} spectra of the spiral-dipole antennas with 5 turns ($N = 5$) with respect to varying tuning capacitance (C_{tuning}) values around their first modes.

Table A.6. Comparison of calculated and simulated first modes of spiral-dipole antennas with 5 turns ($N = 5$) with respect to varying tuning capacitance (C_{tuning}) values.

Tuning Capacitance (C_{tuning}) (pF)	**Calculated** f_0 (MHz)	**Simulated** f_0 (MHz)	**%Error**
0.1	114.24	112.44	1.60
0.2	109.87	108.41	1.35
0.5	99.27	98.53	0.75
1	86.86	86.57	0.34
2	71.67	71.62	0.08
5	51.23	51.34	-0.21

APPENDIX B: IN VITRO TEST RESULTS

Experimental data of the 19 trials, which the results are summarized in Figure 5.11:

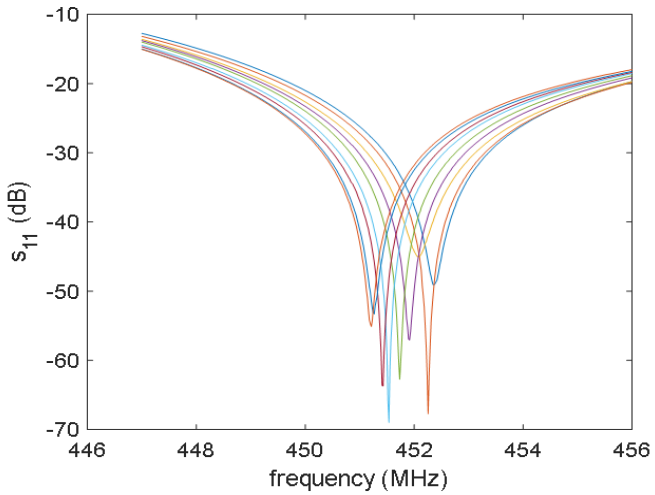

Figure B.1. Measured s_{11} spectra for trial 1 showing the resonant frequencies with respect to varying values of IOP levels.

Table B.1. Tabulated data obtained from trial 1.

	IOP (mmHg)	**Q**	f_0 (MHz)
1	10.22	1771	452.346
2	14.68	11731	452.256
3	20.12	1112	452.094
4	25.44	6156	451.914
5	29.60	10054	451.734
6	35.34	12200	451.536
7	40.62	12017	451.428
8	44.26	3022	451.266
9	50.34	4198	451.212

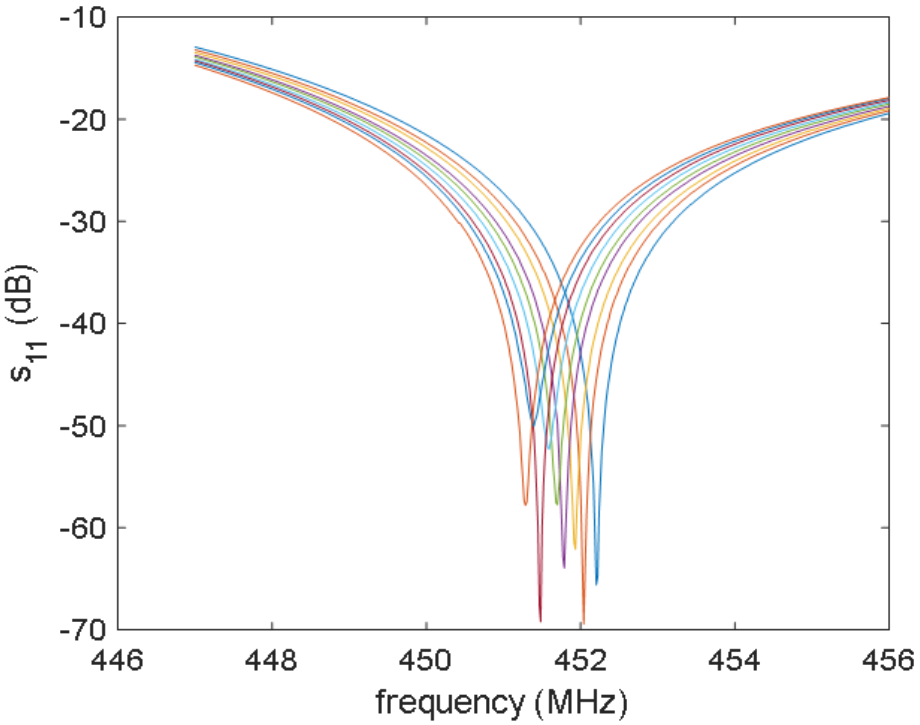

Figure B.2. Measured s_{11} spectra for trial 2 showing the resonant frequencies with respect to varying values of IOP levels.

Table B.2. Tabulated data obtained from trial 2.

	IOP (mmHg)	**Q**	f_0 (MHz)
1	9.52	9322	452.202
2	14.96	12373	452.040
3	20.22	8597	451.932
4	24.78	9675	451.788
5	30.34	6471	451.698
6	35.62	3843	451.590
7	39.88	11990	451.482
8	45.40	2513	451.392
9	50.22	6246	451.284

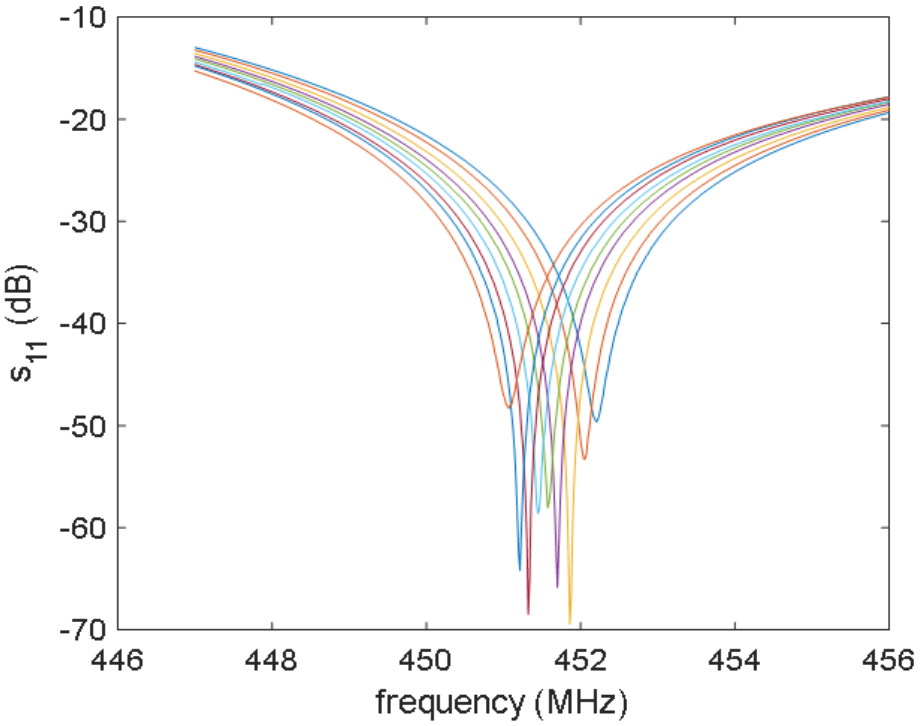

Figure B.3. Measured s_{11} spectra for trial 3 showing the resonant frequencies with respect to varying values of IOP levels.

Table B.3. Tabulated data obtained from trial 3.

	IOP (mmHg)	**Q**	f_0 (MHz)
1	10.50	2324	452.202
2	15.22	3068	452.040
3	19.78	11176	451.860
4	25.28	11713	451.698
5	29.88	4658	451.572
6	35.08	5443	451.446
7	40.12	11475	451.320
8	44.64	9545	451.212
9	49.88	2068	451.068

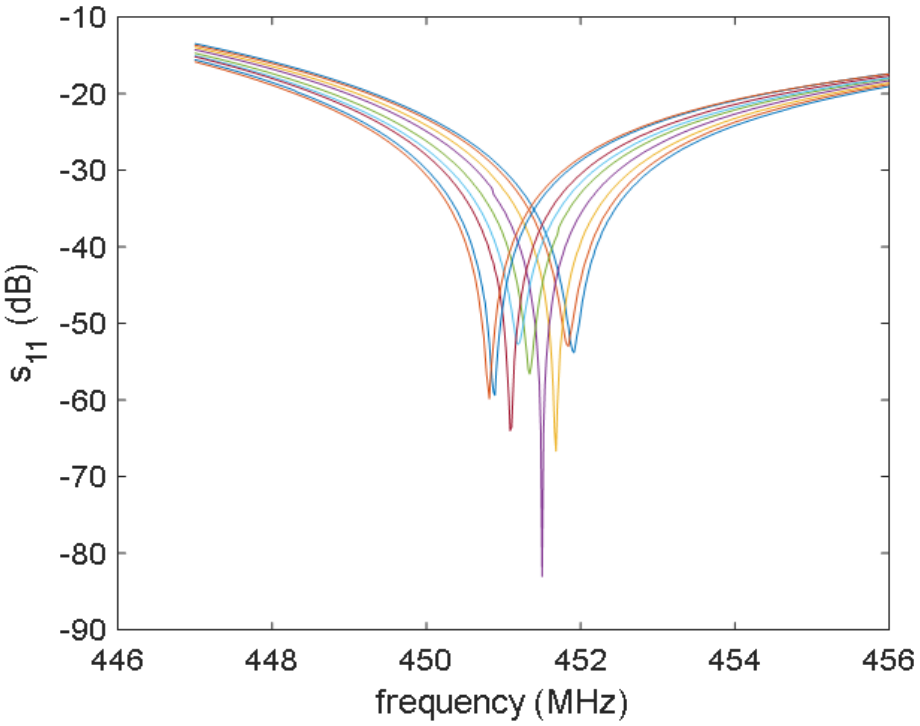

Figure B.4. Measured s_{11} spectra for trial 4 showing the resonant frequencies with respect to varying values of IOP levels.

Table B.4. Tabulated data obtained from trial 4.

	IOP (mmHg)	**Q**	f_0 (MHz)
1	9.88	4305	451.914
2	15.28	4340	451.842
3	20.36	12990	451.680
4	24.68	16942	451.500
5	30.26	6194	451.338
6	35.44	2997	451.194
7	40.12	9717	451.086
8	45.26	5380	450.888
9	49.86	5951	450.816

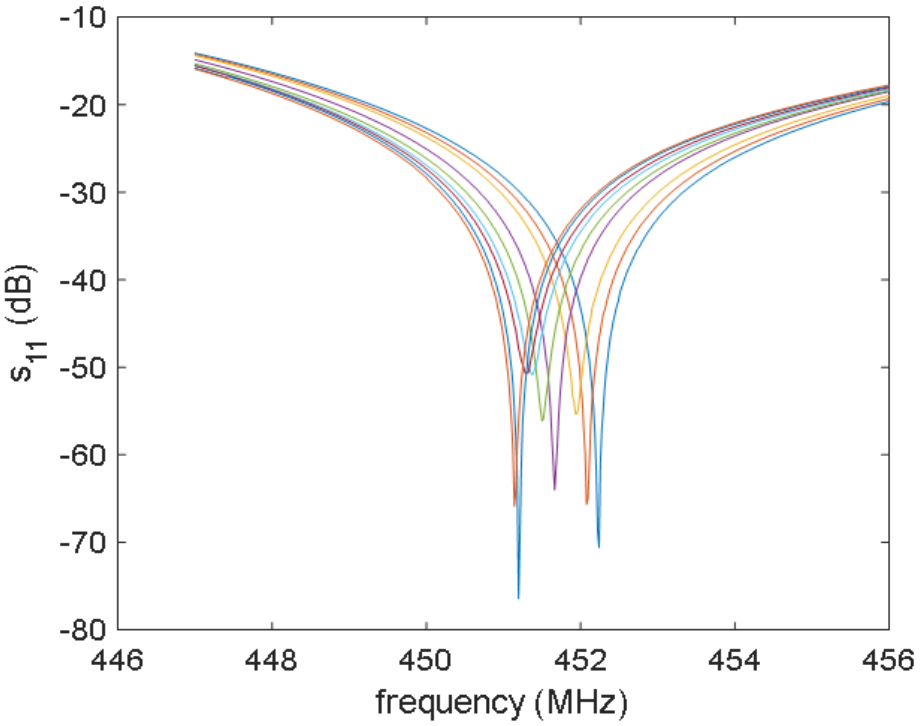

Figure B.5. Measured s_{11} spectra for trial 5 showing the resonant frequencies with respect to varying values of IOP levels.

Table B.5. Tabulated data obtained from trial 5.

	IOP (mmHg)	**Q**	f_0 (MHz)
1	10.44	11754	452.238
2	15.32	9963	452.076
3	19.68	3501	451.932
4	25.24	8192	451.662
5	29.64	4160	451.500
6	35.20	2513	451.374
7	39.78	2521	451.284
8	45.48	11046	451.194
9	50.44	8386	451.140

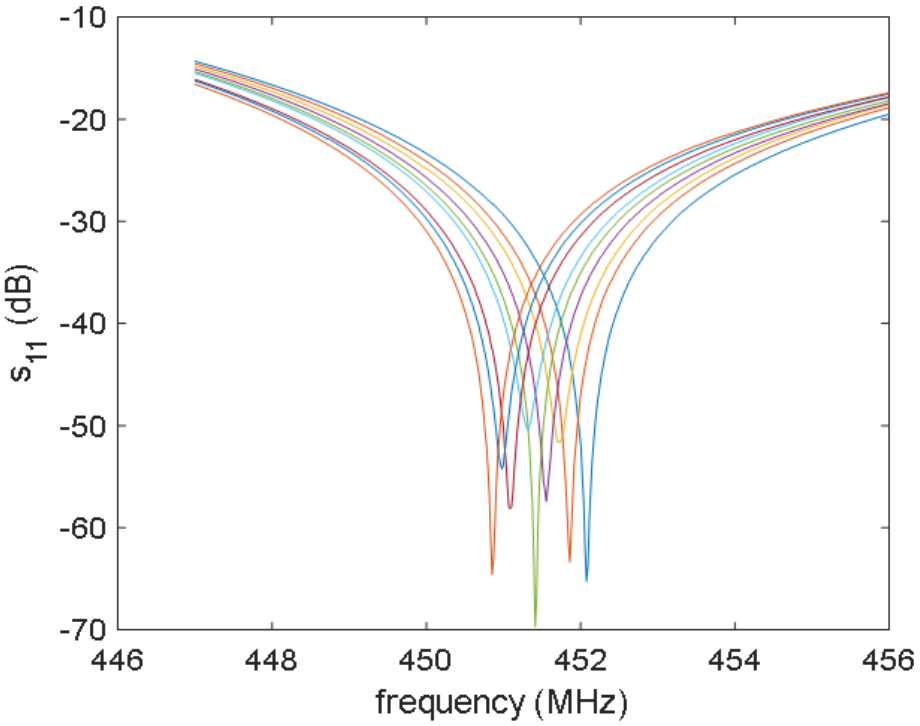

Figure B.6. Measured s_{11} spectra for trial 6 showing the resonant frequencies with respect to varying values of IOP levels.

Table B.6. Tabulated data obtained from trial 6.

	IOP (mmHg)	**Q**	f_0 (MHz)
1	10.68	12425	452.076
2	14.34	12771	451.860
3	20.14	2939	451.734
4	25.32	5778	451.554
5	29.74	12354	451.410
6	35.24	2712	451.320
7	40.24	6336	451.086
8	44.68	3888	450.978
9	49.66	11054	450.852

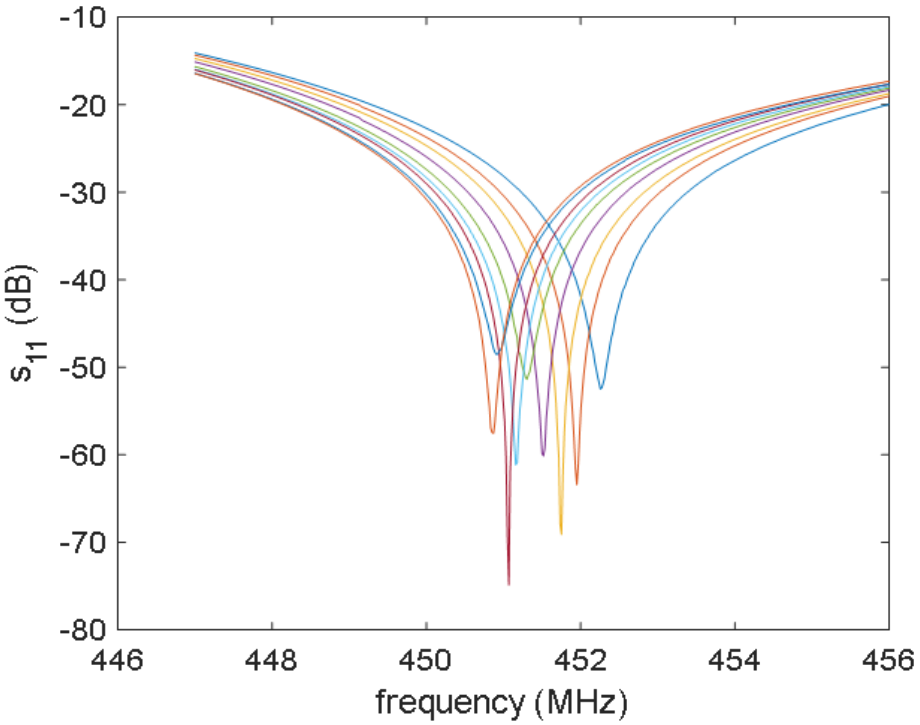

Figure B.7. Measured s_{11} spectra for trial 7 showing the resonant frequencies with respect to varying values of IOP levels.

Table B.7. Tabulated data obtained from trial 7.

	IOP (mmHg)	**Q**	f_0 (MHz)
1	9.46	3098	452.256
2	15.24	10000	451.950
3	20.34	13882	451.752
4	24.78	6099	451.518
5	29.68	2479	451.302
6	35.40	6262	451.158
7	40.36	14630	451.068
8	45.32	1735	450.906
9	49.32	4119	450.870

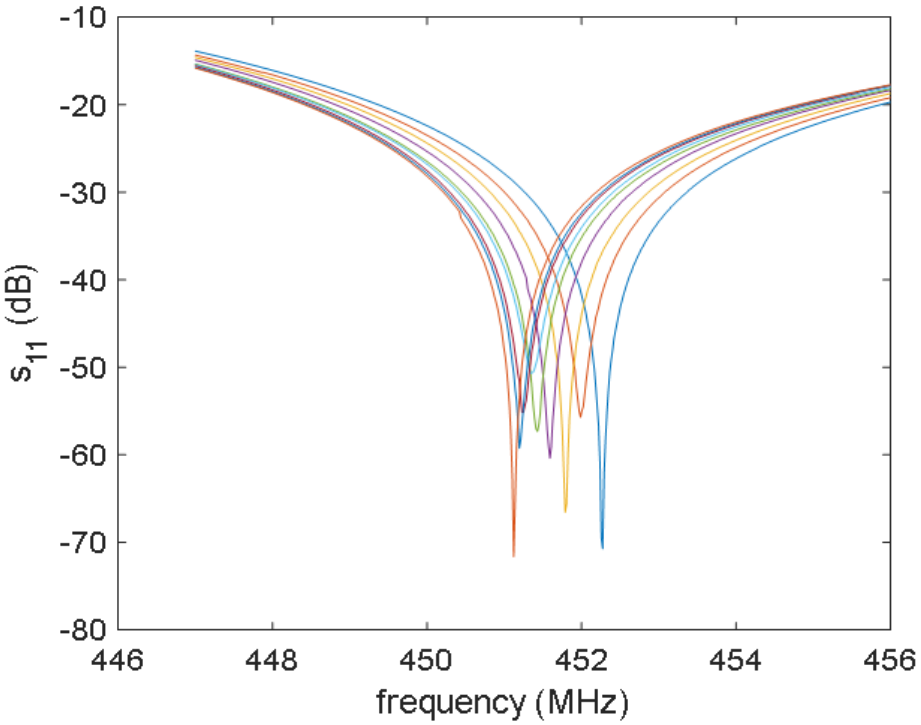

Figure B.8. Measured s_{11} spectra for trial 8 showing the resonant frequencies with respect to varying values of IOP levels.

Table B.8. Tabulated data obtained from trial 8.

	IOP (mmHg)	**Q**	f_0 (MHz)
1	9.88	10450	452.274
2	14.92	3839	451.986
3	19.80	9331	451.788
4	25.24	5808	451.590
5	29.12	4158	451.428
6	34.94	2506	451.356
7	40.12	3986	451.248
8	44.72	1206	451.194
9	50.16	13057	451.122

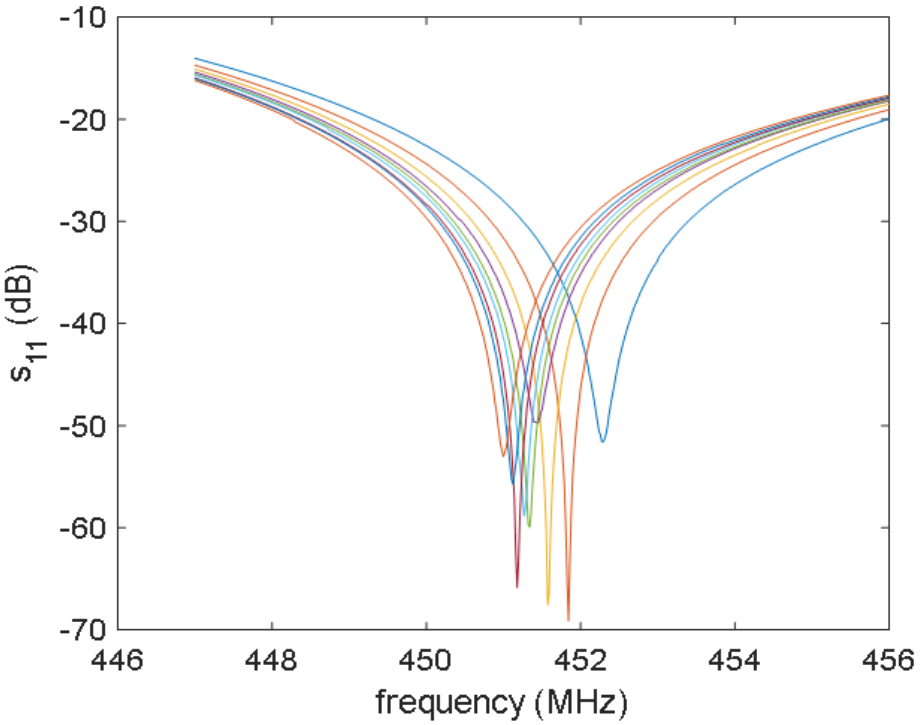

Figure B.9. Measured s_{11} spectra for trial 9 showing the resonant frequencies with respect to varying values of IOP levels.

Table B.9. Tabulated data obtained from trial 9.

	IOP (mmHg)	**Q**	f_0 (MHz)
1	9.70	2730	452.292
2	15.56	11020	451.842
3	20.36	10407	451.572
4	24.74	2532	451.446
5	30.44	6277	451.338
6	34.66	5325	451.266
7	40.32	9153	451.176
8	44.84	4091	451.122
9	49.68	3042	450.996

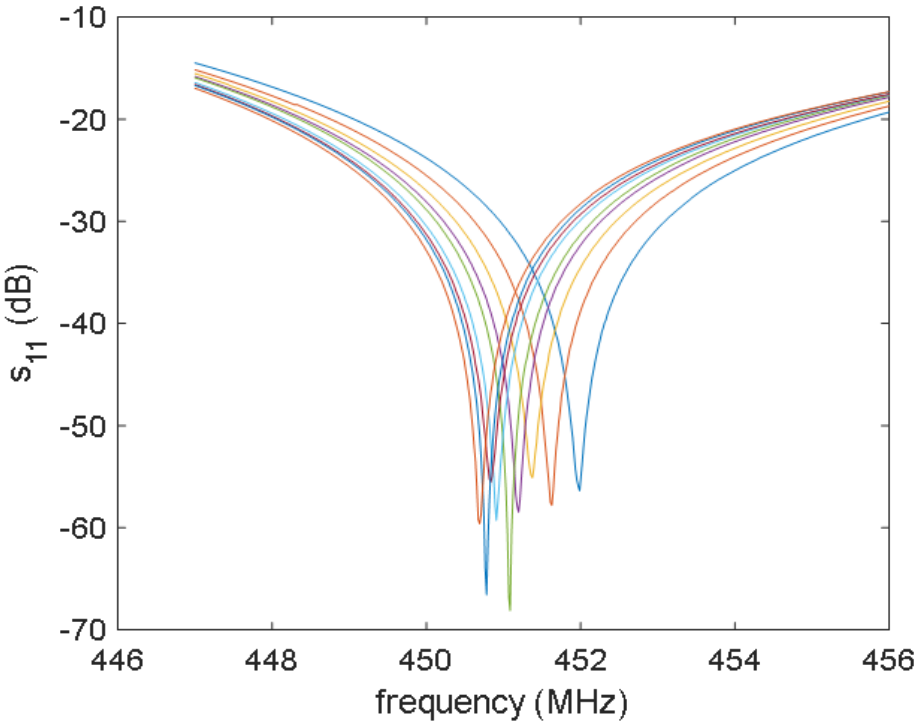

Figure B.10. Measured s_{11} spectra for trial 10 showing the resonant frequencies with respect to varying values of IOP levels.

Table B.10. Tabulated data obtained from trial 10.

	IOP (mmHg)	**Q**	f_0 (MHz)
1	10.32	6119	451.986
2	15.14	6778	451.626
3	20.72	4851	451.374
4	24.64	6566	451.194
5	29.70	12540	451.086
6	35.22	6978	450.906
7	39.68	4112	450.834
8	45.68	11304	450.780
9	50.62	6362	450.690

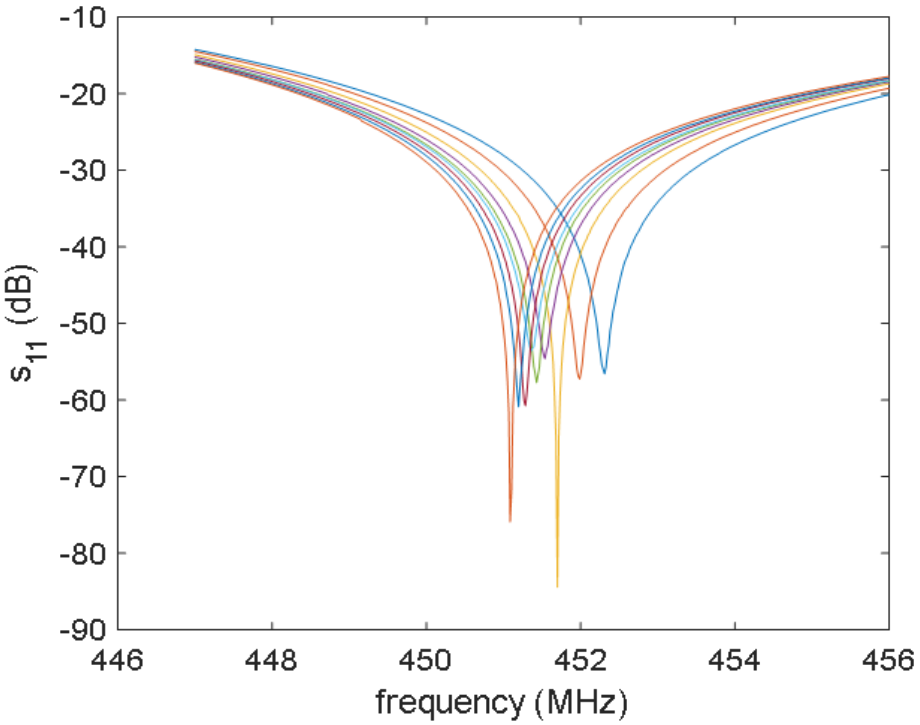

Figure B.11. Measured s_{11} spectra for trial 11 showing the resonant frequencies with respect to varying values of IOP levels.

Table B.11. Tabulated data obtained from trial 11.

	IOP (mmHg)	**Q**	f_0 (MHz)
1	10.46	3867	452.310
2	15.34	4041	451.986
3	19.88	18156	451.698
4	25.14	3176	451.536
5	29.68	5045	451.428
6	35.62	3161	451.356
7	40.42	9310	451.284
8	45.24	10047	451.194
9	49.68	14721	451.086

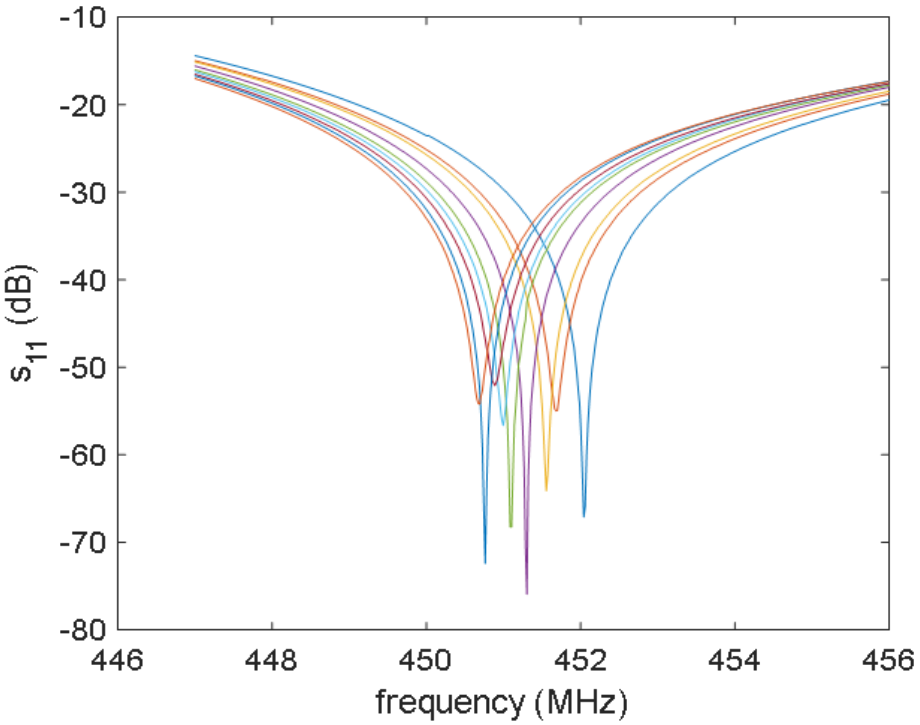

Figure B.12. Measured s_{11} spectra for trial 12 showing the resonant frequencies with respect to varying values of IOP levels.

Table B.12. Tabulated data obtained from trial 12.

	IOP (mmHg)	**Q**	f_0 (MHz)
1	10.28	9551	452.040
2	14.86	3885	451.680
3	19.94	11165	451.554
4	25.06	16584	451.302
5	29.48	11270	451.104
6	35.20	3766	450.996
7	39.82	2831	450.888
8	45.68	13001	450.762
9	49.58	4124	450.690

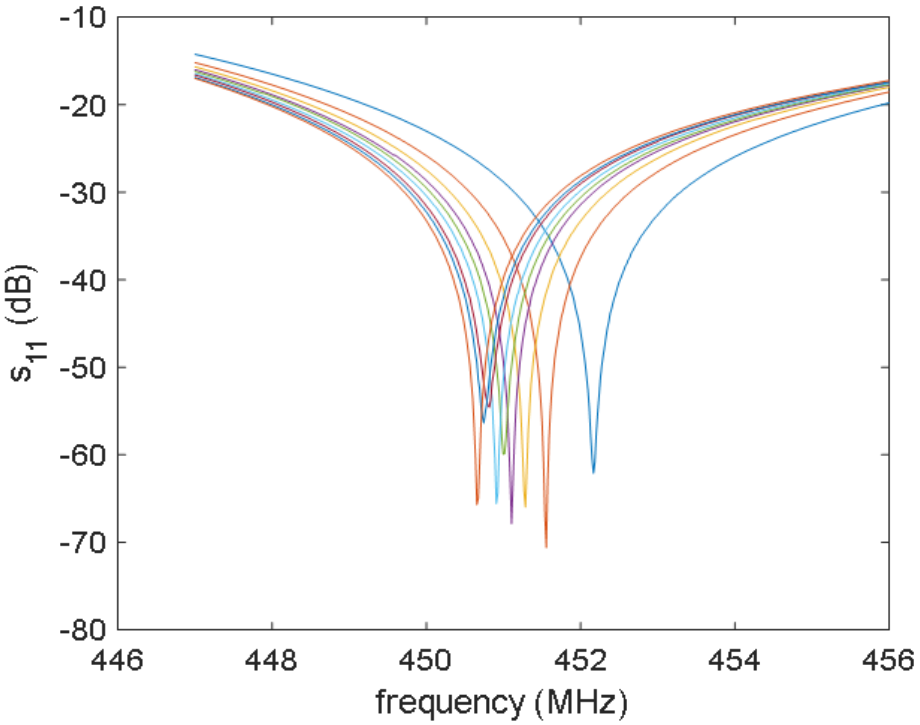

Figure B.13. Measured s_{11} spectra for trial 13 showing the resonant frequencies with respect to varying values of IOP levels.

Table B.13. Tabulated data obtained from trial 13.

	IOP (mmHg)	**Q**	f_0 (MHz)
1	10.26	8381	452.166
2	14.68	12049	451.554
3	20.12	11564	451.284
4	25.42	10339	451.104
5	30.30	9351	450.996
6	34.84	11449	450.906
7	40.14	4784	450.816
8	45.24	5741	450.744
9	49.88	11073	450.654

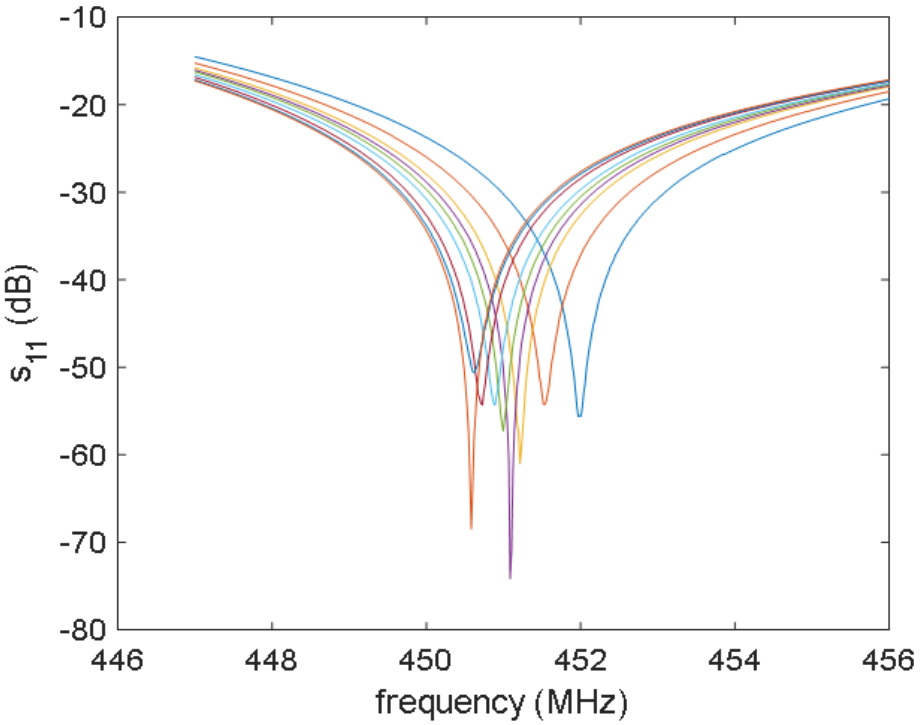

Figure B.14. Measured s_{11} spectra for trial 14 showing the resonant frequencies with respect to varying values of IOP levels.

Table B.14. Tabulated data obtained from trial 14.

	IOP (mmHg)	**Q**	f_0 (MHz)
1	10.52	6190	451.968
2	14.76	3973	451.536
3	20.46	10676	451.212
4	25.10	13404	451.086
5	30.44	5489	450.996
6	34.82	3908	450.888
7	40.32	3092	450.726
8	45.42	2474	450.618
9	49.98	12041	450.582

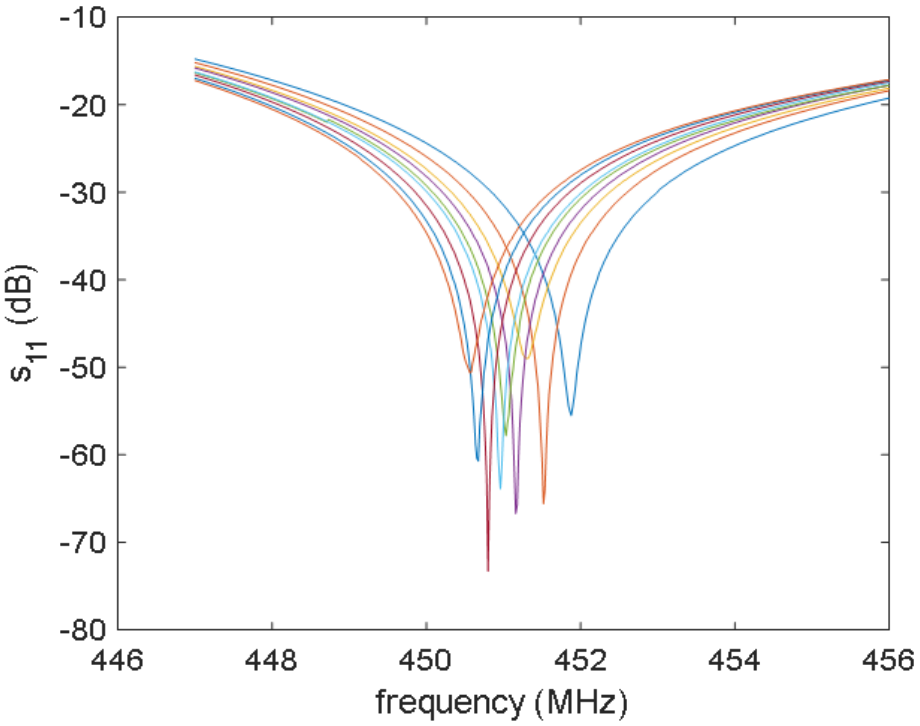

Figure B.15. Measured s_{11} spectra for trial 15 showing the resonant frequencies with respect to varying values of IOP levels.

Table B.15. Tabulated data obtained from trial 15.

	IOP (mmHg)	**Q**	f_0 (MHz)
1	9.58	4477	451.878
2	15.08	9983	451.518
3	20.34	2532	451.32
4	25.42	12098	451.158
5	29.72	6424	451.032
6	35.20	11119	450.96
7	40.12	14031	450.798
8	44.72	10624	450.672
9	50.22	2950	450.564

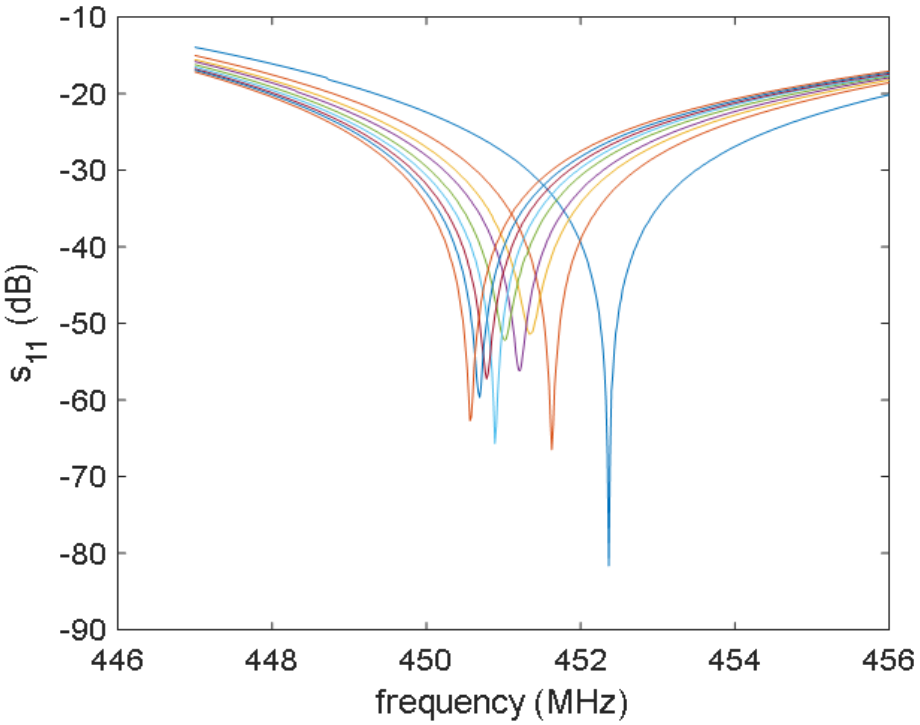

Figure B.16. Measured s_{11} spectra for trial 16 showing the resonant frequencies with respect to varying values of IOP levels.

Table B.16. Tabulated data obtained from trial 16.

	IOP (mmHg)	**Q**	f_0 (MHz)
1	10.14	16170	452.364
2	15.24	13008	451.626
3	19.78	3241	451.338
4	24.80	5697	451.212
5	29.68	3925	451.014
6	34.76	11017	450.888
7	40.24	6199	450.780
8	44.86	6556	450.690
9	50.18	10409	450.564

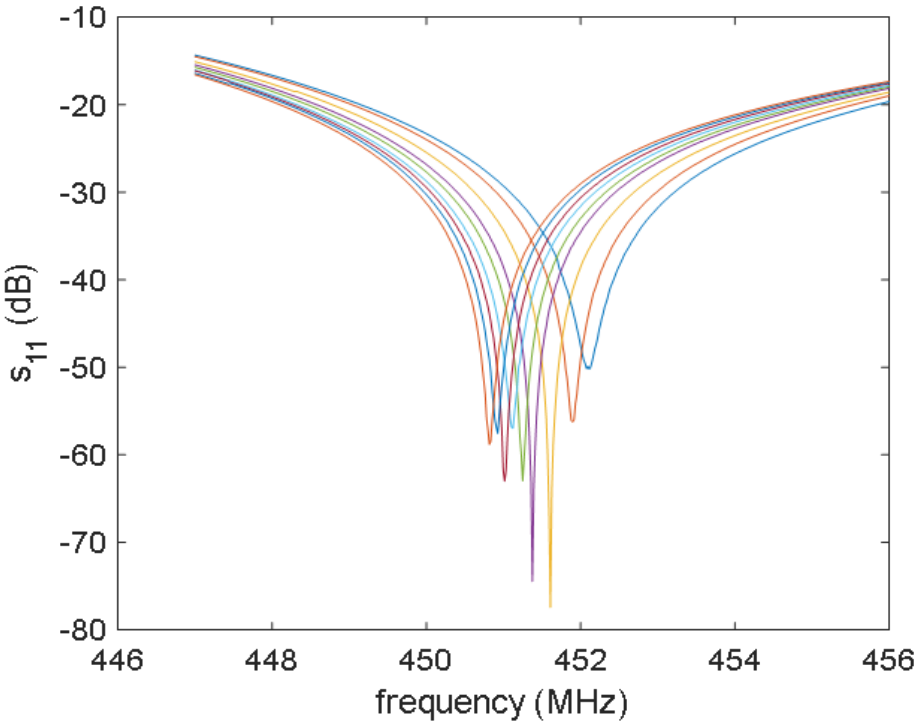

Figure B.17. Measured s_{11} spectra for trial 17 showing the resonant frequencies with respect to varying values of IOP levels.

Table B.17. Tabulated data obtained from trial 17.

	IOP (mmHg)	**Q**	f_0 (MHz)
1	10.68	2443	452.112
2	15.68	4362	451.896
3	19.66	14925	451.608
4	24.84	14627	451.374
5	29.10	11215	451.248
6	34.82	5169	451.122
7	40.34	7562	451.014
8	45.30	5029	450.924
9	49.88	7284	450.816

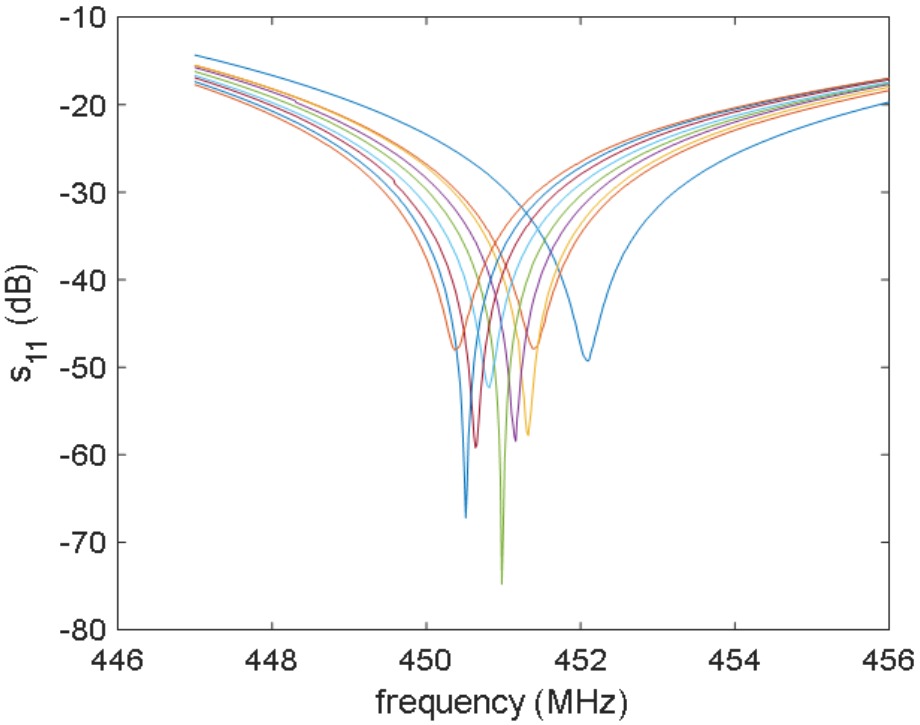

Figure B.18. Measured s_{11} spectra for trial 18 showing the resonant frequencies with respect to varying values of IOP levels.

Table B.18. Tabulated data obtained from trial 18.

	IOP (mmHg)	**Q**	f_0 (MHz)
1	9.74	1748	452.094
2	14.82	1789	451.392
3	19.86	6701	451.320
4	24.82	6960	451.158
5	30.40	13400	450.978
6	34.66	3297	450.816
7	39.74	6499	450.636
8	45.08	11607	450.510
9	49.60	1533	450.366

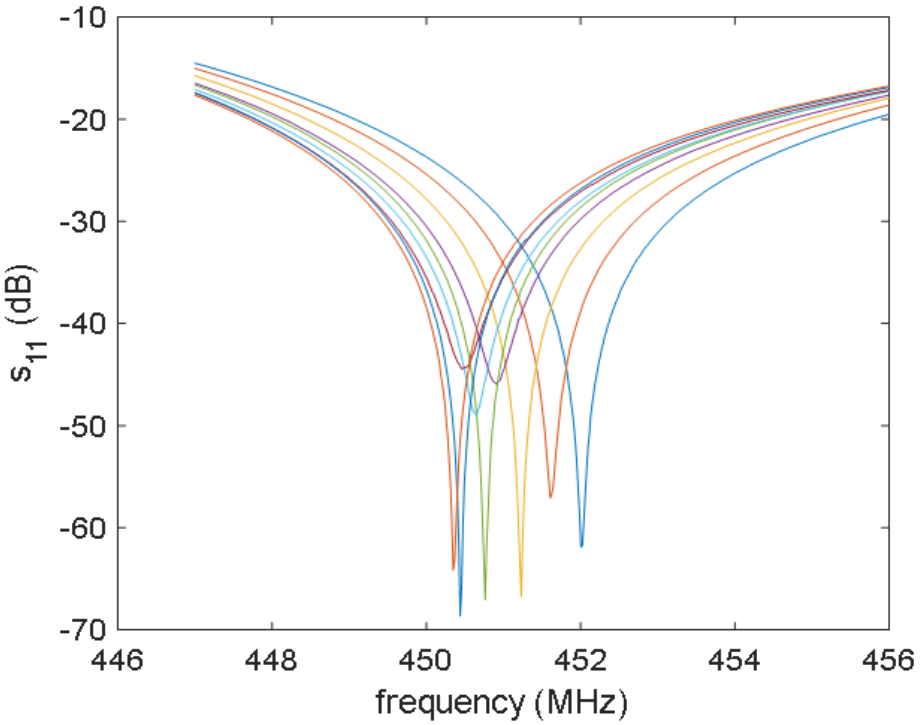

Figure B.19. Measured s_{11} spectra for trial 19 showing the resonant frequencies with respect to varying values of IOP levels.

Table B.19. Tabulated data obtained from trial 19.

	IOP (mmHg)	**Q**	f_0 (MHz)
1	9.68	9154	452.004
2	14.58	6161	451.608
3	20.34	1164	451.230
4	24.48	1390	450.906
5	30.16	10824	450.762
6	35.24	1766	450.654
7	39.76	1037	450.456
8	45.62	11764	450.438
9	50.24	10454	450.348